UTPP-51

A Measurement of Top Quark Mass and Kinematic Properties in Fermilab 1.8-TeV Proton-Antiproton Collisions

Shin AOTA

A dissertation submitted to the Doctoral Program
in Physics, the University of Tsukuba
in partial fulfillment of the requirements for the
degree of Doctor of Philosophy (Science)

January 1997

A Measurement of Top Quark Mass and Kinematic Properties in Fermilab 1.8-TeV Proton-Antiproton Collisions

Shin AOTA

A dissertation submitted to the Doctoral Program
in Physics, the University of Tsukuba
in partial fulfillment of the requirements for the
degree of Doctor of Philosophy (Science)

January 1997

Abstract

We present a measurement of the top quark mass using $W+ \geq$4jet events in $p\bar{p}$ collisions at $\sqrt{s}$=1.8 TeV with the CDF detector at the Fermilab Tevatron Collider using 110 pb^{-1} data collected from 1992 to 1995.

The hadronic W decay is observed in top events. The dijet invariant mass distribution in $W+\geq$4jet events shows an excess of (29$\pm$13) events around a W mass. The dijet mass peak has a mean of $77.1\pm3.8(\text{stat})^{+3.0}_{-2.9}(\text{syst})$ GeV/c^2, which is consistent with the W mass.

Identifying two out of four jets as b-quarks with b-tagging algorithms, we found 11 $t\bar{t}$ candidates events. Furthermore requiring the invariant mass of two leading untagged jets to be within a W mass window, we found 9 events. Using these 9 $t\bar{t}$ candidates events, we extracted a top quark mass of $174.8\pm7.6(\text{stat})\pm5.6(\text{syst})$ GeV/$c^2$with a likelihood method.

Kinematical quantities which describe $t\bar{t}$ production and decay were measured. Various kinematic distributions were compared between CDF data and Monte Carlo calculations. All distributions agree with the Monte Carlo predictions for $t\bar{t}$ production and background.

Acknowledgements

I would like to thank Prof. K. Kondo, Prof. K. Takikawa and Prof. S. Kim for their many ideas, educational advices, helpful discussions and suggestions. I wish to thank Drs. K. Hara and Y. Seiya for their useful discussions and advices.

I thank all members in CDF top mass and kinematics working group. Luc Demortier, Steve Vejcik, Soo-Bong Kim, Jeremy Lys, Richard Hughes, Paul Tipton and Mark Timko provided guidances at critical points in the analysis. Especially Luc Demotier encouraged me through the analysis. Lina Galtieri gave me the opportunity to contribute to the top quark mass measurement. Discussions and conversations with Rick Wilkinson, Nathan Eddy, George Velev, Kirsten Tollefson proved beneficial.

I also wish to thank CDF members of the High Energy Physics group of the University of Tsukuba, Kiyoshi Yasuoka, Takashi Asakawa, Eiichiro Hayashi, Hiroyuki Sato, Tsuyoshi Takada, Toshiharu Uchida, Jun-ichi Suzuki, Tomoko Kuwabara, Takeshi Takano, Housai Nakada, Hirofumi Ikeda and Hiroyuki Minato for their kindness.

I also wish to express appreciation to Carol Picciolo, Kyoko Kunori, Kazuko Kumashiro, Mutumi Uenishi for their constant support with their secretarial works.

Finally, I wish to thank my parents for their assistance and kindness.

The CDF Collaboration

F. Abe,[14] H. Akimoto,[32] A. Akopian,[27] M. G. Albrow,[7] S. R. Amendolia,[23] D. Amidei,[17] J. Antos,[29] C. Anway-Wiese,[4] S. Aota,[32] G. Apollinari,[27] T. Asakawa,[32] W. Ashmanskas,[15] M. Atac,[7] P. Auchincloss,[26] F. Azfar,[22] P. Azzi-Bacchetta,[21] N. Bacchetta,[21] W. Badgett,[17] S. Bagdasarov,[27] M. W. Bailey,[19] J. Bao,[35] P. de Barbaro,[26] A. Barbaro-Galtieri,[15] V. E. Barnes,[25] B. A. Barnett,[13] E. Barzi,[8] G. Bauer,[16] T. Baumann,[9] F. Bedeschi,[23] S. Behrends,[3] S. Belforte,[23] G. Bellettini,[23] J. Bellinger,[34] D. Benjamin,[31] J. Benlloch,[16] J. Bensinger,[3] D. Benton,[22] A. Beretvas,[7] J. P. Berge,[7] J. Berryhill,[5] S. Bertolucci,[8] A. Bhatti,[27] K. Biery,[12] M. Binkley,[7] D. Bisello,[21] R. E. Blair,[1] C. Blocker,[3] A. Bodek,[26] W. Bokhari,[16] V. Bolognesi,[7] D. Bortoletto,[25] J. Boudreau,[24] L. Breccia,[2] C. Bromberg,[18] N. Bruner,[19] E. Buckley-Geer,[7] H. S. Budd,[26] K. Burkett,[17] G. Busetto,[21] A. Byon-Wagner,[7] K. L. Byrum,[1] J. Cammerata,[13] C. Campagnari,[7] M. Campbell,[17] A. Caner,[7] W. Carithers,[15] D. Carlsmith,[34] A. Castro,[21] D. Cauz,[23] Y. Cen,[26] F. Cervelli,[23] H. Y. Chao,[29] J. Chapman,[17] M.-T. Cheng,[29] G. Chiarelli,[23] T. Chikamatsu,[32] C. N. Chiou,[29] L. Christofek,[11] S. Cihangir,[7] A. G. Clark,[23] M. Cobal,[23] M. Contreras,[5] J. Conway,[28] J. Cooper,[7] M. Cordelli,[8] C. Couyoumtzelis,[23] D. Crane,[1] D. Cronin-Hennessy,[6] R. Culbertson,[5] J. D. Cunningham,[3] T. Daniels,[16] F. DeJongh,[7] S. Delchamps,[7] S. Dell'Agnello,[23] M. Dell'Orso,[23] L. Demortier,[27] B. Denby,[23] M. Deninno,[2] P. F. Derwent,[17] T. Devlin,[28] M. Dickson,[26] J. R. Dittmann,[6] S. Donati,[23] J. Done,[30] T. Dorigo,[21] A. Dunn,[17] N. Eddy,[17] K. Einsweiler,[15] J. E. Elias,[7] R. Ely,[15] E. Engels, Jr.,[24] D. Errede,[11] S. Errede,[11] Q. Fan,[26] I. Fiori,[2] B. Flaugher,[7] G. W. Foster,[7] M. Franklin,[9] M. Frautschi,[31] J. Freeman,[7] J. Friedman,[16] H. Frisch,[5] T. A. Fuess,[1] Y. Fukui,[14] S. Funaki,[32] G. Gagliardi,[23] S. Galeotti,[23] M. Gallinaro,[21] M. Garcia-Sciveres,[15] A. F. Garfinkel,[25] C. Gay,[9] S. Geer,[7] D. W. Gerdes,[17] P. Giannetti,[23] N. Giokaris,[27] P. Giromini,[8] L. Gladney,[22] D. Glenzinski,[13] M. Gold,[19] J. Gonzalez,[22] A. Gordon,[9] A. T. Goshaw,[6] K. Goulianos,[27]

H. Grassmann,[23] L. Groer,[28] C. Grosso-Pilcher,[5] G. Guillian,[17] R. S. Guo,[29]
C. Haber,[15] E. Hafen,[16] S. R. Hahn,[7] R. Hamilton,[9] R. Handler,[34]
R. M. Hans,[35] K. Hara,[32] A. D. Hardman,[25] B. Harral,[22] R. M. Harris,[7]
S. A. Hauger,[6] J. Hauser,[4] C. Hawk,[28] E. Hayashi,[32] J. Heinrich,[22]
K. D. Hoffman,[25] M. Hohlmann,[1,5] C. Holck,[22] R. Hollebeek,[22]
L. Holloway,[11] A. Hölscher,[12] S. Hong,[17] G. Houk,[22] P. Hu,[24]
B. T. Huffman,[24] R. Hughes,[26] J. Huston,[18] J. Huth,[9] J. Hylen,[7] H. Ikeda,[32]
M. Incagli,[23] J. Incandela,[7] G. Introzzi,[23] J. Iwai,[32] Y. Iwata,[10] H. Jensen,[7]
U. Joshi,[7] R. W. Kadel,[15] E. Kajfasz,[7a] T. Kamon,[30] T. Kaneko,[32]
K. Karr,[33] H. Kasha,[35] Y. Kato,[20] T. A. Keaffaber,[25] L. Keeble,[8]
K. Kelley,[16] R. D. Kennedy,[28] R. Kephart,[7] P. Kesten,[15] D. Kestenbaum,[9]
R. M. Keup,[11] H. Keutelian,[7] F. Keyvan,[4] B. Kharadia,[11] B. J. Kim,[26]
D. H. Kim,[7a] H. S. Kim,[12] S. B. Kim,[17] S. H. Kim,[32] Y. K. Kim,[15]
L. Kirsch,[3] P. Koehn,[26] K. Kondo,[32] J. Konigsberg,[9] S. Kopp,[5] K. Kordas,[12]
W. Koska,[7] E. Kovacs,[7a] W. Kowald,[6] M. Krasberg,[17] J. Kroll,[7] M. Kruse,[25]
T. Kuwabara,[32] S. E. Kuhlmann,[1] E. Kuns,[28] A. T. Laasanen,[25]
N. Labanca,[23] S. Lammel,[7] J. I. Lamoureux,[3] T. LeCompte,[11] S. Leone,[23]
J. D. Lewis,[7] P. Limon,[7] M. Lindgren,[4] T. M. Liss,[11] N. Lockyer,[22]
O. Long,[22] C. Loomis,[28] M. Loreti,[21] J. Lu,[30] D. Lucchesi,[23] P. Lukens,[7]
S. Lusin,[34] J. Lys,[15] K. Maeshima,[7] A. Maghakian,[27] P. Maksimovic,[16]
M. Mangano,[23] J. Mansour,[18] M. Mariotti,[21] J. P. Marriner,[7] A. Martin,[11]
J. A. J. Matthews,[19] R. Mattingly,[16] P. McIntyre,[30] P. Melese,[27]
A. Menzione,[23] E. Meschi,[23] S. Metzler,[22] C. Miao,[17] G. Michail,[9]
R. Miller,[18] H. Minato,[32] S. Miscetti,[8] M. Mishina,[14] H. Mitsushio,[32]
T. Miyamoto,[32] S. Miyashita,[32] Y. Morita,[14] J. Mueller,[24] A. Mukherjee,[7]
T. Muller,[4] P. Murat,[23] H. Nakada,[32] I. Nakano,[32] C. Nelson,[7]
D. Neuberger,[4] C. Newman-Holmes,[7] M. Ninomiya,[32] L. Nodulman,[1]
S. H. Oh,[6] K. E. Ohl,[35] T. Ohmoto,[10] T. Ohsugi,[10] R. Oishi,[32] M. Okabe,[32]
T. Okusawa,[20] R. Oliver,[22] J. Olsen,[34] C. Pagliarone,[2] R. Paoletti,[23]
V. Papadimitriou,[31] S. P. Pappas,[35] S. Park,[7] A. Parri,[8] J. Patrick,[7]
G. Pauletta,[23] M. Paulini,[15] A. Perazzo,[23] L. Pescara,[21] M. D. Peters,[15]
T. J. Phillips,[6] G. Piacentino,[2] M. Pillai,[26] K. T. Pitts,[7] R. Plunkett,[7]
L. Pondrom,[34] J. Proudfoot,[1] F. Ptohos,[9] G. Punzi,[23] K. Ragan,[12]
A. Ribon,[21] F. Rimondi,[2] L. Ristori,[23] W. J. Robertson,[6] T. Rodrigo,[7a] S.
Rolli,[23] J. Romano,[5] L. Rosenson,[16] R. Roser,[11] W. K. Sakumoto,[26]
D. Saltzberg,[5] A. Sansoni,[8] L. Santi,[23] H. Sato,[32] V. Scarpine,[30]
P. Schlabach,[9] E. E. Schmidt,[7] M. P. Schmidt,[35] A. Scribano,[23] S. Segler,[7]

S. Seidel,[19] Y. Seiya,[32] G. Sganos,[12] A. Sgolacchia,[2] M. D. Shapiro,[15] N. M. Shaw,[25] Q. Shen,[25] P. F. Shepard,[24] M. Shimojima,[32] M. Shochet,[5] J. Siegrist,[15] A. Sill,[31] P. Sinervo,[12] P. Singh,[24] J. Skarha,[13] K. Sliwa,[33] F. D. Snider,[13] T. Song,[17] J. Spalding,[7] P. Sphicas,[16] F. Spinella,[23] M. Spiropulu,[9] L. Spiegel,[7] L. Stanco,[21] J. Steele,[34] A. Stefanini,[23] K. Strahl,[12] J. Strait,[7] R. Ströhmer,[9] D. Stuart,[7] G. Sullivan,[5] A. Soumarokov,[29] K. Sumorok,[16] J. Suzuki,[32] T. Takada,[32] T. Takahashi,[20] T. Takano,[32] K. Takikawa,[32] N. Tamura,[10] F. Tartarelli,[23] W. Taylor,[12] P. K. Teng,[29] Y. Teramoto,[20] S. Tether,[16] D. Theriot,[7] T. L. Thomas,[19] R. Thun,[17] M. Timko,[33] P. Tipton,[26] A. Titov,[27] S. Tkaczyk,[7] D. Toback,[5] K. Tollefson,[26] A. Tollestrup,[7] J. Tonnison,[25] J. F. de Troconiz,[9] S. Truitt,[17] J. Tseng,[13] N. Turini,[23] T. Uchida,[32] N. Uemura,[32] F. Ukegawa,[22] G. Unal,[22] S. C. van den Brink,[24] S. Vejcik, III,[17] G. Velev,[23] R. Vidal,[7] M. Vondracek,[11] D. Vucinic,[16] R. G. Wagner,[1] R. L. Wagner,[7] J. Wahl,[5] C. Wang,[6] C. H. Wang,[29] G. Wang,[23] J. Wang,[5] M. J. Wang,[29] Q. F. Wang,[27] A. Warburton,[12] G. Watts,[26] T. Watts,[28] R. Webb,[30] C. Wei,[6] C. Wendt,[34] H. Wenzel,[15] W. C. Wester, III,[7] A. B. Wicklund,[1] E. Wicklund,[7] R. Wilkinson,[22] H. H. Williams,[22] P. Wilson,[5] B. L. Winer,[26] D. Wolinski,[17] J. Wolinski,[18] X. Wu,[23] J. Wyss,[21] A. Yagil,[7] W. Yao,[15] K. Yasuoka,[32] Y. Ye,[12] G. P. Yeh,[7] P. Yeh,[29] M. Yin,[6] J. Yoh,[7] C. Yosef,[18] T. Yoshida,[20] D. Yovanovitch,[7] I. Yu,[35] L. Yu,[19] J. C. Yun,[7] A. Zanetti,[23] F. Zetti,[23] L. Zhang,[34] W. Zhang,[22] and S. Zucchelli[2]

(CDF Collaboration)

[1] *Argonne National Laboratory, Argonne, Illinois 60439*

[2] *Istituto Nazionale di Fisica Nucleare, University of Bologna, I-40126 Bologna, Italy*

[3] *Brandeis University, Waltham, Massachusetts 02254*

[4] *University of California at Los Angeles, Los Angeles, California 90024*

[5] *University of Chicago, Chicago, Illinois 60637*

[6] *Duke University, Durham, North Carolina 27708*

[7] *Fermi National Accelerator Laboratory, Batavia, Illinois 60510*

[8] *Laboratori Nazionali di Frascati, Istituto Nazionale di Fisica Nucleare, I-00044 Frascati, Italy*

[9] *Harvard University, Cambridge, Massachusetts 02138*

[10] *Hiroshima University, Higashi-Hiroshima 724, Japan*

[11] *University of Illinois, Urbana, Illinois 61801*

[12] *Institute of Particle Physics, McGill University, Montreal H3A 2T8, and University of Toronto, Toronto M5S 1A7, Canada*

[13] *The Johns Hopkins University, Baltimore, Maryland 21218*

[14] *National Laboratory for High Energy Physics (KEK), Tsukuba, Ibaraki 305, Japan*

[15] *Lawrence Berkeley Laboratory, Berkeley, California 94720*

[16] *Massachusetts Institute of Technology, Cambridge, Massachusetts 02139*

[17] *University of Michigan, Ann Arbor, Michigan 48109*

[18] *Michigan State University, East Lansing, Michigan 48824*

[19] *University of New Mexico, Albuquerque, New Mexico 87131*

[20] *Osaka City University, Osaka 588, Japan*

[21] *Universita di Padova, Istituto Nazionale di Fisica Nucleare, Sezione di Padova, I-35131 Padova, Italy*

[22] *University of Pennsylvania, Philadelphia, Pennsylvania 19104*

[23] *Istituto Nazionale di Fisica Nucleare, University and Scuola Normale Superiore of Pisa, I-56100 Pisa, Italy*

[24] *University of Pittsburgh, Pittsburgh, Pennsylvania 15260*

[25] *Purdue University, West Lafayette, Indiana 47907*

[26] *University of Rochester, Rochester, New York 14627*

[27] *Rockefeller University, New York, New York 10021*

[28] *Rutgers University, Piscataway, New Jersey 08854*

[29] *Academia Sinica, Taipei, Taiwan 11529, Republic of China*

[30] *Texas A&M University, College Station, Texas 77843*

[31] *Texas Tech University, Lubbock, Texas 79409*

[32] *University of Tsukuba, Tsukuba, Ibaraki 305, Japan*

[33] *Tufts University, Medford, Massachusetts 02155*

[34] *University of Wisconsin, Madison, Wisconsin 53706*

[35] *Yale University, New Haven, Connecticut 06511*

Contents

List of Tables

List of Figures

Chapter 1

Introduction

Elementary particle physics describes the nature of interactions between the fundamental constituents of matter. Standard Model $SU(3)_C \otimes SU(2)_L \otimes U(1)_Y$ has been successful over all energy ranges explored so far. According to this model, the ultimate particles are leptons and quarks which have a spin of $1/2$ in units of $\hbar$ and have no structure. Both leptons and quarks have three generations. Each generation consists of a $SU(2)_L$(weak isospin) doublet. The doublet in the first generation is an electron neutrino and an electron for leptons and a u quark and a d quark with charge $2/3$ and $-1/3$ for quarks. The leptons and quarks have a specific helicity properties, so that electrons, for instance, are described in weak isospin space by a left handed doublet and a right-handed singlet which must be suitably normalized to give unity for the unpolarised electron state. Gauge bosons mediate the interactions between particles.

In constructing the unified electroweak theory, Weinberg and Salam in-

troduced a pair of "Higgs fields" which transform as a doublet under SU(2). The fields are such that the lowest energy state is no longer empty space but a space permeated by the neutral Higgs field. The W and Z bosons couple to this field generating terms in the Lagrangian corresponding to massive particles. The zero mass of the photon is preserved in the Standard Model because it does not couple to the Higgs field. The quanta of the Higgs field should be manifest as "Higgs bosons" which supposed to be a scalar particle and electrically neutral.

$$\begin{array}{cccccccccc} \begin{pmatrix}\nu_e\\ e^-\end{pmatrix}_L & \begin{pmatrix}\nu_\mu\\ \mu^-\end{pmatrix}_L & \begin{pmatrix}\nu_\tau\\ \tau^-\end{pmatrix}_L & & e_R & & \mu_R & & \tau_R & \\ \begin{pmatrix}u\\ d'\end{pmatrix}_L & \begin{pmatrix}c\\ s'\end{pmatrix}_L & \begin{pmatrix}t\\ b'\end{pmatrix}_L & u_R & c_R & t_R & d'_R & s'_R & b'_R & \\ \gamma & & & W^- & & Z & & g & & \end{array}$$

This thesis describe a measurement of the top quark mass in pure top candidate events which were collected at Fermilab $\sqrt{s}$=1.8 TeV $p\bar{p}$ collider from August 1992 to November 1995. Total integrated luminosity is 110pb^{-1}.

1.1 The top quark mass

The Standard Model does not predict the top quark mass. The mass of top quark was expected to be very heavy because many experiments had failed to obtain an evidence for top quark production. Within the Standard Model, this large mass is linked to the Higgs mechanism used to model the

role of mass and its connection to gauge bosons. The measurement of the properties of the top quark -particularly its mass- and gauge bosons thus provide a link to the yet undiscovered Higgs boson through the calculation of radiative corrections. The top quark mass is an independent parameter with no predictions, although constraints on it can be given by the measurements of other Standard Model quantities.

1.1.1 Previous indirect measurement

So far many collider experiments had failed to establish the existence of the top quark. In the previous studies, upper and lower limits on the top quark mass were provided. Indirect lower limits were obtained by the measurements of $B^0\bar{B}^0$ mixing with the ARGUS and the CLEO detector and the CP violation parameter ϵ/ϵ' at FNAL and CERN. These results were

$m_{top} \geq 45.0 GeV/c^2$ (90 % C.L.) $B^0\bar{B}^0$ mixing [1][2][3](1988)

$m_{top} \geq 50.0 GeV/c^2$ ϵ/ϵ'[4](1988)

By the direct measurements performed at $p\bar{p}$ and e^+e^- colliders, several lower limit were provided.

$m_{top} \geq 44.5 GeV/c^2$ e^+e^- collider at LEP[5](1989)

$m_{top} \geq 40.7 GeV/c^2$ e^+e^- collider at SLC[6](1989)

$m_{top} \geq 118 GeV/c^2$ $p\bar{p}$ collider at CDF[7](1994)

$m_{top} \geq 131 GeV/c^2$ $p\bar{p}$ collider at D0[8](1994)

The results from a global analysis of all electroweak data, including precise measurements of the Z^0 mass and decay widths from LEP and the W mass measured at CDF and UA2, gave a bound of $M_{top} = 177^{+11+18}_{-11-19}$ GeV/c^2 [9].

1.1.2 Direct measurement at Fermilab

The first evidence for top quark production was reported by the CDF collaboration in April 1994. CDF found 9 top candidate events in 19pb^{-1} data sample of $\sqrt{s}$=1.8 TeV proton-antiproton collisions at the Fermilab Tevatron particle accelerator[10]. The top quark mass and production cross section were measured to be 174$\pm$10(stat)$^{+13}_{-12}$(syst) GeV/c^2 and 13.9$^{+6.1}_{-4.8}$pb, respectively. In February 1995, CDF and D0 collaboration reported the observation of top quark production in 67pb^{-1} data. CDF measured the top quark mass to be 176$\pm$8(stat)$\pm$10(syst) GeV/c^2, and the $t\bar{t}$ production cross section to be 6.8$^{+3.6}_{-3.4}$pb[11][12].

The CDF carried out the RUN1 collider run from 1992 to 1995 and collected 110pb^{-1} data in total. The analysis in this thesis was carried out with the full data sample of 110pb^{-1}.

1.2 Heavy quark production and decay

1.2.1 Production process

The production processes of heavy flavor in the lowest order parton subprocesses are quark-antiquark annihilation and gluon-gluon fusion,

$$q\bar{q} \rightarrow Q\bar{Q}, \qquad gg \rightarrow Q\bar{Q}$$

where q, g, and Q are light quark, gluon and heavy quark, respectively.

The differential cross sections are given by

$$\frac{d\hat{\sigma}}{d\hat{t}}(q\bar{q} \rightarrow Q\bar{Q}) = \frac{4\pi\alpha_s}{9\hat{s}^4}\left[(m^2-\hat{t})^2+(m^2-\hat{u})^2+2m^2\hat{s}\right]$$

where $\hat{s} = (q+\bar{q})^2, \hat{t} = (q-Q)^2, \hat{u} = (q-\bar{Q})^2$, α_s is the strong coupling constant and m is the heavy quark mass and,

$$\begin{aligned}\frac{d\hat{\sigma}}{d\hat{t}}(gg \rightarrow Q\bar{Q}) = \frac{\pi\alpha_s}{8\hat{s}^2}\Bigg[&\frac{6(m^2-\hat{t})(m^2-\hat{u})}{\hat{s}^2} - \frac{m^2(s-4m^2)}{3(m^2-\hat{t})(m^2-\hat{u})} \\ &+ \frac{4}{3}\frac{(m^2-\hat{t})(m^2-\hat{u})-2m^2(m^2+\hat{t})}{(m^2-\hat{t})^2} + \frac{4}{3}\frac{(m^2-\hat{t})(m^2-\hat{u})-2m^2(m^2+\hat{u})}{(m^2-\hat{u})^2} \\ &- 3\frac{(m^2-\hat{t})(m^2-\hat{u})+m^2(\hat{u}-\hat{t})}{\hat{s}(m^2-\hat{t})} - 3\frac{(m^2-\hat{t})(m^2-\hat{u})+m^2(\hat{t}-\hat{u})}{\hat{s}(m^2-\hat{u})}\Bigg]\end{aligned}$$

where $\hat{s} = (g_1+g_2)^2, \hat{t} = (g_1-Q)^2, \hat{u} = (g_1-\bar{Q})^2$.

The $2 \rightarrow 3$ parton subprocesses that produce $Q\bar{Q}$ pairs are

$$\begin{aligned} q\bar{q} &\rightarrow Q\bar{Q}g \\ gg &\rightarrow Q\bar{Q}g \\ qg &\rightarrow Q\bar{Q}q \end{aligned}$$

The total cross section for heavy flavor production has been completely calculated by E. Laenen *et al* [13] with the exact order α_s^3 corrected cross section and the resummation of the leading soft gluon corrections in all orders of perturbation theory. The theoretical cross section for $t\bar{t}$ production as a function of M_{top} is shown in Fig. 1.1.

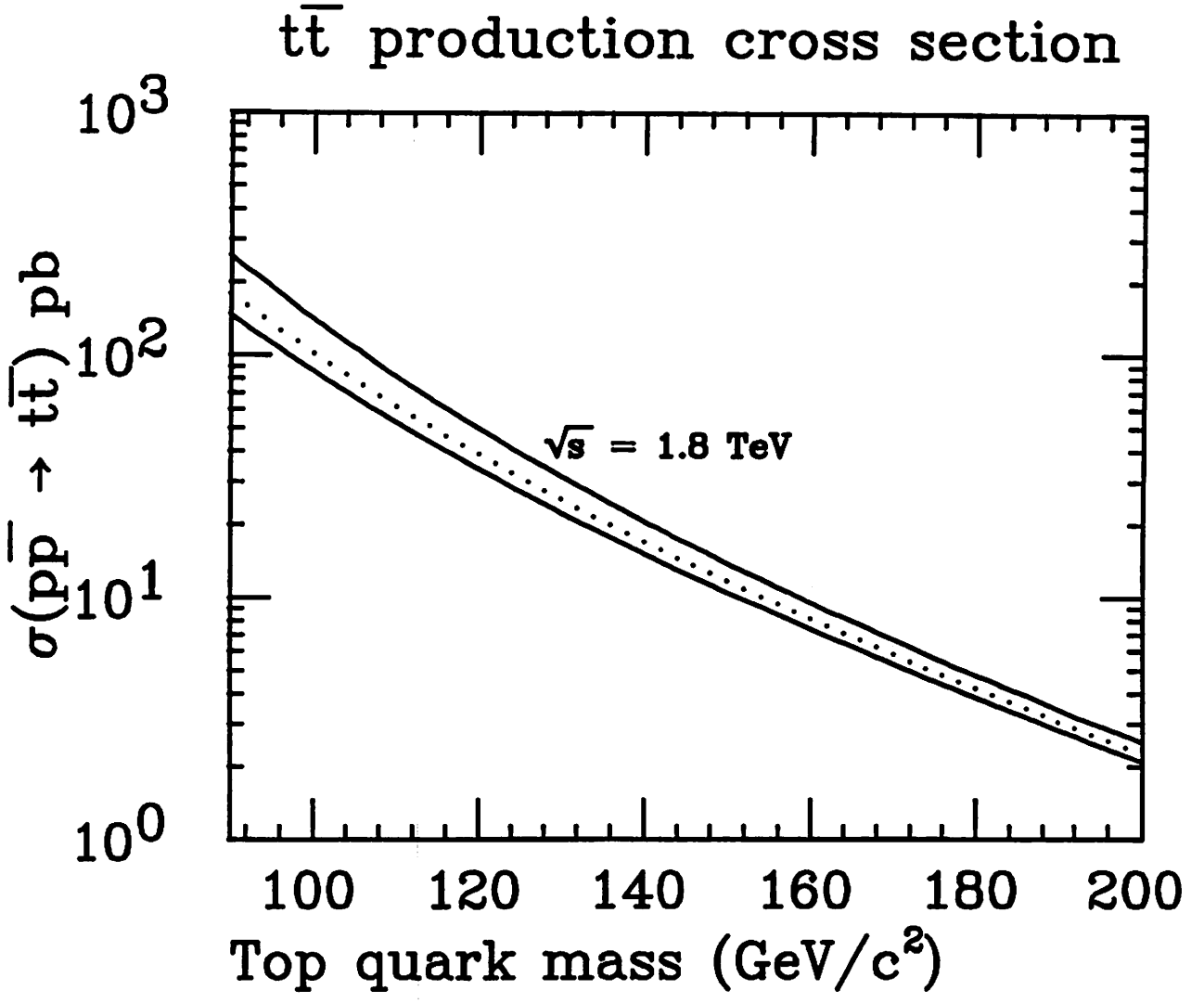

Figure 1.1: Theoretical cross section of $t\bar{t}$ pair production in $p\bar{p}$ collisions at $\sqrt{s} = 1.8$ TeV. Solid lines show upper and lower limits of the top quark cross section. Dashed line shows the central value.

1.2.2 Decay process

In the Standard Model, top quark decays almost exclusively into a W boson and a b quark. If the mass of the top quark is larger than the sum of the masses of the W boson and the b quark(about 85 GeV), the W boson is a real particle. The W boson subsequently decays either to a charged lepton and a neutrino, or a quark and antiquark. In a $t\bar{t}$ event, two top quarks decay into two W bosons and two b quarks. If both W bosons decay into two quarks, we have 6 quarks in the final state of $t\bar{t}$ event. Each quark hadronizes to a jet. We call such events "Multijet events". If one W boson decays into a charged lepton and a neutrino and the other decays into two quarks, we have 2 leptons and 4 jets. We call such events "Lepton + jets events". If both W bosons decay into two leptons, we will get 4 leptons and 2 jets. We call such events "Dilepton events". A diagram of $t\bar{t}$ production and decay is shown in Fig. 1.2. The branching ratios for the different decay modes are listed in Table 1.1

Most often both W bosons decay to a quark-antiquark pair, leading to a fully hadronic final state. This happens at a rate of about 44% of $t\bar{t}$ decays, but a huge background from all other QCD multijet production processes makes an extraction of the $t\bar{t}$ signal extremely difficult. If one of the W bosons decays leptonically to $e\nu$ or $\mu\nu$, the background is substantially reduced. Because it is difficult to identify hadronic decays of τ leptons, the backgrounds to $\tau\nu$ decays cannot be substantially reduced. This "lepton + jets" mode occurs at a rate of about 30% and the background comes predominantly from higher-order production of W bosons, where the W recoils

Decay mode	Branting ratio
$t\bar{t} \to (q\bar{q}b)(q\bar{q}\bar{b})$	36/81
$t\bar{t} \to (q\bar{q}b)(e\nu\bar{b})$	12/81
$t\bar{t} \to (q\bar{q}b)(\mu\nu\bar{b})$	12/81
$t\bar{t} \to (q\bar{q}b)(\tau\nu\bar{b})$	12/81
$t\bar{t} \to (e\nu b)(\mu\nu\bar{b})$	2/81
$t\bar{t} \to (e\nu b)(\tau\nu\bar{b})$	2/81
$t\bar{t} \to (\mu\nu b)(\tau\nu\bar{b})$	2/81
$t\bar{t} \to (e\nu b)(e\nu\bar{b})$	1/81
$t\bar{t} \to (\mu\nu b)(\mu\nu\bar{b})$	1/81
$t\bar{t} \to (\tau\nu b)(\tau\nu\bar{b})$	1/81

Table 1.1: The decay mode of $t\bar{t}$ production and branting ratio.

against significant jet activity. This is referred to as "W + multijet" background.

1.3 Background process against the top quark signature

As stated in the previous section, "W + multijet" production is a dominant background process in the "lepton + jets" mode. A diagram of W + multijet producion is shown in Fig. 1.3. Standard model top decays always contain a b quark in the final state. Suppression of the W + mutijet background in this search relies on the identification of at least one b or $\bar{b}$ quark among the decay products.

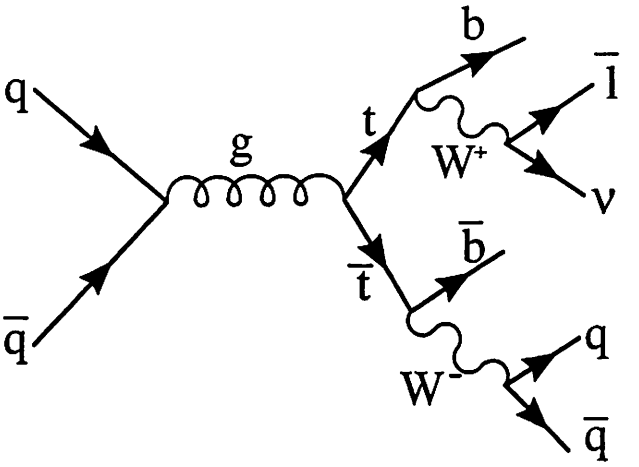

Figure 1.2: A diagram of $t\bar{t}$ production and decay process.

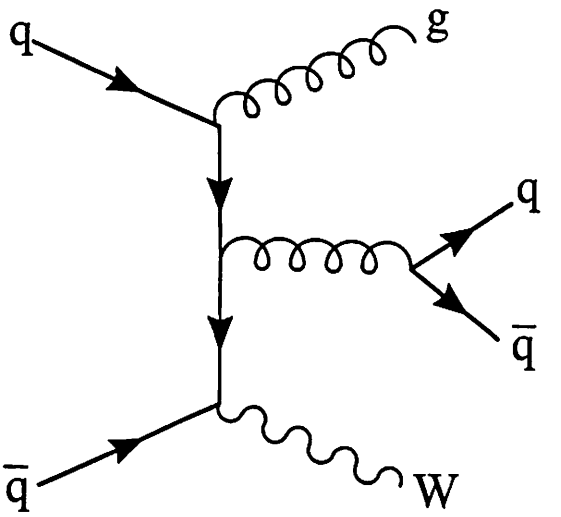

Figure 1.3: A diagram of W + multijet production.

Chapter 2

The CDF Detector

The Fermi National Accelerator Laboratory (FNAL) has the world highest energy accelerator called the Tevatron. Collider Detector at Fermilab (CDF) is the first general-purpose detector built to exploit physics in $p\bar{p}$ collision with this machine and currently one of two detectors which can prove the existence of top quark in the world. The design purpose of the Collider Detector at Fermilab (CDF) is to measure the energy and momentum of particles and identify them produced at the Tevatron collider. It was first commissioned in 1987 and took 4.3 pb^{-1} data in the 1988-1989 Collider Run. Since then the CDF has undergone several upgrades, some of which are crucial to this analysis. The upgrades include the addition of a Silicon microstrip Vertex detector (SVX), extension of the muon coverage and several enhancements in the Data Acquisition system (DAQ). This chapter briefly describes an overview of the Tevatron collider and the CDF detector.

2.1 The Tevatron collider

The Fermilab Tevatron collider currently produces the highest energy collisions in the world, colliding antiprotons with protons at a center-of-mass energy of 1.8 TeV. The Tevatron collider consists of two rings of radius 1km, proton injector, antiproton injector, accumulator, linear accelerator and booster as shown in Fig. 2.1. The protons used in the collisions originate from Hydrogen gas molecules which are first ionized and the resulting negative ions accelerated to 750 KeV in a Cockroft-Walton electrostatic generator. The Hydrogen ions are then accelerated to 200 MeV in a linear accelerator. The ions emerge from the LINAC through a carbon foil that strips their outer electrons thereby leaving only protons. Protons thus produced are stored in a Booster Ring, a synchrotron accelerator, where they are accelerated to 8 GeV. In the Booster, proton bunches are collected and injected into the Main Ring, also a synchrotron accelerator. The Main Ring consists of 6 km alternating dipole (bending) and quadupole (focusing) magnets. The Main Ring also contains RF cavities that boost the protons to 150 GeV. The Main Ring then injects these protons into the Tevatron or to Fixed Target Experimental Stations. Protons from the Main Ring also act as the source of antiprotons. These protons are removed from the Main Ring and focused on a target which produces, amongst other secondary particles, antiprotons. Antiprotons are stored in the Accumulator Ring. After enough antiprotons have been accumulated, they are reinjected first into the Main Ring and then eventually into the Tevatron. The Tevatron is a ring of superconducting magnets that lies directly beneath the Main Ring. In the Tevatron protons

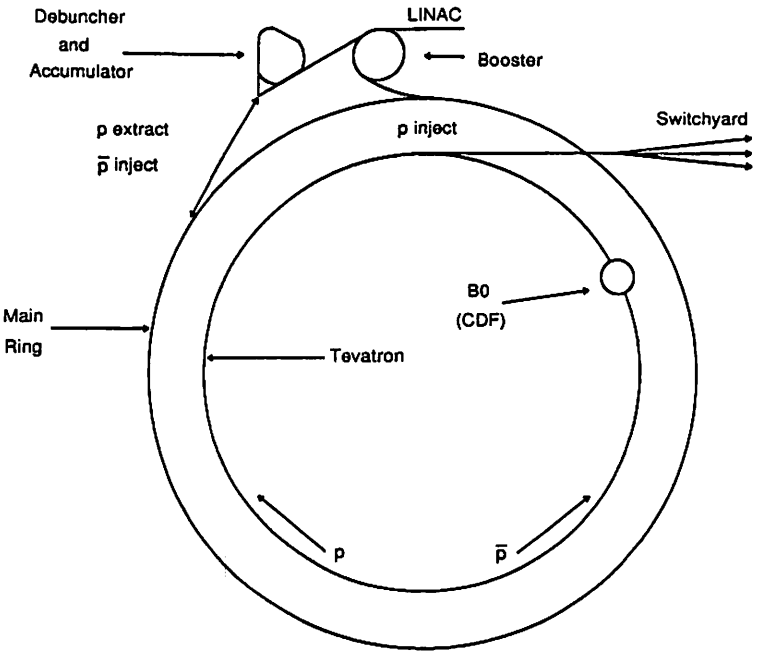

Figure 2.1: The Tevatron collider at Fermilab.

and antiprotons are accelerated to 900 GeV and then made to collide at two interaction regions, B0 and D0, at which are housed Fermilab's two detectors, CDF and D0 respectively.

At the B0 interaction region, the beam is roughly circular in cross-section with a radius defined by one σ of $\sim$ 40 μm. The longitudinal profile of the beam is apporoximately Gaussian with a width of 30$\sim$35 cm.

2.2 Detector overview

The perspective view of CDF detector is shown in Fig. 2.2. The side-view cross section of the CDF detector is shown in Fig. 2.3. The detector is forward-backward symmetric about the interaction point which is at the lower-right edge on the beam line. The detector consists of a central detector which is made up of the solenoidal magnet, steel yoke, tracking chambers, electromagnetic calorimeters, hadron calorimeters and muon chambers. Forward/backward calorimeters and muon toroidal spectrometers are mounted about 6m far from the interaction point.

Surrounding the 1.9 cm radius beryllium beampipe is a 4 layer silicon microstrip vertex detector (SVX) used to measure displaced vertices. Surrounding the SVX are a series of Vertex Time Projection Chambers (VTX) which reconstruct the z coordinates of the vertices of every interaction. A Cylindrical Drift Chamber (CTC) envelops the VTX and provides tracking information. An axial magnetic field of 1.412 Tesla permeates the CTC. Surrounding the CTC are both electromagnetic and hadronic calorimeters used to measure the energy of particles. Behind thick plates of steel and furthest from the beamline lie CDF's muon chambers that detect minimum ionizing particles.

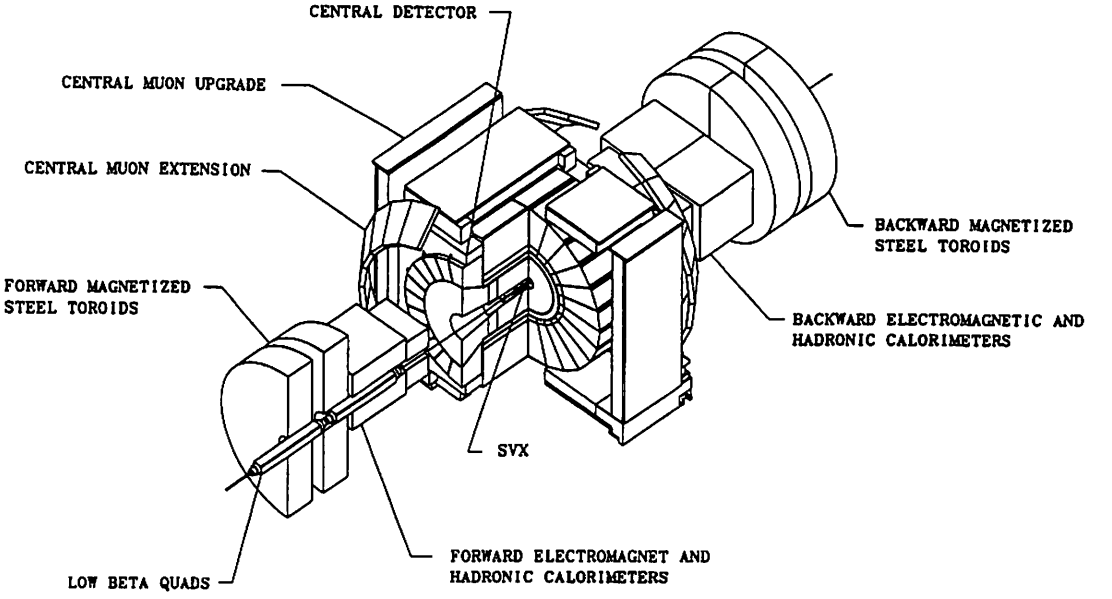

Figure 2.2: Perspective view of the CDF detector, showing the forward, central and backward sections.

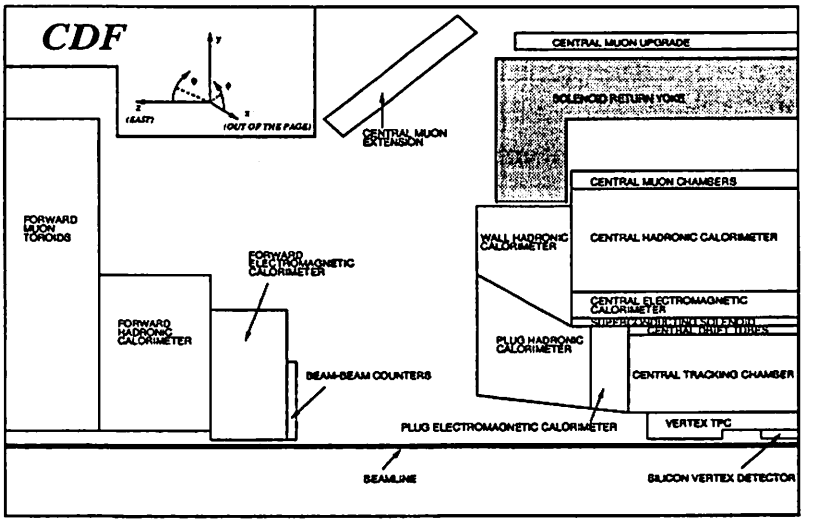

Figure 2.3: Cross section of one quadrant of the CDF detector.

2.3 Coordinate system

CDF employs a right-handed coordinate system in which the z-axis lies in the proton direction, the y-axis points upwards from the plane of the Tevatron and the x-axis points radially outwards as shown in Fig. 2.4. The interaction point, coordinates (0,0,0), is taken to be the geometric center of the detector. The polar angle θ is measured in the r - z plane and goes to zero in the positive z-direction.

It is useful to work in terms of the geometric parameters, rapidity,

$$y = \frac{1}{2} ln(\frac{E + P_Z}{E - P_Z})$$

and the closely related pseudorapidity,

$$\eta = -ln(tan\frac{\theta}{2}) = \frac{1}{2} ln(\frac{P + P_Z}{P - P_Z})$$

The transverse momentum P_T and transverse energy E_T are defined as

$$P_T = \mid \mathbf{P} \mid \times sin\ \theta$$

$$E_T = E \times sin\ \theta$$

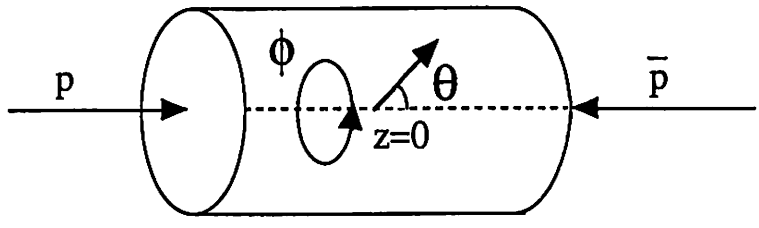

Figure 2.4: The CDF coordinate system.

2.4 Tracking

The CDF tracking system covers the angular range between ~8° and ~172° in polar angle, with three dimensional tracking available from 40° to 140°. The tracking system achieves excellent resolution due to the 1.412 Tesla magnetic field provided by a Superconducting Solenoid. Tracking at CDF is used to provide position information of charged particles along their helical trajectotries in the solenoidal magnetic field. Absence of tracks matched to electromagnetic clusters in the calorimeter is also used to identify photons.

The tracking system consists primarily of the solenoid, a silicon microvertex detector (SVX), a vertex time projection chamber (VTX),and the Central tracking chamber (CTC). These detectors are summarized in Table. 2.1.

Tracking system	Angular coverage	2 track resolution	Momentum resolution
SVX	$\sim 6.3° < \theta < \sim 173.7°$	-	$\Delta P_T/P_T = 0.011 \times P_T$ (GeV/c)
VTX	$\sim 8° < \theta < \sim 172°$	$6mm/\theta$	
		6mm (R)	-
		$3cm(\phi)$	
CTC	$\sim 40° < \theta < \sim 140°$	3.5mm	$\Delta P_T/P_T = 0.001 \times P_T$ (GeV/c)

Table 2.1: Properties of CDF tracking systems.

2.4.1 Solenoid

A 1.412 Tesla magnetic field is produced by a NbTi/Cu superconducting solenoid and permeates a cylindrical volume of 4.8 m in length and 3 m in

diameter. An average current of 4650 Amps produces the magnetic field. The magnetic field flux is returned through a steel yoke which also functions to support the calorimeters. The magnetic field is mapped precisely and offline corrections to tracking are performed using this map. Some non-uniformities in the field are also corrected for using this map.

2.4.2 SVX

One of the major upgrades of CDF for Run1A was the installation of a silicon microstrip vertex detector (SVX), the innermost and closest to the interaction point detector of CDF. The SVX was upgraded for the high luminosity expected in Run1B. The SVX surrounds the 1.9 cm radius beampipe and is itself surrounded by the VTX. It provides precise tracking in the $r-\phi$ plane in order to measure the impact parameter of particles traversing its fiducial volume.

The SVX is segmented into two barrels, one on either side of the nominal interaction point as shown in Fig. 2.5. Each barrel is composed of 12 wedges, each wedge occupying 30° in ϕ. At both ends of each barrel is a beryllium support structure that contains readout electronics modules and chilled water cooling tubes. The SVX is operated at a nominal temperature of 20°C. There are 4 layers in each wedge, numbered 0 to 3. Each layer consists of a ladder which in turn consists of 3 rectangular strip detectors laid end-to-end (3×8.5 cm). The active length of each barrel is 25.5 cm, that is, a total of 51 cm along the beam direction. Each wedge is read out independently, which leads to 46,080 channels for the SVX alone. This is a substantial fraction of all

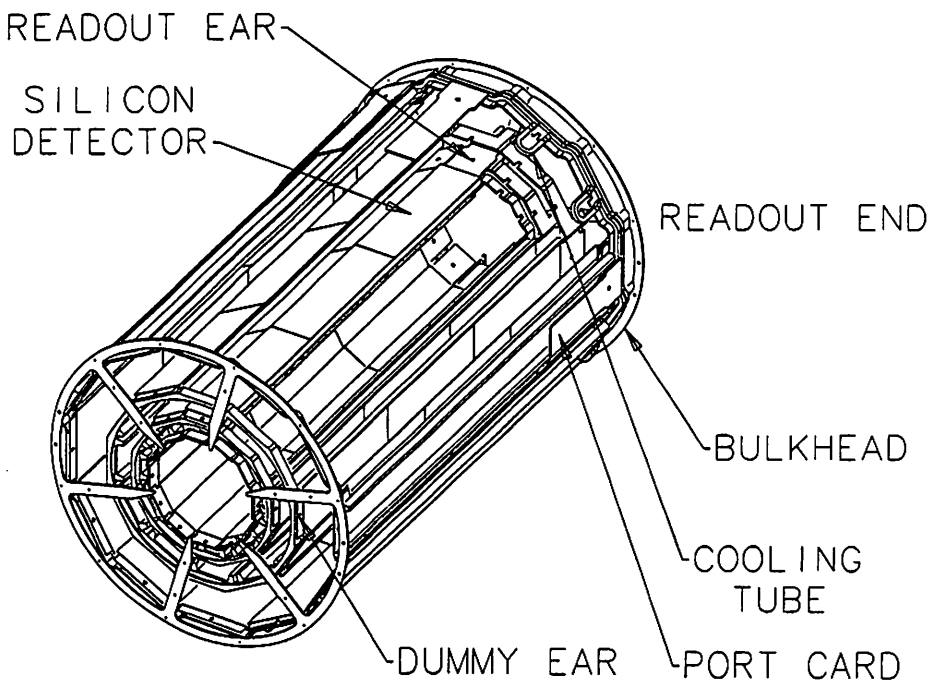

Figure 2.5: An isometric view of the SVX detector.

readout channels for CDF.

Because the longitudinal spread of the beam is ~30 cm, the SVX acceptance is 60% in $p\bar{p}$ interactions. The SVX hit information, when combined with CTC hit information improves track helix measurements. Track reconstruction in the SVX begins with a CTC track that is required to have at least 2 hits in the SVX not associated with any other track. The SVX momentum resolution is $\Delta P_T/P_T = 0.011 \times P_T$ (GeV/c). The individual hit resolution is measured in the data to be $\sim 11\mu$m.

The SVX can be used to study particles with lifetimes on the order of a picosecond. Thus the SVX provides the basis for a top quark search, in which displaced vertices produced by b quarks possibly arising from top quark decay are detected in the SVX.

2.4.3 VTX

The Vertex Time Projection Chamber (VTX) for the Run1A and Run1B is an upgrade of a similar chamber (VTPC) used in Run0. The upgrade was necessary to handle the much higher luminosity expected in Run1A and Run1B and to make space for SVX. It provides tracking information out to a radius of 22cm for $|\eta| < 3.25$ region. The VTX is segmented into 2 barrels, East and West, with the two barrels lying on either side of the nominal interaction position. As mentioned earlier, the VTX completely surrounds the SVX. Each half consists of 28 octagonal modules which extend out to 1.5m on either side of the nominal interaction point. The inner 18 modules that surround the SVX contain 16 sense wires strung in the $r - \phi$ plane perpendicular to a radial line from the origin. Ten additional modules have 24 sense wires. The drift gap in the Argon-Ethane atmosphere between sense wires is 4cm. Adjacent modules are rotated by 11.3° in ϕ to aid better matching of the CTC $r - \phi$ track segments to the VTX segments.

By measuring the drift times of electrons hitting sense wires, a primary particle track can be reconstructed in the $r - z$ plane. The azimuth of the track is obtained from charge induced on the cathode pads. The VTX provides 3-D track reconstruction for $|\eta| < 3.25$ region.

The main function of the VTX is to locate the primary z vertex of an event, that is, the $p\bar{p}$ interaction point. This is achieved by finding the convergence of all reconstructed tracks in the event. The z resolution of primary vertices found by the VTX is 1-2 mm depending on track multiplicity in the event. Since collisions are distributed like a Gaussian with $\sigma \approx 35$ cm,

the VTX provides ample coverage. The event vertex is used to calculate transverse quantities.

2.4.4 CTC

The 3.2m long Central Tracking Chamber (CTC) surrounds the VTX. It fits inside a superconducting solenoid that provides a 1.412 Tesla axial magnetic field. The chamber consists of 84 layers of sense wires grouped into 9 superlayers: 5 axial and 4 stereo. The axial superlayers consist of 12 wires each arranged parallel to the beam direction that enable track reconstruction in the $r - \phi$ plane. The stereo superlayers, interspersed between the axial ones, have 6 wires each, at $\pm 3°$ to the axial direction and enable stereo track reconstruction i.e. in the r-z plane. Figure. 2.6 shows the endplate of CTC showing the wire slots.

The CTC performance is excellent, as is extensively documented elsewhere[14]. The excellent momentum resolution achieved by the CTC is largely due to the large magnetic field strength and the large tracking volume. Beam-constrained fits further improve the momentum resolution.

The excellent position resolution is used to identify electrons by matching tracks to energy deposition in electromagnetic calorimeters and muons by matching tracks to hits in muon chambers. The CTC is also used to identify secondary vertices due to decay of long-lived particles, to study calorimetry response as a function of momentum and position in the calorimeter, and also to identify energy directed at cracks and holes in the calorimeter. A time-over-threshold circuit placed on the CTC sense wires provides dE/dx

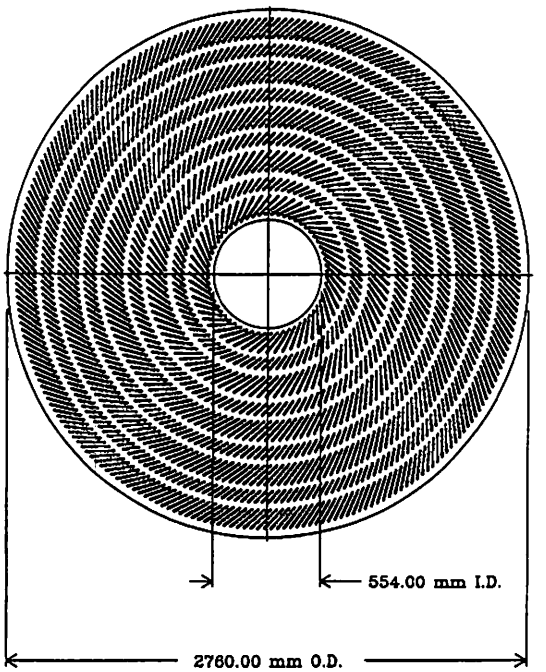

Figure 2.6: The CTC endplate showing the wire slots.

information. This dE/dx information is utilized in the low-P_T electron identification to discriminate against charged hadrons.

2.5 Calorimetry

Calorimetry coverage at CDF extends from $\sim 2°$ to $\sim 178°$ in θ and 2π in ϕ. The calorimeters are segmented into projective towers in η and ϕ, pointing to the nominal interaction point. CDF calorimetry can be divided into three segments based on pseudorapidity coverage: the central calorimeter provides coverage in the range $|\eta| < 1.1$, the plug in the region $1.1 < |\eta| < 2.4$ and the forward extends this coverage to $2.2 < |\eta| < 4.2$. Each calorimeter consists of an electromagnetic detector followed by a hadronic one. Properties of the

CDF calorimeter are summarized in Table 2.2.

System	η range	Energy Resolution ($\frac{\%}{\sqrt{E}}$+constant term	Position Resolution	Thickness
CEM	$\mid\eta\mid$<1.1	13.5%⊕2.0%	0.2cm×0.2cm	$18X_0$
PEM	1.1<$\mid\eta\mid$<2.4	28%⊕2%	0.2cm×0.2cm	18-$21X_0$
FEM	2.2<$\mid\eta\mid$<4.2	25%⊕2%	0.1cm×0.4cm	$25X_0$
CHA	$\mid\eta\mid$<1.1	75%⊕3%	0.2cm×0.2cm	$4.5\Lambda_{abs}$
PHA	1.1<$\mid\eta\mid$<2.4	90%⊕4%	0.2cm×0.2cm	$5.7\Lambda_{abs}$
FHA	2.2<$\mid\eta\mid$<4.2	130%⊕4%	0.2cm×0.2cm	$7.7\Lambda_{abs}$

Table 2.2: Calorimetry at CDF. ⊕ means add in quadrature and X_0 and Λ_{abs} are the radiation and absorption lengths respectively.

2.5.1 Central calorimeter

Figure 2.7 shows a perspective view of a central calorimeter wedge. The central calorimeter uses scintillators as the active material and phototube readout. It is segmented into two halves in the z-plane at $\eta = 0$. Each half is further segmented into 24 wedges covering 15° in ϕ and the η range from 0 to 1.1. Each wedge is divided into 10 towers along the z-axis. One wedge is notched to allow access to the coil, and consequently has only 8 towers.

The electromagnetic calorimeter (CEM) uses lead absorber intersperesd with polysterene scintillator. The CEM is made up of 31 layers of 0.5 cm thick scintillator interspersed with 30 sheets of 0.32 cm thick lead absorber. At the position of shower maximum for electromagnetic showers (CEM) lie proportional chambers, the Central Electromagnetic Shower counter (CES). A perspective view of CES is shown in Fig. 2.8. The CES consists of strip

perpendicular to the beam and wires along beam direction. The CES measures the shower position and transverse profile in z and ϕ with a position resolution of 2mm by 2mm. The shower centroid measured in the CES is then matched with tracks from the CTC to select electron candidates and is crucial to electron identification. The energy resolution of the CEM is $13.5\%/\sqrt{E} \oplus 2.0\%$.

The hadronic calorimeter (CHA) is mounted around the solenoid and consists of steel plates and acrylic scintillator. The CHA has the same tower segmentation as its electromagnetic counterpart. It covers the pseudorapidity range $| \eta | < 0.9$, with the endwall hadron calorimeter (WHA) extending this coverage out to $| \eta | < 1.3$. The CHA consists of 32 layers of 1cm thick scintillator interleaved with layers of 2.5cm thick steel. The WHA is made up of 15 layers of 5cm thick steel followed by 1cm thick scintillator. It presents 4.5 absorption lengths and has an energy resolution of $75\%/\sqrt{E} \oplus 3\%$.

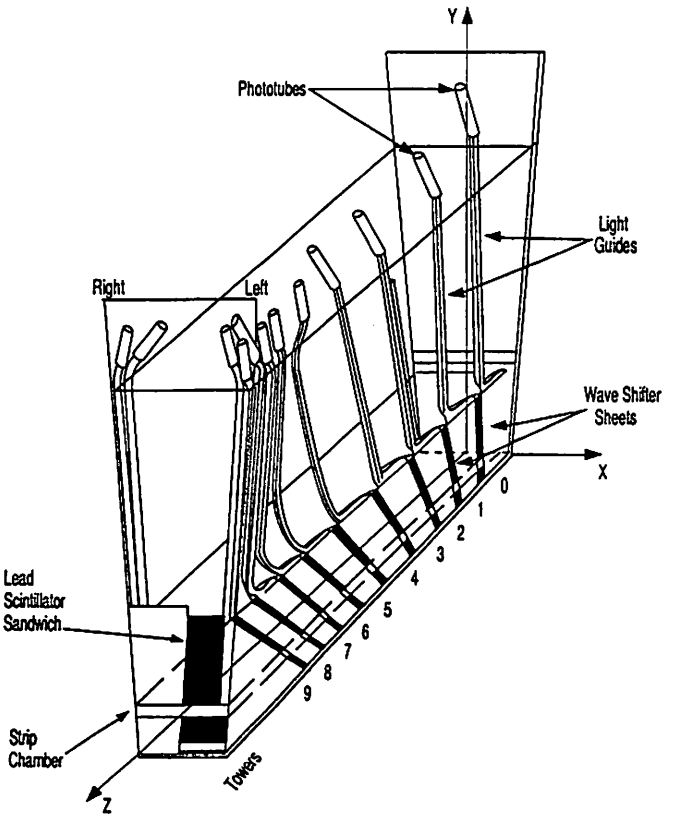

Figure 2.7: Perspective view of a Central calorimeter wedge.

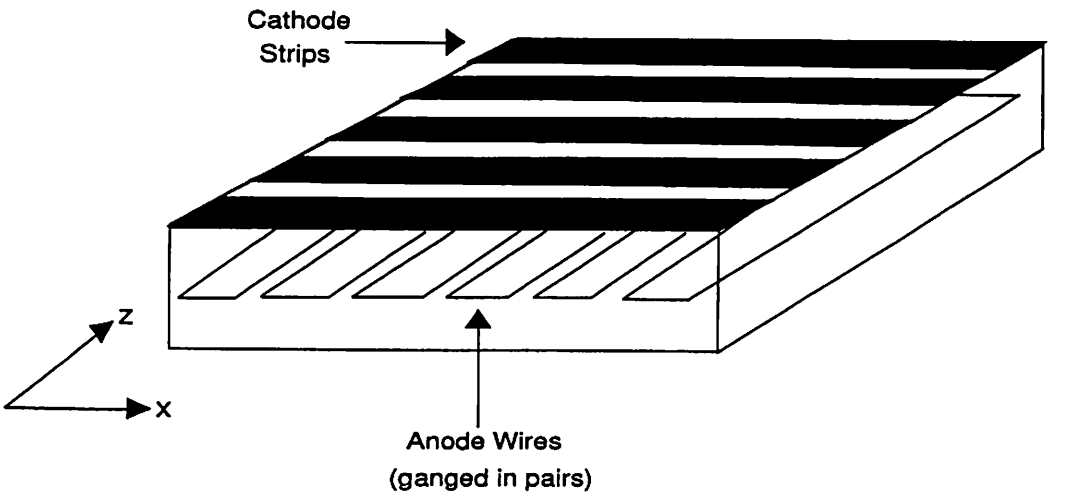

Figure 2.8: Perspective view of a CES chamber.

2.5.2 Plug calorimeter

The plug calorimeter is made up of gas proportional chambers with cathode pad readout. The electromagnetic calorimeter (PEM) uses lead absorber and conductive plastic proportional tube arrays. The PEM has an energy resolution of $28\%/\sqrt{E} \oplus 2.0\%$. Shower position is obtained from strip with a resolution of 2mm by 2mm.

The hadronic calorimeter (PHA) consists of steel plates and conductive plastic proportional tube arrays. The PHA has an energy resolution of $130\%/\sqrt{E} \oplus 4\%$.

The information of plug calorimeter is used only for jet measurement and missing transverse energy calculation in this analysis.

2.5.3 Forward calorimeter

The forward calorimeters consist of electromagnetic shower counter and hadron calorimeter.

Each of the forward calorimeters are composed of proportional chambers and steel plates. It designed to cover a pseudorapidity region of $2.2 \leq |\eta| \leq 4.2$ with full azimuthal angle.

The information of forward calorimeter is used only for missing transverse energy calculation in this analysis.

2.6 Central preradiator

The central preradiator (CPR) is made up of the proportional chambers and located between the solenoid and the CEM. The CPR samples the early development of electromagnetic showers in the material of the solenoid coil. The chambers provide $r - \phi$ information only. This information is only used to identify low P_T electrons coming from b-quark decays in this thesis.

2.7 Muon chamber

The muon chambers can be divided into three parts: the central Muon chamber(CMU), the Central Muon upgrade(CMP) and the Central Muon extension(CMX). The coverage of each detector is shown in Fig. 2.9.

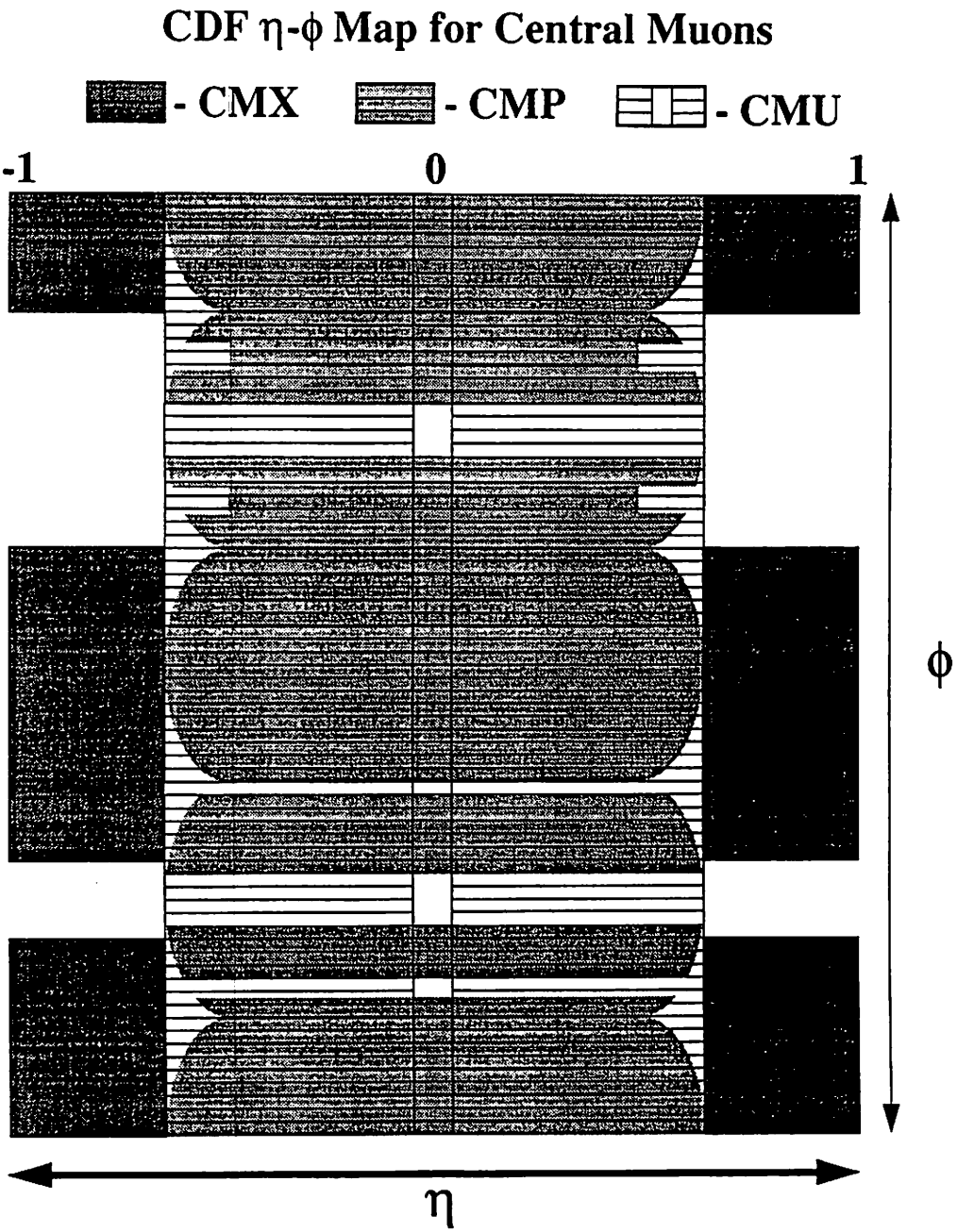

Figure 2.9: CDF $\eta - \phi$ map for central muon chambers.

2.7.1 Central muon chamber

The covered region of the central muon chamber is up to $|\eta| < 0.63$. The total coverage in ϕ is about 85%. The CMU chamber is located behind the central hadron calorimeter in each wedge. Due to the thickness of the calorimeters, only muons with P_T above 1.4 GeV/c can reach the muon chambers. The layout of the CMU system is shown in Fig. 2.10.

Each muon chamber is divided into three modules, each of which in turn consists of four layers of four rectangular drift cells parallel to the beam axis. There is a sense wire at the center of each cell. A cell of CMU is shown in Fig. 2.11. Particles traversing the muon chamber radially pass through all four cells. To resolve the left-right ambiguity in track azimuth measurement, the sense wires in the outer two cells are offset by 2mm with respect to the two inner wires. Sense wires in alternate cells of the same layer are connected at the ϕ=90° end of the chamber and are read out separately at the other end. The z position of a track is obtained by charge division. The angle α between a trajectory in a muon chamber and a reference plane containing the beam axis is related to the track P_T by:

$$sin\alpha = \frac{qBL^2}{2DP_T}$$

where q is the charge of the particle, B the magnitude of the magnetic field, L is the distance of the chamber from the beam line and D is the curvature of the track. The angle α is determined by measuring the difference in arrival times of drift electrons at the four sense wires crossed by a given muon, i.e

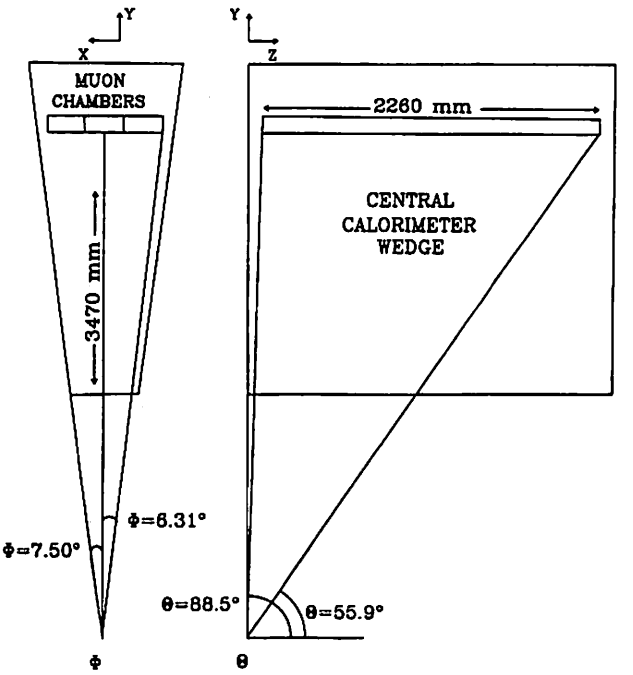

Figure 2.10: Layout of CMU system.

the greater of $t_4 - t_2$ and $t_3 - t_1$. (see Fig. 2.12)

The muon P_T is then inferred using the above formula and used in the trigger. The momentum resolution is dominated by multiple Coulomb scattering of muons in the calorimeter steel.

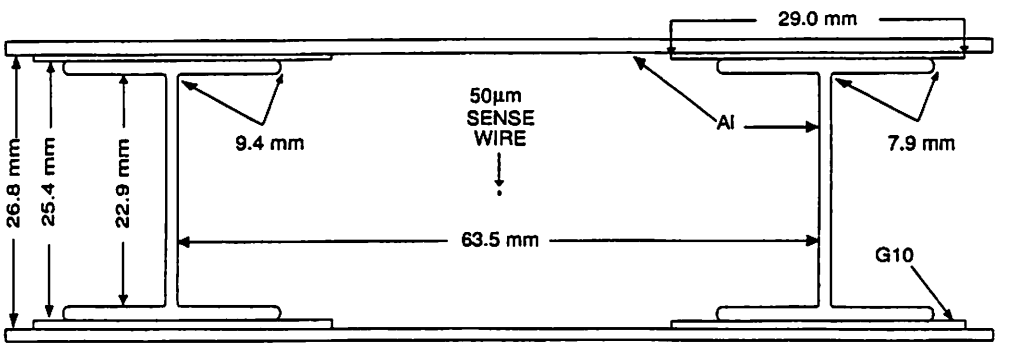

Figure 2.11: A cell of central muon chamber.

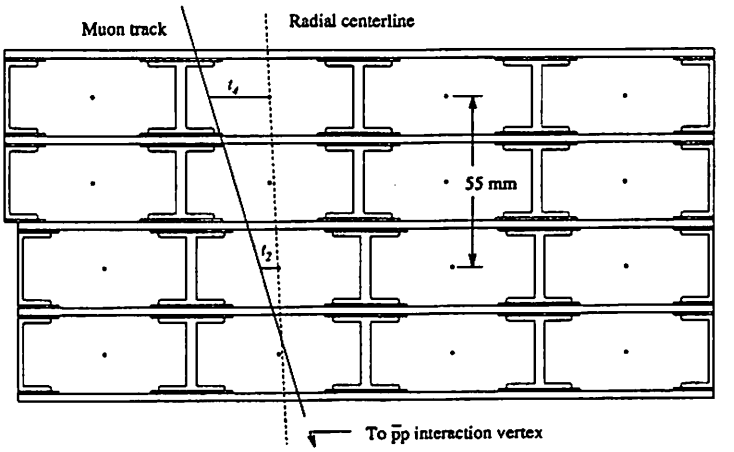

Figure 2.12: Cross section of CMU module showing the position of the sense wires.

2.7.2 Central muon upgrade

To minimize the "punch through" background which is caused by high P_T hadrons, the CMP was conceived and built. The CMP chambers consist of a four sided box around the CDF detector: north wall and south wall chambers and top yoke and bottom yoke chambers. On two sides of the detector are steel walls $\sim$ 535 cm from the interaction point. The CMP provides additional muon chambers behind 0.6 m of additional steel behind the CMU. Consequently muons with P_T less than $\sim$2.5 GeV/c cannot reach the CMP.

2.7.3 Central muon extention

The second thrust of the muon upgrade in CDF was extending the muon coverage. The central muon extension (CMX) was built and installed to alleviate this problem. The CMX consists of four free-standing arches and extends muon coverage from 0.6 to 1.0 in pseudorapidity and has 80% coverage in ϕ.

Chapter 3

Monte Carlo Simulation

The present particle physics analysis cannot be done without help of Monte Carlo programs which provide the theoretical information. An event simulator which can take into account the finite acceptance of the apparatus and variations in efficiencies across the detector is also used.

Samples of top quark events were generated with both HERWIG[15] and ISAJET[16]. W+jet events were generated according to the lowest-order matrix elements for the production of a W with n final-state partons. The complete sets of matrix elements at a tree level have been determined for n of 0 to 4 and are implemented in the program VECBOS[17]. To avoid infrared divergences which would occur at small angles and small P_T, cuts are applied in the event generation that require P_T(parton) > 10 GeV/c, $|\eta(parton)|$<3.5 and ΔR(parton-parton) > 0.4. We have used two different Q scales, $Q^2 = \langle P_T \rangle^2$ and M_W^2, for the α_s scale and take the difference as a systematic uncertainty. To transform the partons produced by VECBOS into

hadrons and jets, we use HERPRT[18] fragmentation model which uses part of QCD shower evolution Monte Carlo HERWIG. The Monte Carlo events have then been processed through a full simulation of the CDF detector and reconstructed in the same manner as the data.

3.1 Pseudo experiments

In order to check the analysis method and estimate various systematic uncertainties, we perform pseudo-experiments which use Monte Carlo events. For example, to check the analysis method, we make a sample which contains the signal and the background Monte Carlo events with an expected background fraction and we perform the analysis on the sample. Then we can check that the analysis method is doing correct things. Also we can estimate how much is the possibility of obtaining the result with the CDF data by comparing between the result of many pseudo-experiments and that of the CDF data within an assumption that Monte Carlo describes the real data correctly.

Chapter 4

Event Selection

The signature of top quark production which we used is a high P_T lepton, large missing transverse energy ($\not\!\!E_T$) and 4 or more jets. One of W bosons has decayed either to an $e\ \nu$ or a $\mu\nu$ pair, and the other W boson has decayed to quarks, giving rise to jets. Our event selection begins with high P_T lepton sample, then we look for the existence of W boson by requiring large missing transverse energy. The creation of these samples is described in this chapter, together with a brief description of the calculation and meaning of missing transverse energy and jet clustering algorithms applied at CDF. To suppress the W+multijet background, we search for b quarks using basically two methods. In the first method, we look for displaced vertices using SVX detector. The second method requires a low P_T lepton from b-quark decay.

4.1 W selection

Our trigger for searching for top quark requires a high P_T electron or muon which is a decay product of a W boson. In decay process of W boson, we expect high missing transverse energy caused by a neutrino.

4.1.1 High P_T lepton sample

We only consider electrons and muons detected in the central region with $E_T > 20$ GeV for electrons and $P_T > 20$ GeV/c for muons. These electrons and muons have to pass the standard trigger and offline lepton identification as described in the following subsections.

High P_T electron

All seed towers with an electromagnetic transverse energy of at least 3 GeV are considered to be EM energy clusters and adjacent towers are added to the cluster if E_T is above 0.1 GeV. Electrons from photon conversion can be rejected with a high efficiency of (88±4%) using tracking information. An electron which does not have a matching VTX track, or which can be paired with an oppositely charged CTC track to form a small effective mass, is considered coming from a photon conversion. We applied the following cuts to identify electrons against charged hadrons: The ratio of the hadronic energy to the electromagnetic energy of the cluster (HAD/EM) is required to be less than 0.05. The ratio of the cluster energy to the track momentum (E/P) should be less than 1.8. A deviation of the lateral shower profile in the calorimeter cluster from that of test beam electrons (L_{shr}) should be less than 0.2. The distance between the position of the extrapolated track

and the CES shower position measured in the ϕ and z views (Δx and Δz) should satisfy | Δx|< 1.5cm and | Δ z|< 3.0cm. A χ^2 comparison of the CES shower profiles with those of test beam electrons(χ^2_{strip}) should be less than 10. The distance between the interaction vertex and the reconstructed track in the z direction(z-vertex match) should be less than 5.0cm. The calorimeter isolation (I_{cal}) is defined as the sum of the transverse energies in the towers within a cone of radius 0.4 in $\eta - \phi$ plane around the electron but excluding the electron cluster transverse energy E_T. We require $I_{cal} < 0.1 \times E_T$. A summary of the electron selection criteria is listed in Table 4.1.

$\mid \eta \mid$	< 1.0
HAD/EM	< 0.05
E/P	< 1.8
L_{shr}	< 0.2
$\mid \Delta x \mid$	< 1.5 cm
$\mid \Delta z \mid$	< 3.0 cm
χ^2_{strip}	< 10
z-vertex match	< 5.0 cm
Isolation	$I_{cal}/E_T(e) < 0.1$

Table 4.1: Summary of electron selection criteria.

High P_T muon

We require a match between a CTC track and a track segment in the muon chamber of CMU,CMP or CMX. To identify muons, we require the following selection criteria: the energy in the calorimeter tower in the path of the extrapolated track should be consistent with that for a minimum ionizing particle. This is useful to separate muons from hadrons which interact in

the calorimeters, and cosmic rays. EM or HAD energy is required to satisfy EM < 2 GeV and HAD < 6 GeV. The closest approach of the reconstructed track to the beam line(impact parameter) should be less than 3mm. The distance between the interaction vertex and the reconstructed track in the z direction(z-vertex match) should be less than 5.0 cm. The matching distance between the extrapolated track and the track segment in the muon chambers(Δx=r$\times\Delta\phi$) should be less than 2cm for CMU and less than 5cm for CMP and CMX. Isolation(I_{cal}), defined as the sum of the transverse energy deposited within a cone of 0.4 excluding transverse energy by muon tower (I_{cal}) should satisfy $I_{cal} < 0.1\times P_T$. A summary of the muon selection criteria is listed in Table 4.2.

$\mid \eta \mid$	< 1.0
EM energy deposit	< 2 GeV
HAD energy deposit	< 6 GeV
Impact parameter	< 3 mm
z-vertex match	< 5.0 cm
$\mid \Delta x \mid$	< 2.0 cm (CMU)
	< 5.0 cm (CMP,CMX)
Isolation	$I_{cal}/P_T(\mu) < 0.1$

Table 4.2: Summary of muon selection criteria.

4.1.2 Missing transverse energy

The $\not\!\!E_T$ variable is used to estimate the total transverse momentum of all neutrinos in the event. It is calcuated as

$$\not\!\!E_T^{raw} \equiv \mid \vec{\not\!\!E}_T^{raw} \mid \equiv \mid -\sum_i \vec{E}_{T_i} \mid,$$

where $\vec{E}_{T_i}$ is the vector of the transverse energy deposited in the i-th tower and the sum is over all towers within the pseudo-rapidity range $\mid \eta \mid < 3.6$. The $\not\!\!E_T{}^{raw}$ contains the momentum of muons which pass the calorimeter. To subtract muon momenta from $\not\!\!E_T$, we correct it as follows:

$$\vec{\not\!\!E}_T = \vec{\not\!\!E}_T^{raw} - \vec{P}_T^{\mu} + \vec{E}_T^{\mu}$$

where $\vec{P}_T^{\mu}$ is transverse momentum of the muon reconstructed with a condition that the muon track is constrained to the beam line. $\vec{E}_T^{\mu}$ is sum of calorimeter energies deposited by the muon. Nonlinear calorimeter response to low energy particles and the cracks between detector components make the observed $\not\!\!E_T{}^{raw}$ an inaccurate measure of the neutrino transverse energy. $\not\!\!E_T$ is corrected by taking into account the correction of the electron energy, the jet energy and underlying event energy from the spectator partons and the low energy jets. Underlying event energy vector $\vec{E}_T^{ul}$ is defined by

$$\vec{E}_T^{ul} = -(\vec{\not\!\!E}_T + \sum \vec{E}_T^{jet} + \sum \vec{E}_T^{ele})$$

Each piece is corrected individually and the corrected missing transverse energy $\not\!\!E_T{}^{corr}$ is given by

$$\vec{\not\!\!E}_T^{corr} = -(\vec{E}_T^{elecorr} + \sum \vec{E}_T^{jetcorr} + \alpha \cdot \vec{E}_T^{ul})$$

where $\vec{E}_T^{elecorr}$ is the transeverse energy of electron corrected with calibration factor tower by tower, $\vec{E}_T^{jetcorr}$ is the corrected jet transverse energy and α is the scale factor for the underlying event set to 1.6.

For the event selection, we require uncorrected $\not\!\!E_T^{raw} > 20$ GeV.

4.1.3 Z vertex position and Z^0 removal

We require the event z vertex position to be within 60 cm of the center of the CDF detector. In addition, we removed Z boson candidates by rejecting events with an oppositely-charged dilepton (ee or $\mu\mu$) invariant mass in the range between 75 GeV/c^2 and 105 GeV/c^2.

4.2 Jet selection

4.2.1 Jet identification

Jets are defined as a cluster of energy in EM and HAD calorimeters by a clustering algorithm with a cone radius R of 0.4. Jet clustering involves finding seed towers, forming pre-clusters, extending pre-clusters to clusters and resolving overlap region between clusters. First all towers with $E_T >$ 1GeV are defined as seed towers. Seed towers adjacent to each other on

a corner or side are grouped into a pre-cluster. Pre-clusters are expanded to clusters using a fixed-cone iterative algorithm. In $\eta - \phi$ plane, the E_T weighted center of pre-cluster is computed. A cluster then includes all towers with $E_T > 100$ MeV within a cone of radius 0.4 around the pre-cluster. The cluster centroid is recomputed and its set of towers redefined accordingly. This procedure is repeated until the set of towers in a cluster does not change. The initial pre-cluster is always kept in the cluster regardless of its distance to the centroid. This prevents the centroid from shifting too far away in pathological situations. If a cluster is a subset of another cluster, only the larger cluster is kept. If two clusters share towers, they are merged if the total E_T in common towers is larger than 50% of the smaller cluster E_T. Otherwise towers in the overlap region are assigned to the closest cluster in $\eta - \phi$ space. The cluster centroids are recomputed until a stable configuration is reached.

4.2.2 Energy correction

Jet energy may be mismeasured due to the following effects:

- non-linearity of the calorimeter.
- low calorimeter response at a crack.
- contribution from an underlying event.
- energy loss outside a cone.
- undetected energy of μ or ν.

To correct the jet energy, we used a jet energy correction factor which depends on the jet E_T and η to reproduce the average jet E_T correctly, not to reduce the jet fluctuations around this mean E_T. The jet corrections are fully described in Ref.[28] and [29].

We have used an additional jet energy correction which was obtained by comparing between parton momenta and measured jet E_T on Monte Carlo $t\bar{t}$ events. We also know the resolution of jet energy scale from this comparison. This jet energy correction is applied after the general jet energy corrections as described above. The jet energy resolution is used to calculate the function for the MINUIT fitter. The correction function and energy resolution function are a function of jet E_T as shown in Fig. 4.1. These functions are specific functions for b jets and light quark jets from W boson.

Using these function, we have found that the reconstructed mass distribution has closer mean value to generated mass value in comparison with the case we do not use the additional energy correction.

4.2.3 4 jet selection

For the top quark mass reconstrcution, we applied the 4-jet cut which requires $E_T^{uncorr} > 15$ GeV and $|\eta| < 2.0$ for leading 3 jets and $E_T^{uncorr} > 8$ GeV and $|\eta| < 2.4$ for the 4th jet. A summary for the jet selection criteria is listed in Table 4.3.

For leading 3 jets	$E_T^{uncorr} > 15$ GeV	$\mid \eta \mid < 2.0$
For 4th jet	$E_T^{uncorr} > 8$ GeV	$\mid \eta \mid < 2.4$

Table 4.3: Summary of jet selection criteria.

4.3 b-tagging

To separate the $t\bar{t}$ signal from the backgrounds, b-tagging is one of the most powerful techniques. In the standard top quark mass analysis, we have used two different kinds of b-tagging algorithms. The first looks for displaced vertices in the SVX detector which is called "SVX tag". The second method searches for low P_T leptons from b-quark decay which is called "SLT tag".

In this analysis, we used an additional b-tagging method to increase the b-tagging efficiency. "Loose jet probability tagging" requires looser cuts than a standard jet probability b-tagging algorithm.

4.3.1 SVX tagging

SVX tagging algorithm[19] performs secondary-vertex fitting with three or more SVX tracks which passed track selection cuts. If that fails, it looks for two or more track vertices using tighter track quality cuts and vertex quality requirement. Basically this algorithm is applied to sets of SVX tracks associated with jets that have $E_T \geq 15$ GeV and $\mid \eta \mid$<2.0. The SVX tracks must have at least one track with P_T >2 GeV/c and an impact parameter significance $\mid d \mid / \sigma_d \geq 2.5$. Using these tracks, we calculate the distance from the primary vertex L_{xy} and require the absolute significance of L_{xy} to

be greater than 3.

4.3.2 SLT tagging

Soft Lepton Tagging algorithm[20] looks for low P_T non-isolated electrons and muons which are the decay products of b-quarks through $b \rightarrow l\nu_l X$ ($l = e$ or μ), or $b \rightarrow c \rightarrow l\nu_l X$.

To search for electrons from b and c decays, we extrapolate each particle track reconstructed in the CTC to the calorimeter and attempt to match it to a CES shower cluster. The matched CES clusters are required to be consistent in size, shape, and position with expectations for electron showers. Electron candidates must also match to an energy deposition in the CPR corresponding to at least four minimum ionizing particles.

To identify muons from b and c decays, track segments reconstructed in the CMU and CMP systems are matched to tracks in the CTC. To maintain a high efficiency for nonisolated muons from b and c decays, we do not apply the minimum ionizing requirements which are intended for isolated muons from W decay. These requirements are designed to reduce high-P_T hadronic punch-through, which is also effectively reduced by requiring a match between the CTC track and the CMP track segment. For CMU-only muons in the regions not covered by the CMP system, we apply an isolation-dependent requirement on muon candidates with $P_T > 6$ GeV/c that do not have a matching CMP track segment; we require $E_{had} < 6$ GeV $+ \sum p$, where E_{had} is the hadronic energy of the tower traversed by the muon and $\sum p$ is the scalar sum of the momenta of all tracks within a cone of radius 0.2 around

the muon candidate. The difference between RUN1A and RUN1B collider runs is the CMX system. We also use CMX muons in order to increase the acceptance.

4.3.3 Loose jet probability tagging(JPB tagging)

Loose jet probability tagging algorithm uses looser cuts than a standard jet probability tagging algorithm[21]. The jet probability tagging algorithm uses a track signed impact patameter to determine the probability that the track is consistent with originating from the primary vertex. In this algorithm, the sign of the impact parameter is defined to be positive if the point of the closest approach to the primary vertex lies in the same hemisphere as the jet direction, and negative otherwise. Tracks from long-lived objects will usually have a positive impact parameter. Using looser cuts, a jet is tagged by this algorithm if it has an overall jet probability less than 5% and two or more tracks with positive impact parameter and $P_T \geq 1.5$ GeV/c.

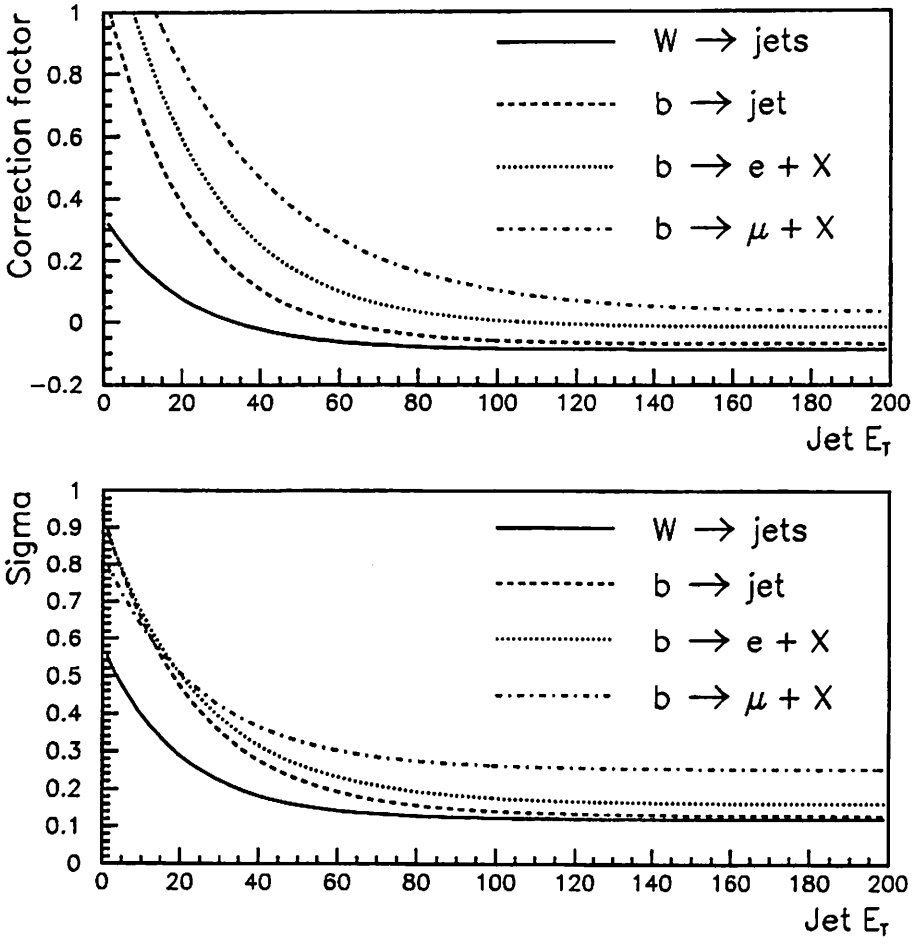

Figure 4.1: Top plot shows the correction function as a function of jet E_T, which is applied as a specific energy correction in $t\bar{t}$ events. Bottom plot shows the energy resolution function as a function of jet E_T, which is used in top mass fitting.

Chapter 5

Hadronic W Decay in $t\bar{t}$ Events

5.1 Motivation

One of the largest uncertaities on top quark mass measurement is a jet energy scale uncertainty. Finding a W mass peak in the dijet mass distribution for $W+\geq$4jet events is a technique to examine the jet energy scale in $t\bar{t}$ events and prove that $t\bar{t}$ candidates have 2 W's in the final state. We have worked on $W+\geq$4jet events as top candidates but we have not proved that one of the W bosons decays into a quark pair.

5.2 H variable

The H variable[26] has been used for making a separation between $t\bar{t}$ events and W+jets background. It is defined as a total transverse energy of

observed objects as follows:

$$H = E_T(e) + P_T(\mu) + \not\!\!E_T + \sum E_T(jet)^{cor}$$

where jets must have $E_T > 8$ GeV and $|\eta| < 2.4$.

In this analysis, we optimize the H threshold with Monte Carlo events to separate $t\bar{t}$ events from the W+jets background.

5.3 Method

Figure 5.1 shows the dijet mass distribution of the CDF W+≥4jet data. This distribution was fitted to a sum of the expected distributions obtained from HERWIG $t\bar{t}$ production (M_{top}=175 GeV/c^2) and VECBOS W+jets backgrounds ($Q^2=\langle P_T \rangle^2$). Details are described below. Figure 5.2 shows the expected dijet mass distributions (a) for VECBOS W+jets backgrounds, (b) for HERWIG $t\bar{t}$ production (W signal + combinatorial background), (c) for W signal from HERWIG $t\bar{t}$ production and (d) for combinatorial background from HERWIG $t\bar{t}$ production.

The fitting procedure is as follows:

1. We use the H variable[26] to enhance the ratio of signal to background. We show the results with and without the optimized H cut.

2. We performed an unbinned likelihood fit excluding the dijet mass region between 60 GeV/c^2 and 100 GeV/c^2 to find the most probable background fraction α. The dijet mass distributions of the W+jet back-

ground and the combinatorial background from $t\bar{t}$ events were used as a probability function.

3. We subtracted backgrounds to extract the excess around a $W \rightarrow$jj mass peak.

4. We performed an unbinned likelihood fit for all mass region using the sum of the above background probability function and a Gaussian for W$\rightarrow$jj signal as a probability function. The mean and sigma of a Gaussian are fit parameters.

5. We define the excess by $S/\Delta(S+B)$ and the significance by $S/\Delta(B)$, where S is the number of signal events and B is the number of background events in the mass region between 70 GeV/c^2 and 90 GeV/c^2.

5.3.1 Mass window optimization

To determine the mass window for calculating the significance, we performed 1000 pseudo-experiments with Monte Carlo $t\bar{t}$ events using the HERWIG event generator. We obtained results on the following three samples:

1. Events before b-tagging with a background fraction of 68%
   (normal HERWIG pretagged W+4jet events).

2. Events before b-tagging with a background fraction of 68%
   where each $t\bar{t}$ event has a $W \rightarrow$2jets signal
   (HERWIG pretagged W+4jet events with no gluon radiation)

3. Single b-tagged events with a background fraction of 19%

The significances are plotted against the mass window in Fig. 5.3 for the first sample, Fig. 5.4 for the second sample and Fig. 5.5 for the third sample, respectively. On the normal HERWIG W+4jet events, we have the optimized mass window around 70~90 GeV/c^2. On the HERWIG pretagged events with no gluon radiation, we can see the optimized mass window more clearly. The highest significance is obtained in 71~89 GeV/c^2. On single b-tag events, the optimized mass window is seen around 70~90 GeV/c^2.

We selected the mass window of 70~90 GeV/c^2 which gives the highest significance on the HERWIG pretagged sample with no hard gluon effect and the b-tagged sample, which is consistent with the result on the normal pretagged events.

5.4 $W+\geq$4jet events without b-tagging requirement

5.4.1 Results without H cut

The fitting result is shown in Fig. 5.6. The fraction of background events is estimated to be 0.66±0.08. The number of $W \rightarrow$ 2 jets was estimated to be 33±20 corresponding to an excess of 1.7σ. The significance was 1.9σ. The fitting result gives a mean of 79.7±3.6 GeV/c^2 and a sigma of 6.9±2.1 GeV/c^2. The mean and the sigma are consistent with those of a W mass peak obtained from Monte Carlo of 80.4 GeV/c^2 and 11.7 GeV/c^2, respectively. By fitting with a W mass peak width fixed to 11.7 GeV/c^2, we obtained 79.6±5.1 GeV/c^2.

5.4.2 Results with H cut

Figure 5.7 shows H distribution for the CDF pretagged $W+\geq$4jet events and a Monte Carlo sample of 53 $t\bar{t}$ events and 111 W+jets background events. We expect the number of $t\bar{t}$ events to be 53 and the number of background events to be 111 out of 164 events from the Reference[27].

We optimize the H threshold and the mass region where we count the excess and the significance. We performed an unbinned likelihood fit with various H thresholds and calculated the significance in the mass region and compared them on the ~200 samples of Monte Carlo pretagged $W+\geq$4jet events. The result is shown in Table 5.1. α indicates an estimated background fraction on pseudo experiments. The significance and the excess show the mean of 100 pseudo experiments.

We obtained the optimized H threshold value of 310 GeV. We show the distributions of α and the significance for ~200 pseudo experiments after H>310 GeV cut in Fig. 5.8 and Fig. 5.9.

We also evaluated the significance using real data. From the results, we obtained the excess of 2.2σ and the significance of 2.8σ using 310 GeV cut as shown in Table 5.2. This result shows the number of $W \rightarrow$jj signal is 29±13. The background fraction, a mean and a sigma of the peak were estimated to be 0.27±0.14, 75.2±2.7 GeV/c^2 and 6.8±2.1 GeV/c^2, respectively. When we fixed the sigma of Gaussian to 11.7 GeV/c^2, the mean value was found to be 77.1±3.8 GeV/c^2. This value was consistent with that of Monte Carlo. Fitting result after H> 310 GeV cut is shown in Fig. 5.10. We summarized these results in Table 5.3 together with the estimated number

threshold	α	excess	significance
0	0.61±0.08	1.14±0.03	1.28±0.04
220	0.55±0.10	1.25±0.03	1.42±0.04
230	0.53±0.10	1.26±0.03	1.44±0.04
240	0.51±0.11	1.26±0.03	1.45±0.04
250	0.48±0.12	1.28±0.03	1.48±0.04
260	0.47±0.13	1.30±0.03	1.51±0.04
270	0.45±0.14	1.30±0.03	1.53±0.04
280	0.43±0.15	1.28±0.03	1.52±0.04
290	0.42±0.15	1.29±0.03	1.54±0.05
300	0.42±0.16	1.29±0.03	1.54±0.05
310	0.40±0.16	1.27±0.03	1.55±0.05
320	0.39±0.18	1.23±0.03	1.51±0.05
330	0.38±0.18	1.17±0.04	1.43±0.05
340	0.37±0.19	1.12±0.03	1.39±0.05
350	0.37±0.20	1.11±0.03	1.38±0.05

Table 5.1: The results for various H thresholds on Monte Carlo pretagged $W+\geq$4jet samples. α indicates the fraction of background events. The background events were used with $Q^2=\langle P_T\rangle^2$.

of $t\bar{t}$ events.

threshold	α	Mean(Fixed σ)	Mean	Sigma	excess	significance
250	0.55±0.12	82.0±5.5	79.8±4.2	7.6±2.2	1.5	1.7
260	0.53±0.12	82.9±5.6	80.2±4.0	7.6±2.2	1.7	2.0
270	0.49±0.13	82.0±5.2	79.3±4.1	8.0±2.3	1.8	2.2
280	0.47±0.14	79.9±5.0	73.5±1.4	3.6±1.6	1.7	2.1
290	0.26±0.13	77.6±4.1	75.3±3.1	6.8±2.1	2.1	2.6
300	0.28±0.14	77.7±4.1	75.3±3.1	6.7±2.2	2.0	2.5
310	0.27±0.14	77.1±3.8	75.2±2.7	6.8±2.1	2.2	2.8
320	0.23±0.14	77.1±4.1	76.0±3.1	7.8±2.4	2.1	2.7

Table 5.2: The results for various H thresholds on CDF data. α indicates the fraction of background events. The background events were modeled with VECBOS with $Q^2=\langle P_T\rangle^2$.

H cut	0	310
Background fraction	0.63±0.07	0.27±0.14
N(total)	164	81
N($t\bar{t}$)	61±11	58±11
Number of signal	35±19	29±13
Mean of the mass peak	79.9±4.7	77.1±3.8
significance	2.0 σ	2.8σ

Table 5.3: Expected number of $t\bar{t}$ events which was obtained from estimated background fraction. Number of signal in the mass region and the mean of the mass peak are also shown.

The number of background events in 153 events which pass the $\chi^2 <$ 10.0 cut in the top quark mass fitting is 100±9 [27]. We can assume that

the events with $\chi^2 > 10.0$ are background, because the event with large χ^2 does not have a kinematic system like a $t\bar{t}$ production. The efficiency that 2 jets from W decay are in leading 4 jets and the invariant mass is between 70 GeV/c^2 and 90 GeV/c^2 was estimated to be 39% from HERWIG $t\bar{t}$ Monte Carlo data. Using this efficiency, the expected number of signal is 24±4 without the H cut. This is consistent with the above result. Furthermore as the efficiency for H>310 GeV cut is 40%, we can expect the number of signal after H>310 GeV cut is 23±4. This is also consistent with the above result.

So far we have performed this analysis using the VECBOS W+3jet background with $Q^2=\langle P_T\rangle^2$. To see the effect of different Q^2 definition, we made a fitting to the W+3jet background with $Q^2=Mw^2$. The results are listed in Table. 5.4. We found that H>310 GeV cut gives the excess of 2.2σ. The result is shown in Fig. 5.11. The fraction of background events and the significance were estimated to be 0.21±0.14 and 2.9 σ, respectively. The Gaussian has the mean and the sigma of 75.4±2.7 GeV/c^2 and 6.9±2.0 GeV/c^2. When we fixed the sigma of Gaussian to 11.7 GeV/c^2, the mean value was found to be 77.0±3.7 GeV/c^2. These values are consistent with the results obtained using the VECBOS W+3jet background with $Q^2=\langle P_T\rangle^2$.

We summarized these results in Table 5.5 together with the estimated number of $t\bar{t}$ events.

threshold	α	Mean(Fixed σ)	Mean	Sigma	excess	significance
250	0.53±0.11	81.7±5.4	79.6±4.1	7.7±2.3	1.6	1.8
260	0.50±0.12	82.7±5.3	80.3±3.8	7.7±2.2	1.8	2.1
270	0.46±0.13	81.8±5.1	79.3±4.0	8.2±2.4	1.9	2.3
280	0.43±0.13	79.9±4.9	76.4±4.5	6.9±2.9	1.8	2.1
290	0.24±0.12	77.5±4.0	75.3±3.1	6.8±2.1	2.1	2.6
300	0.27±0.13	77.4±4.0	75.3±3.0	6.8±2.2	2.0	2.6
310	0.27±0.14	77.0±3.7	75.4±2.7	6.9±2.0	2.2	2.9
320	0.21±0.14	76.8±4.1	75.9±3.0	7.7±2.3	2.1	2.8

Table 5.4: The results for various H thresholds. α indicates the fraction of background events. The background events were used with Q^2=Mw^2.

H cut	0	310
Background fraction	0.65±0.08	0.27±0.14
N(total)	164	81
N($t\bar{t}$)	57±13	59±11
Number of signal	38±19	29±13
Mean of the mass peak	79.6±4.6	77.0±3.7
significance	2.1 σ	2.9 σ

Table 5.5: Expected number of $t\bar{t}$ events which was obtained from estimated background fraction. Number of signal in the mass region and the mean of the mass peak are also shown.

5.5 W +≥4jet events with b-tagging requirement

There are 29 single b-tagged events in 110 pb^{-1} data where at least one jet is identified as a b-jet by the b-tagging algorithm. The dijet mass distribution is shown in Fig. 5.12.

The fit result is shown in Fig. 5.13. This fitting gives the background fraction of 0.00 + 0.19, the S$\pm\Delta(S+B)$ of 9$\pm$5 corresponding to an excess of 1.9σ, S$\pm\Delta B$ of 9$\pm$4 corresponding to a significance of 2.4σ. By fitting with a width of a W mass peak fixed to 11.7 GeV/c^2, we obtained a W mass of 73.1$\pm$5.0 GeV/c^2.

If we constrain the background fraction to (19$\pm$6)% which was estimated by Reference[27], the fit gives a background fraction, the number of signals, excess and significance of 0.17$\pm$0.06, 9$\pm$5, 1.8σ and 2.3σ, respectively. The result is shown in Fig. 5.14. By fitting with a width of a W mass peak fixed to 11.7 GeV/c^2, we obtained a W mass of 74.6 $\pm$ 5.2 GeV/c^2.

We summarized these results in Table 5.6 together with the estimated number of $t\bar{t}$ events.

Background shape	unconstraint	constraint
Background fraction	0.00+0.19	0.17±0.06
N(total)	29	29
N($t\bar{t}$)	29^{+0}_{-6}	24±2
Number of signal	9±5	9±5
Mean of the mass peak	73.1±5.0	74.6±5.2
significance	2.4 σ	2.3 σ

Table 5.6: Expected number of $t\bar{t}$ events which was obtained from estimated background fraction. Number of signal in the mass region and the mean of the mass peak are also shown.

5.6 W +≥4jet events with double b-tagging requirement

There are 11 double b-tagged events in 110pb^{-1} data where two jets are identified as b-jets. The dijet mass distribution was fitted with sum of the dijet mass distribution of $t\bar{t}$ and that of W+jets background events. The result gives a W mass of 78.1±5.1(stat)±4.0(syst) GeV/c^2[22]. The fit result is shown in Fig. 5.15.

5.7 Background shape

5.7.1 W+jets background shape

Figure 5.16 shows a comparison of the dijet mass distributions between Z+4jet real data and VECBOS W+jets background. They are consistent with each other within a statistical error.

5.7.2 Combinatorial background shape

Using b-tagged events, we can compare the combinatorial background shapes between Monte Carlo events and CDF real data. The top plot of Fig. 5.17 shows combinatorial background shape(point) obtained by making a dijet mass of an SVX tagged jet and another jet. This combinatorial background shape includes the contribution from W+jets backgrounds due to b-mistag. Histogram shows a sum of the combinatorial background from HERWIG $t\bar{t}$ events(M_{top}=175 GeV/c^2) and the VECBOS W+jets background. We used the W+jets background fraction of 0.25[11]. The bottom plot shows the same plot using SLT tagged jets. We used the W+jets background fraction of 0.67[11].

5.8 Systematic uncertainty in $W \rightarrow$jj mass

5.8.1 H variable uncertainty

In calculation of H variable, we did not use the top specific jet energy correction. This means we have independent uncertainty in H variable. We have to take into account the H variable uncertainty for W mass error estimation.

1. change the jet energy scale by $\pm$10% and calculate H variable for Monte Carlo events.

2. obtain a new H distribution and get the H threshold which corresponds to H=310 GeV in the original H distribution.

3. using this H threshold, make a fitting.

From the efficiency curve of H for $t\bar{t}$ and background events, we found H > 330(290) GeV cut corresponds to H > 310 GeV cut on +10%(−10%) energy shift sample. From the result of both fittings, we found a mean of mass peak is 78.1±4.0 GeV/c^2 (76.6±5.0 GeV/c^2). Thus we estimate the uncertainty in W →jj mass due to H uncertainty to be $^{+1.0}_{-0.5}$ GeV/c^2.

5.8.2 VECBOS W+jets background shape

Systematic error should include the difference coming from the uncertainty in the W+jets background shape. In a comparison of the results between $Q^2=\langle P_T \rangle^2$ and M_W^2 after H>310 GeV cut, we obtained the error of 0.1 GeV/c^2. Another uncertainty comes from the jet multiplicity. We estimated it to be 0.3 GeV/c^2 by the comparison of the results with the W+3jet background shape to that with the W+4jet background shape.

5.8.3 Combinatorial background shape

We also have to take into account the uncertainty in the combinatorial background shape. We performed the fitting using $t\bar{t}$ Monte Carlo data at M_{top}=160 GeV/c^2 and 190 GeV/c^2. Estimated mean value of Gaussian is 77.1±5.0 (77.5±3.5) GeV/c^2 for the combinatorial backgrounds at M_{top} =160(190) GeV/c^2. We estimated the uncertainty in W →jj mass due to the combinatorial background shape uncertainty to be $^{+0.7}_{-0.4}$ GeV/c^2.

5.8.4 Other fitting method

From the W mass difference between the fits with and without fixing a sigma to 11.7 GeV/c^2, we take the W mass systematic error of $\pm$1.9 GeV/c^2.

5.8.5 Jet energy scale

The $W \rightarrow$jj mass peak value is affected by jet energy scale. In the same method as top quark mass analysis which will be describe at Chapter 8, we perform pseudo-experiments and estimate this uncertainty to be $\pm$2.1 GeV/c^2.

5.8.6 Total systematic uncertainty

We obtained the total systematic uncertainty by adding the above uncertainties in a quadrature as listed in Table 5.7. Thus we obtained $W \rightarrow$jj mass peak of $77.1 \pm 3.8(\text{stat})^{+3.0}_{-2.9}(\text{sys})$ GeV/c^2.

5.9 Summary

We searched for a W mass peak in the dijet invariant mass distribution for the $W+\geq$4jet events. We analysed 164 events in total. We compared the background shape in the CDF real data with that in Monte Carlo events and found they are consistent with each other. We observed (29$\pm$13) $W \rightarrow$jj signals after H>310 GeV cut by an unbinned likelihood fitting with $Q^2=\langle P_T \rangle^2$ background shape. It corresponds to 2.2σ excess and 2.8σ significance. The number of $W \rightarrow$jj signal events is consistent with the expected one. The dijet

Systematic error in $W \rightarrow$jj mass	
H value	$^{+1.0}_{-0.5}$
W+jets background shape	± 0.3
combinatorial background shape	$+0.4$
fitting method	± 1.9
jet energy scale	± 2.1
total	$^{+3.0}_{-2.9}$

Table 5.7: The list of systematic uncertainties in $W \rightarrow$jj mass.

mass peak has a mean of $77.1 \pm 3.8(\text{stat})^{+3.0}_{-2.9}(\text{sys})\text{GeV/c}^2$ which is consistent with the expected W mass peak.

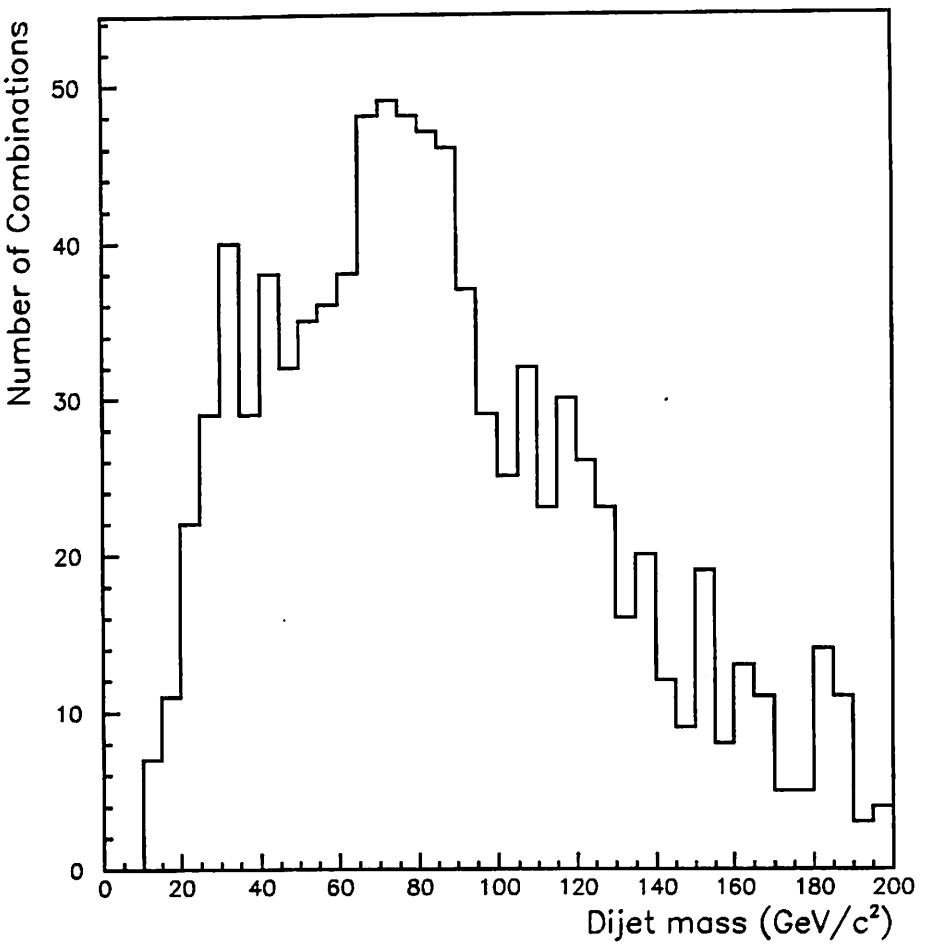

Figure 5.1: The dijet mass distribution for pretagged events.

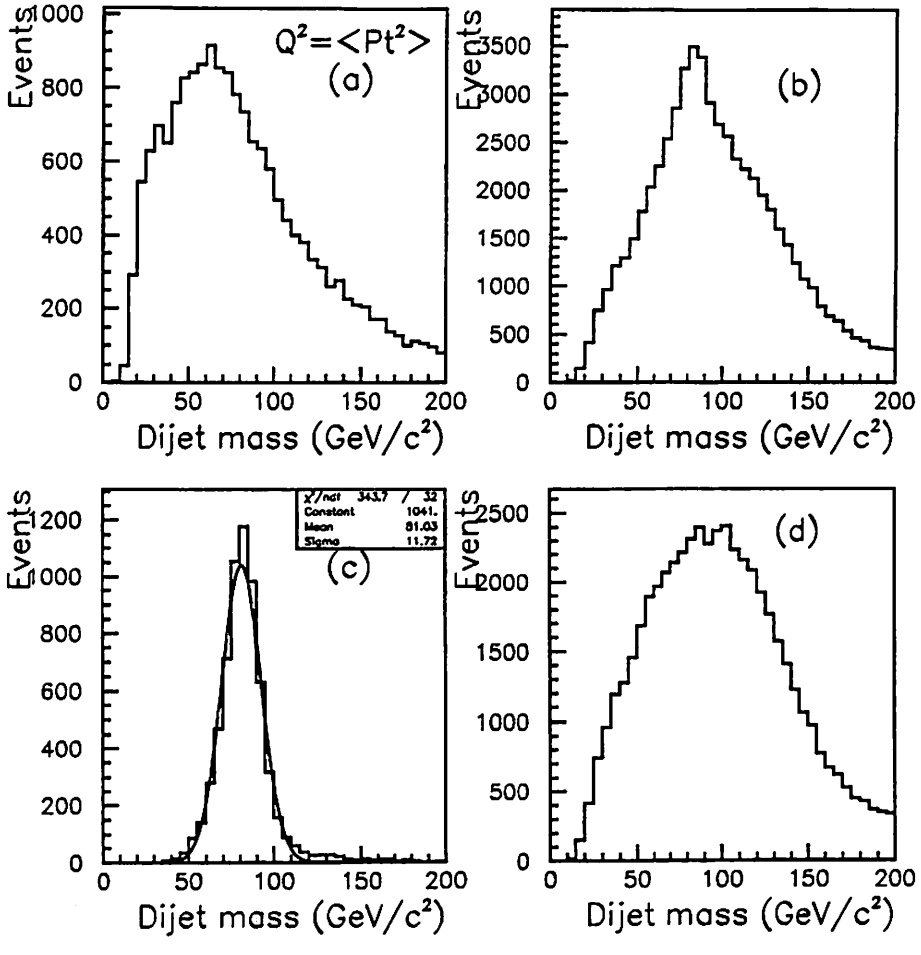

Figure 5.2: The dijet mass distributions for (a) VECBOS W+3jet ($Q^2=\langle P_T \rangle^2$) (b) HERWIG M_{top}=175 GeV/c^2. (c) $W \rightarrow$jj signal on HERWIG. (d) combinatorial background.

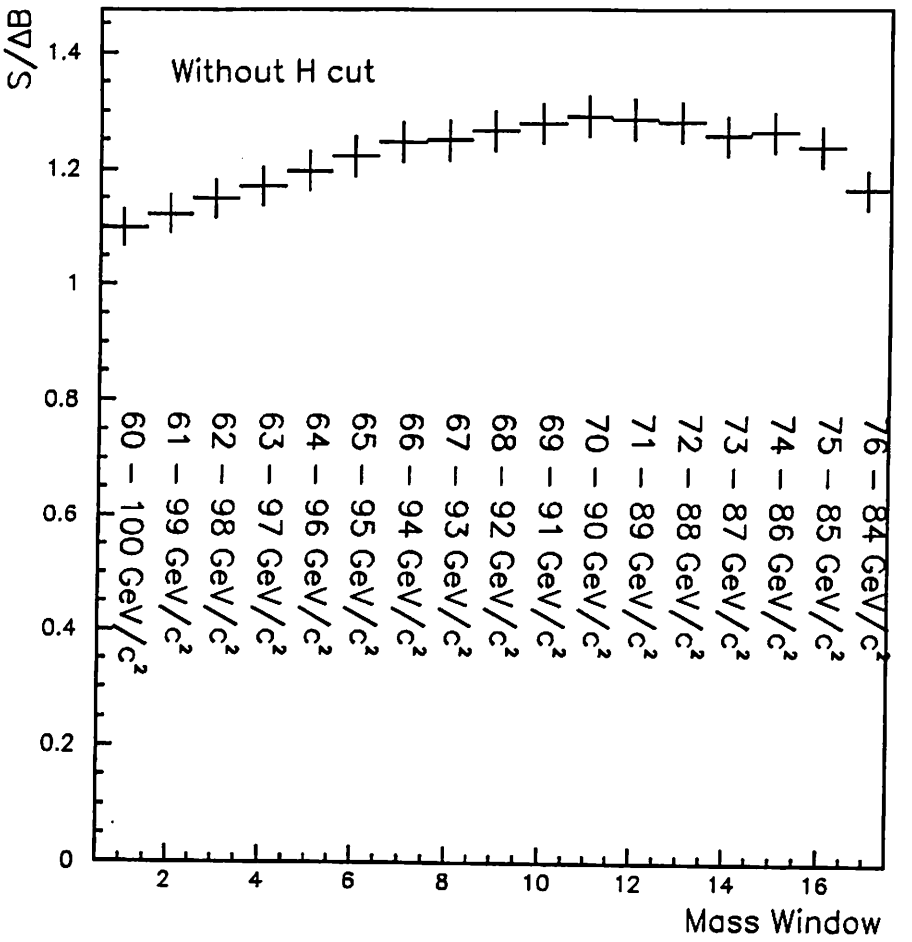

Figure 5.3: The average of significance versus mass window obtained in 1000 Monte Carlo pseudo experiments. The background fraction was set to 68%.

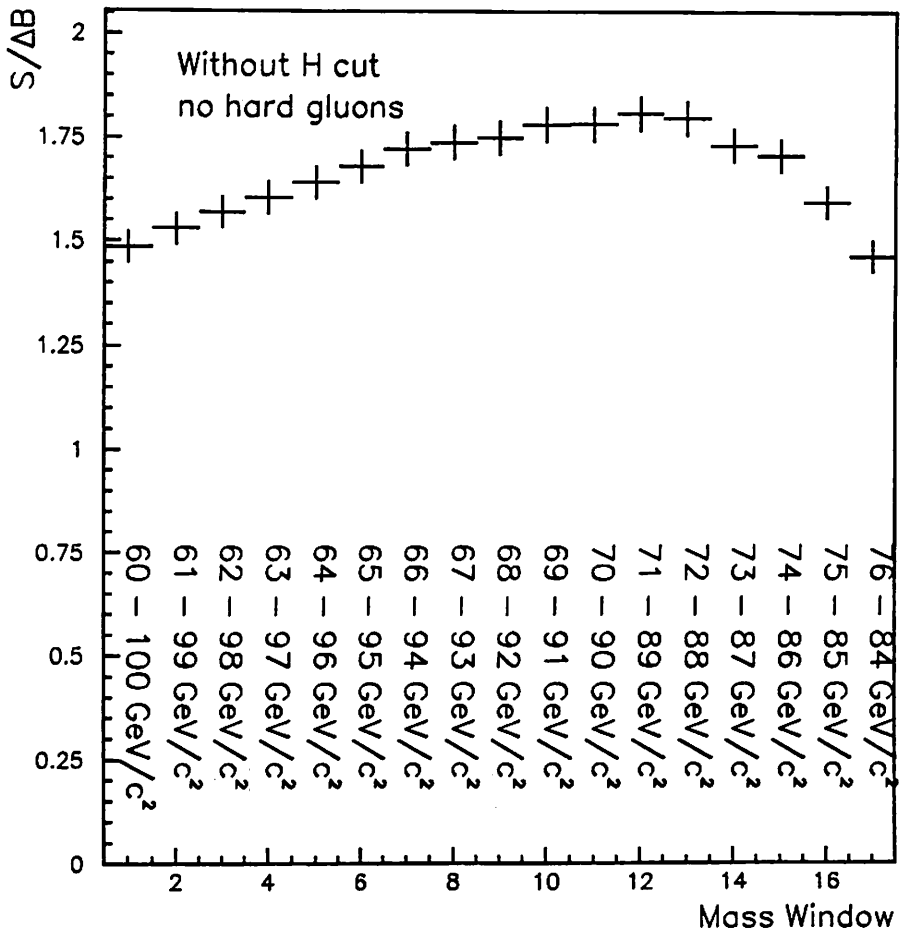

Figure 5.4: The average of significance versus mass window obtained in 1000 Monte Carlo pseudo experiments where all events have $W \rightarrow$jj signal which means there is no hard gluon effects. The background fraction was set to 68%.

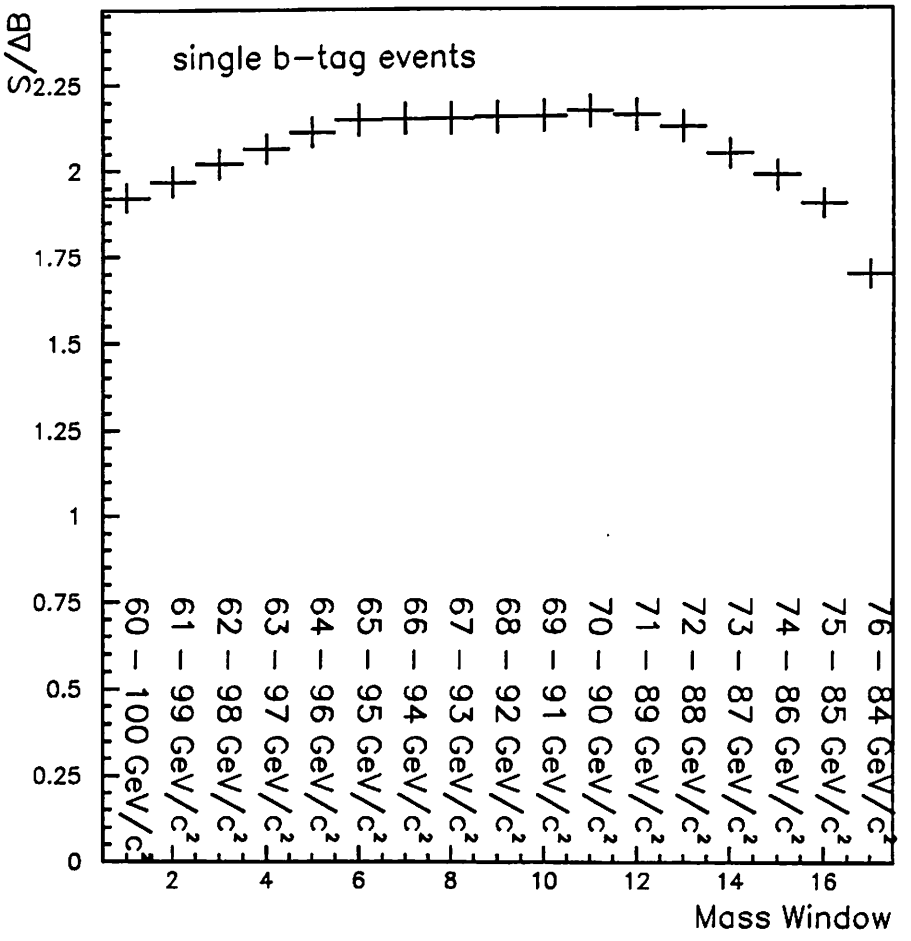

Figure 5.5: The average of significance versus mass window obtained in 1000 Monte Carlo pseudo experiments. All events are single b-tagged events. The background fraction was set to 19%.

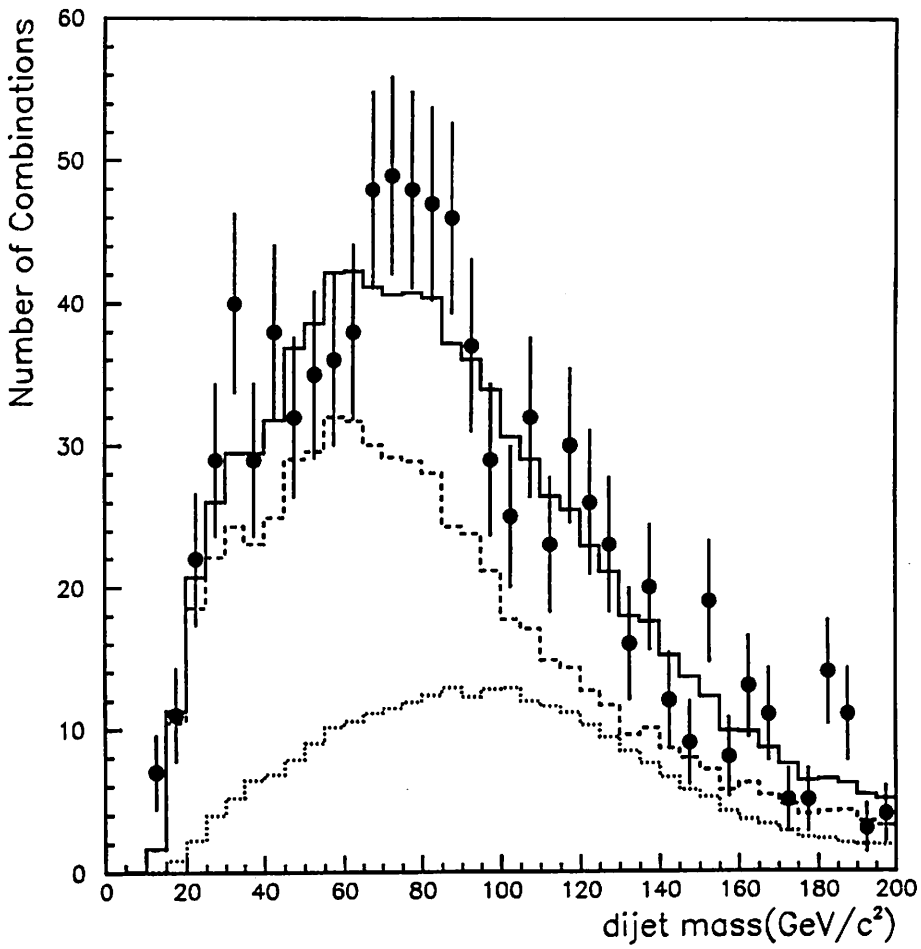

Figure 5.6: The dijet mass distribution for pretagged events(black points) was fitted with a sum of that of VECBOS W+jets background(broken line) and that of HERWIG combinatorial background(dotted line). We excluded the W mass region for fitting. The mean and sigma of Gaussian probability function are 79.7±3.6 GeV/c^2 and 6.9±2.1 GeV/c^2, respectively

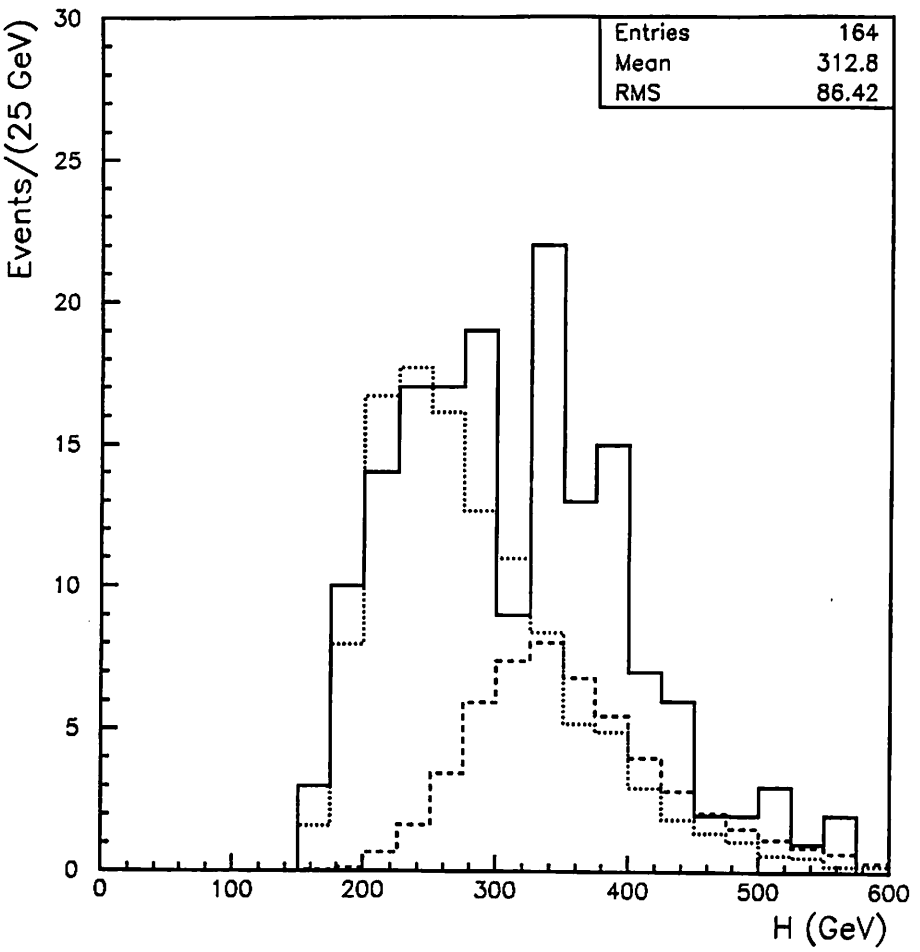

Figure 5.7: Solid line shows H distribution for pretagged events. Dotted histogram shows the H distribution of W+jets background. Dashed histogram shows that of $t\bar{t}$ events.

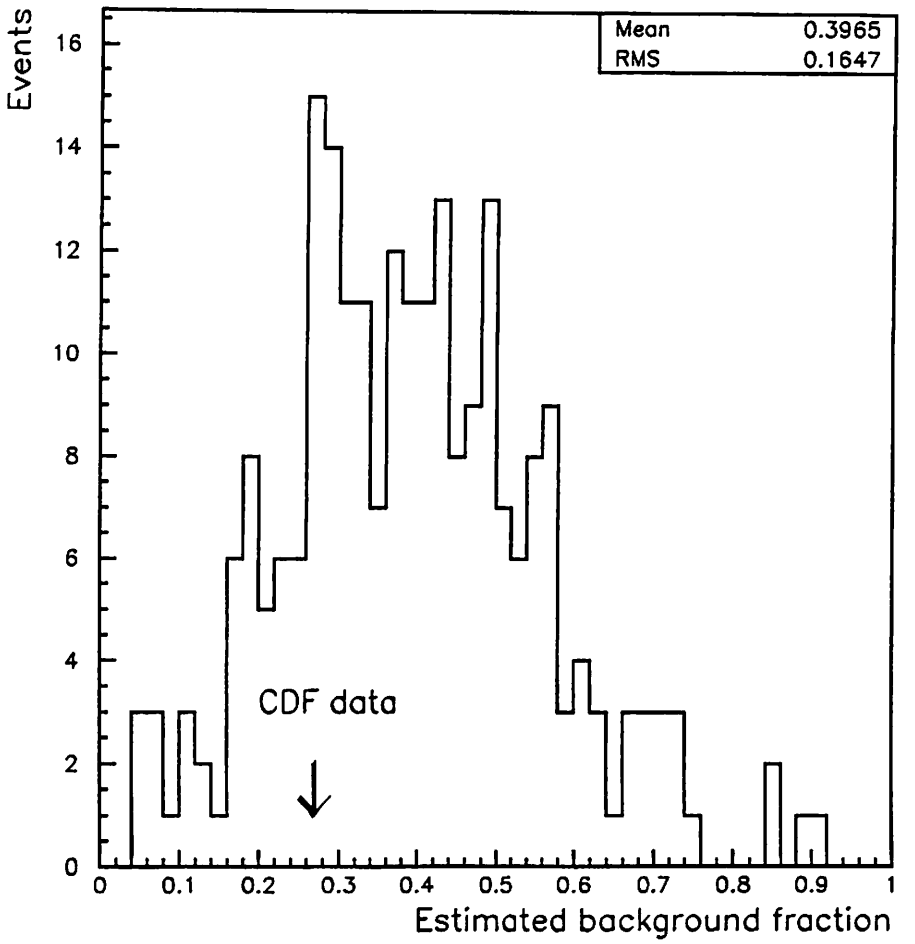

Figure 5.8: The plot of estimated background fraction with H>310 GeV cut on Monte Carlo pseudo experiments.

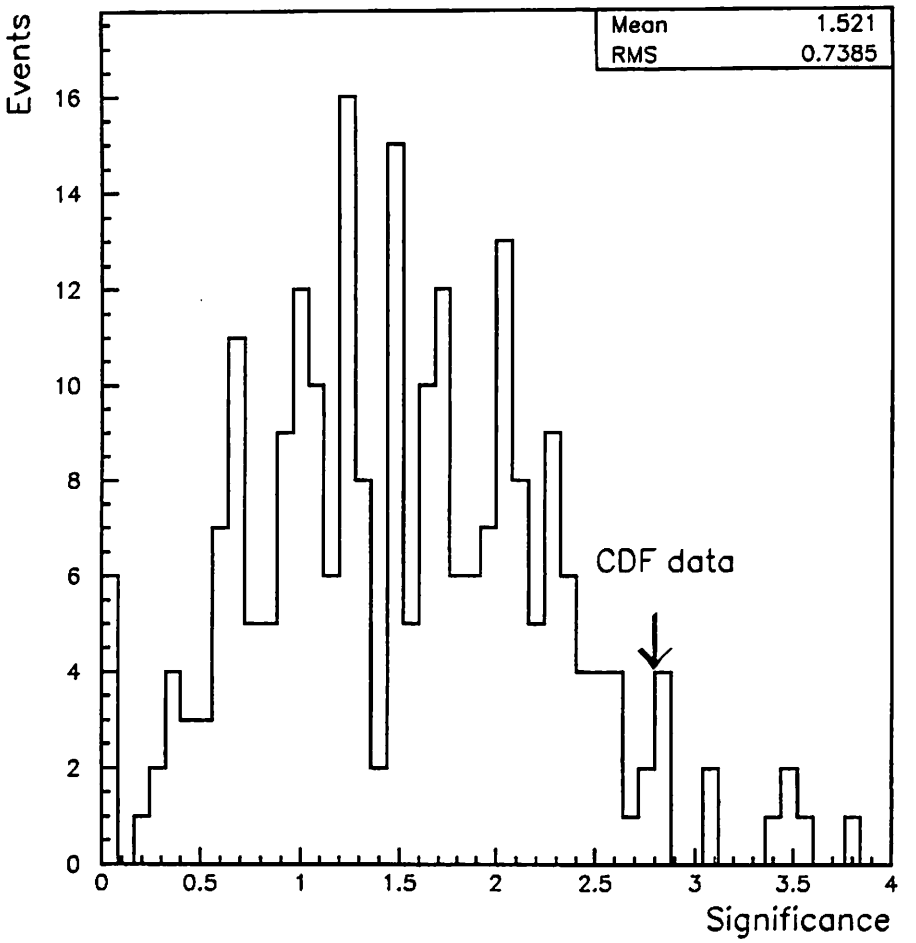

Figure 5.9: The plot of significance with H>310 GeV cut on Monte Carlo pseudo experiments.

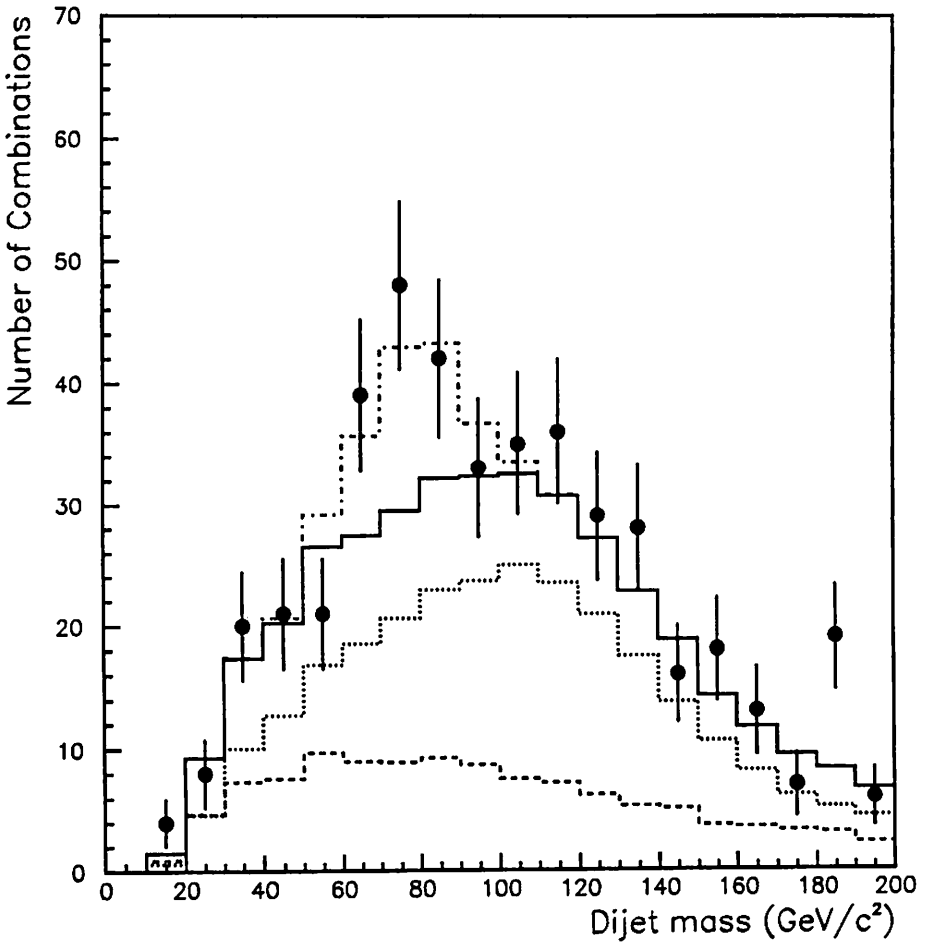

Figure 5.10: Fitting result after H>310 GeV cut. With $Q^2=\langle P_T\rangle^2$ VECBOS background shape. The fit of the signal excess to a Gaussian with a fixed σ of 11.7 GeV/c^2 gives a mean of 77.1±3.8 GeV/c^2.

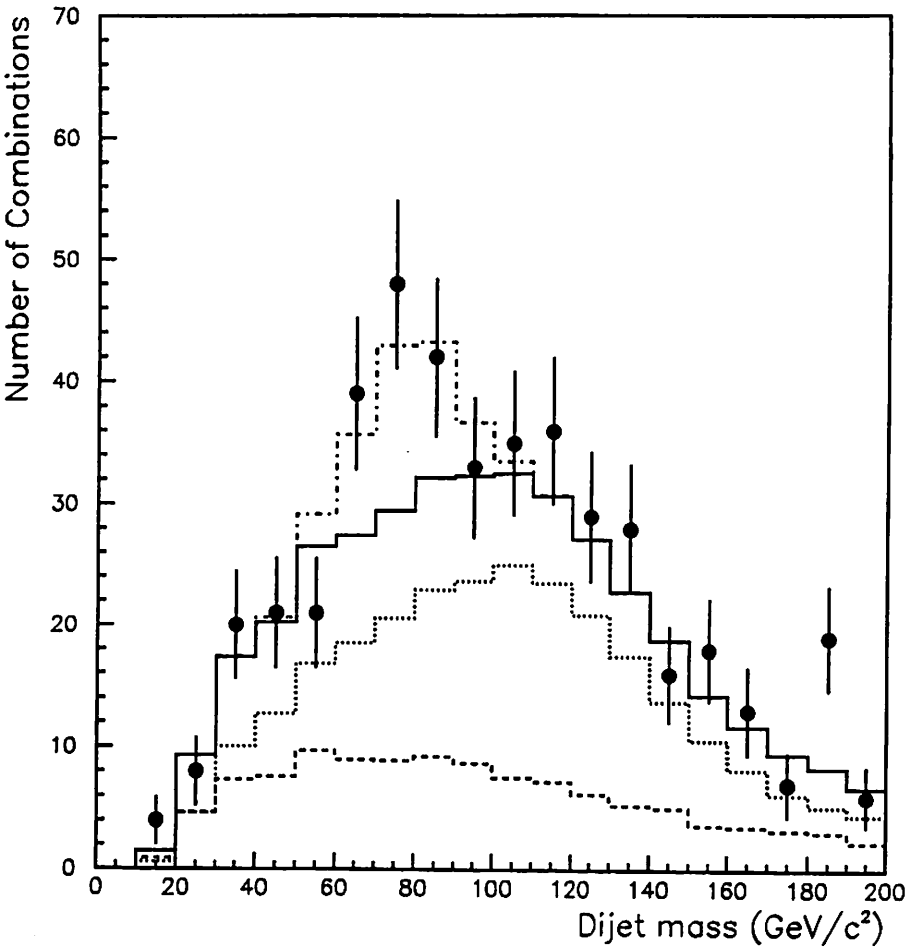

Figure 5.11: Fitting result after H>310 GeV cut with $Q^2=Mw^2$ VECBOS background shape. The fit of the signal excess to a Gaussian with a fixed σ of 11.7 GeV/c^2 gives a mean of 77.0±3.7 GeV/c^2.

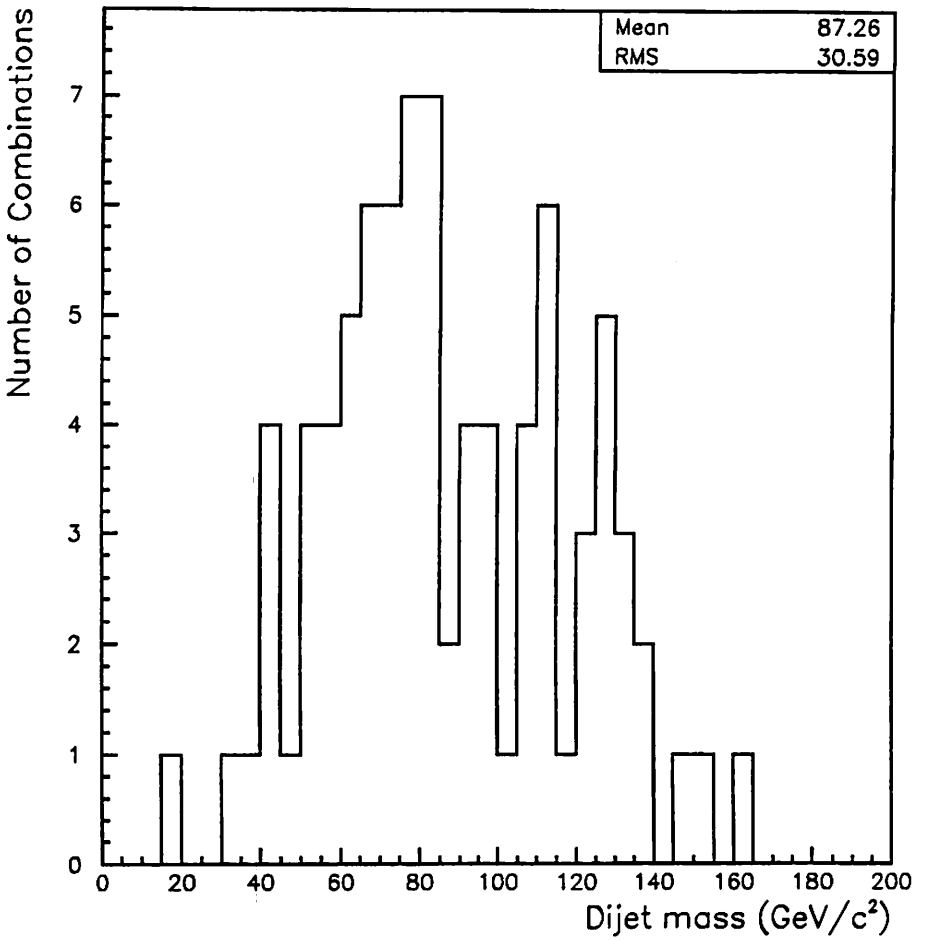

Figure 5.12: The dijet mass distribution for single b-tagged events.

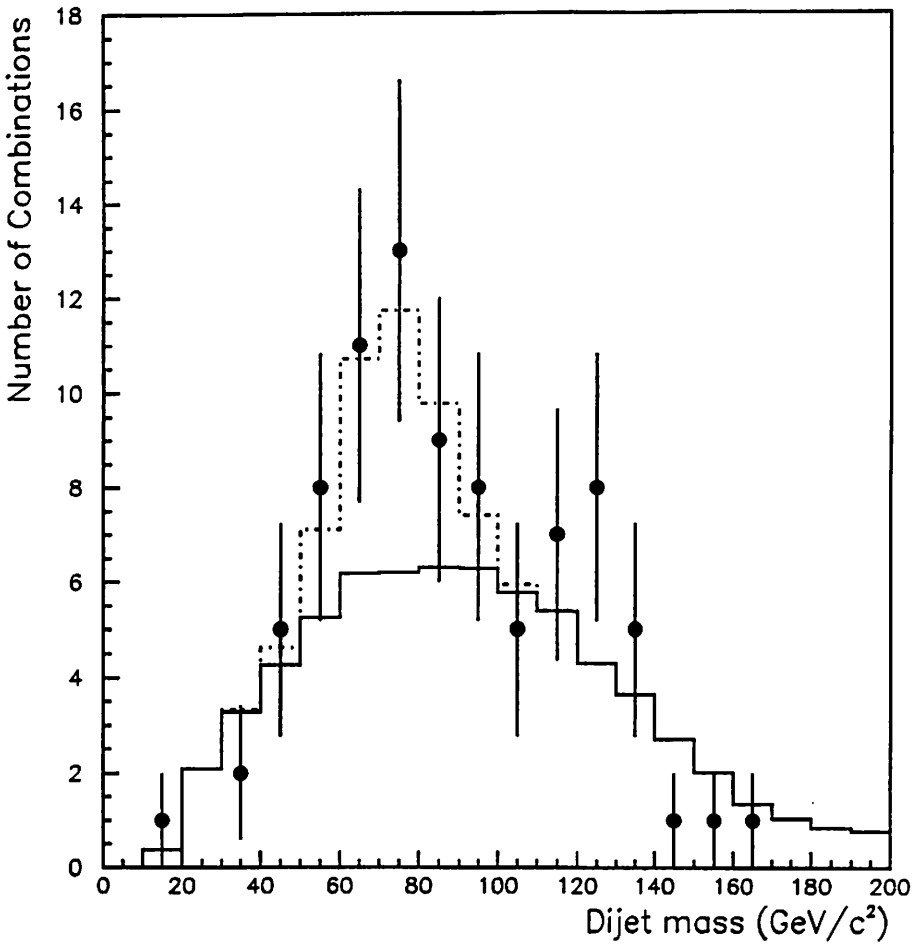

Figure 5.13: Fitting result on single b-tagged events with $Q^2=\langle P_T\rangle^2$ VECBOS background shape.

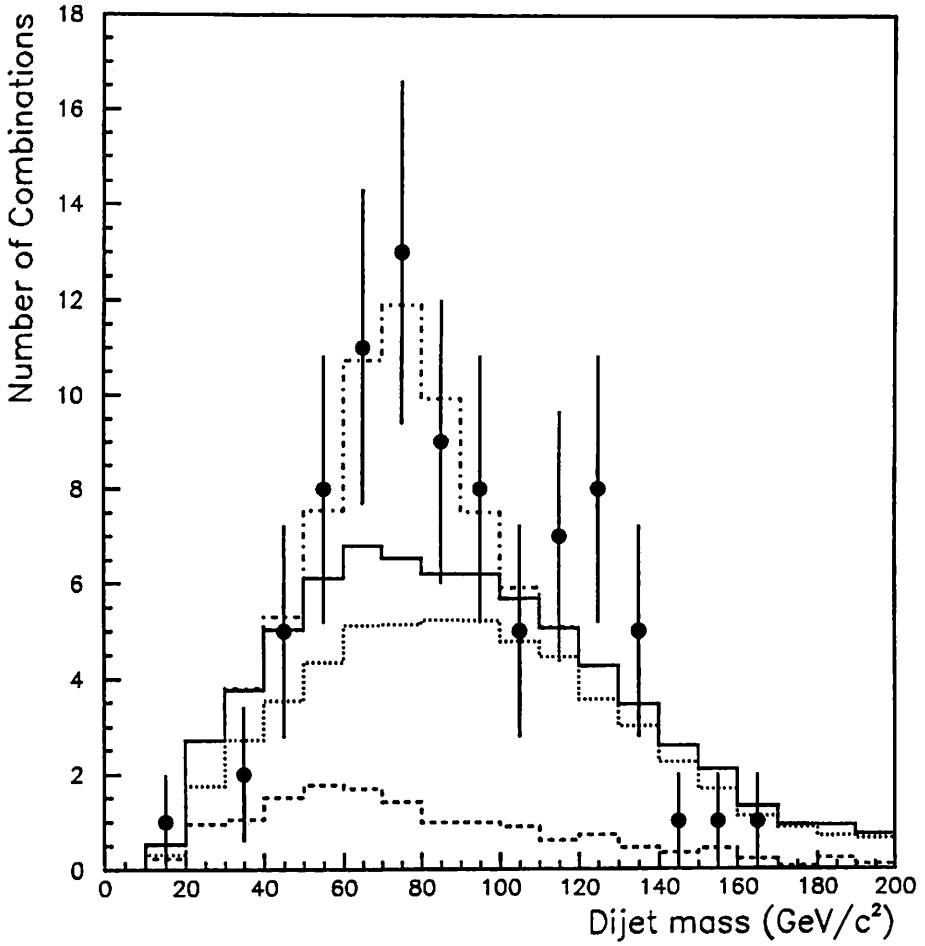

Figure 5.14: Fitting result on single b-tagged events with $Q^2=\langle P_T\rangle^2$ VECBOS background shape. The background shape was constrained to be 0.19±0.06.

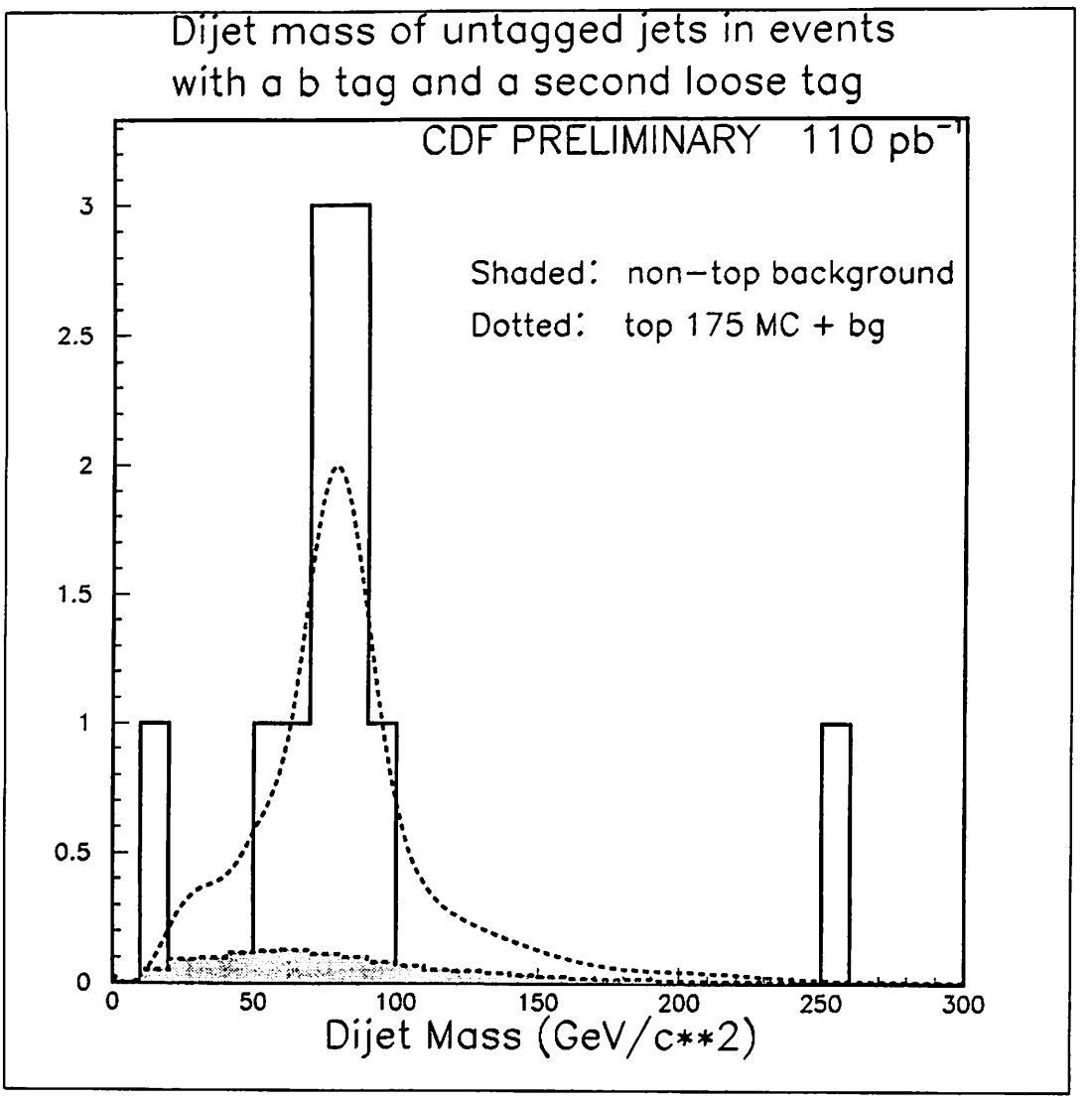

Figure 5.15: The dijet mass distribution of 11 double b-tagged events with expected signal+background shape(dotted) and background shape(shaded).

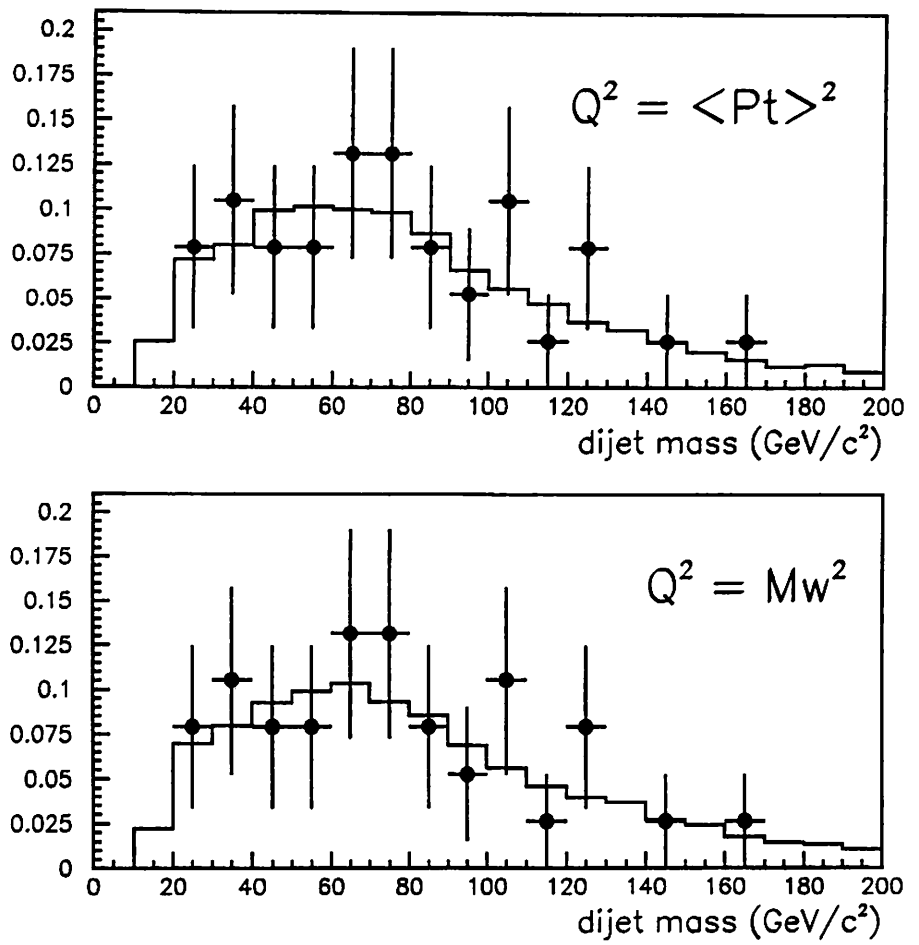

Figure 5.16: A comparison of dijet mass distribution between Z+4jet CDF real data and VECBOS W+3jets Monte Carlo. They are consistent each other within statistical significance.

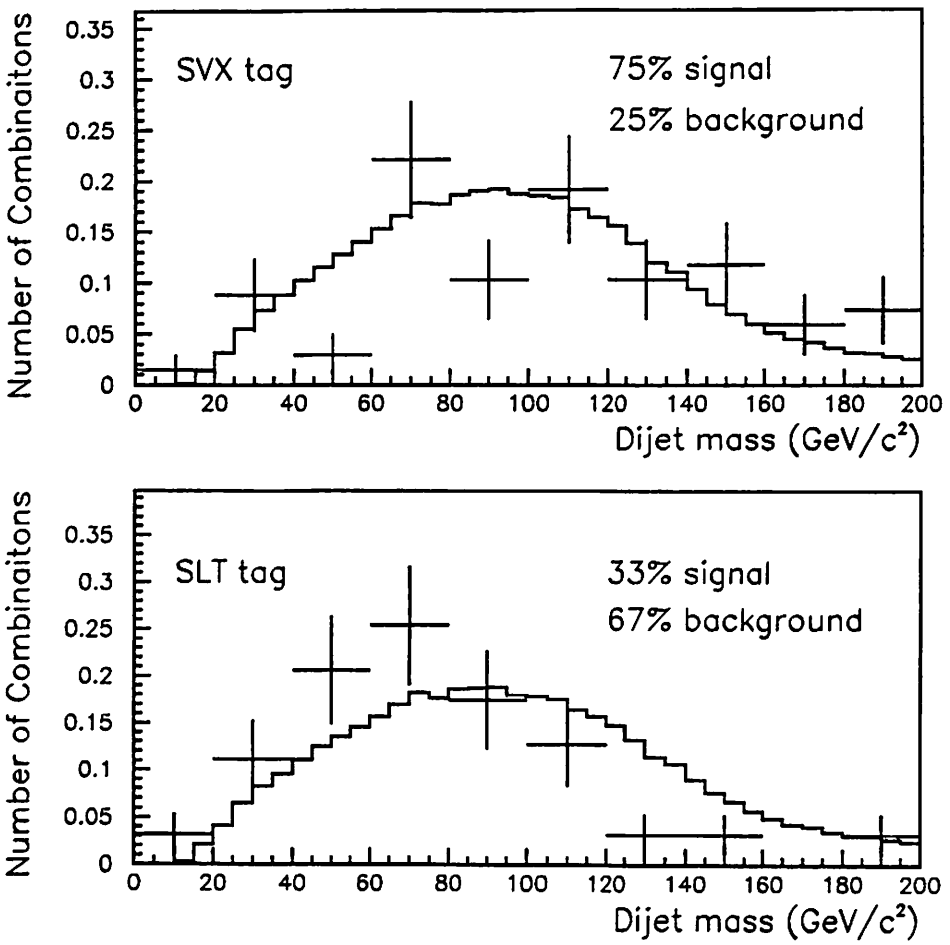

Figure 5.17: A comparison of combinatorial background shape between SVX(SLT) b-tagged events and Monte Carlo events.

Chapter 6

Fraction of Events with a Gluon Jet

6.1 Motivation

In the CDF top quark mass analysis, the hard gluon fraction uncertainty is a large source of the systematic error in the top quark mass measurement at CDF[11]. Where the hard gluon jet is a jet which is

1. among the four leading jets of the event, and
2. more than ΔR[1]=0.4 away from the nearest parton from $t\bar{t}$ decay.

Then a "hard gluon fraction" is the fraction of events with at least one hard gluon jet. We tried to estimate the hard gluon fraction using the dijet mass distribution of double b-tagged $W+\geq$4jet events. We use the double b-tagged

[1] $R=\sqrt{\eta^2+\phi^2}$

$W+\geq$4jet event sample where dijet mass peak was proved to be consistent with a W mass peak[22].

In section 2, we will compare the hard gluon fraction in HERWIG $t\bar{t}$ Monte Carlo data with that in PYTHIA. In section 3, we will show the fitting results of dijet mass distribution to Monte Carlo templates with one parameter of the hard gluon fraction. In section 4, we will show the fitting results with two parameters of the hard gluon fraction and the jet energy scale. In the last section, we summarize the analysis results.

6.2 Hard gluons in Monte Carlo $t\bar{t}$ events

6.2.1 HERWIG Monte Carlo

The P_T distribution is shown in Fig. 6.1 for gluon jets in four and six leading jets in $W+\geq$4jet events from HERWIG $t\bar{t}$ Monte Carlo data with M_{top} of 175 GeV/c^2. The hard gluon fractions in the pretagged $W+\geq$4jet event sample were 53$\pm$1% and 52$\pm$1% before and after $\chi^2 \leq 10$ cut, respectively. The hard gluon fractions in one b-tagged sample were 51$\pm$1% and 46$\pm$1% before and after $\chi^2 \leq 10$ cut, respectively. The hard gluon fractions in double b-tagged sample were 49$\pm$1% and 33$\pm$1% before and after $\chi^2 \leq 10$ cut and dijet mass cut (60GeV/c^2 < M_{jj} < 100GeV/c^2), respectively. Thus the hard gluon fractions are about 50% in any samples before the cut.

6.2.2 PYTHIA Monte Carlo

The P_T distribution is shown in Fig. 6.2 for gluon jets in four and six leading jets in $W+\geq$4jet events from PYTHIA $t\bar{t}$ Monte Carlo data with M_{top} of 175 GeV/c^2. The hard gluon fractions in the pretagged $W+\geq$4jet sample were 61$\pm$1% and 59$\pm$1% before and after $\chi^2 \leq 10$ cut, respectively. The hard gluon fractions in one b-tagged sample were 60$\pm$1% and 56$\pm$1% before and after $\chi^2 \leq 10$ cut, respectively. The hard gluon fractions in double b-tagged sample were 56$\pm$1% and 45$\pm$1% before and after $\chi^2 \leq 10$ cut and dijet mass cut (60GeV/c^2 < M_{jj} < 100GeV/c^2), respectively.

Comparing PYTHIA with HERWIG, the gluon P_T distribution is similar and the hard gluon fraction in PYTHIA is a little larger than in HERWIG by ~10%.

6.3 Dijet mass fitting with one parameter of hard gluon fraction

6.3.1 Templates of dijet mass distribution

We calculated an invariant mass of dijet which are not b-tagged in double b-tagged $W+\geq$4jet events made with HERWIG $t\bar{t}$ Monte Carlo at M_{top} of 175 GeV/c^2. The events were categorized into two samples with and without a hard gluon jet. Mixing these two samples we made dijet mass templates with various hard gluon fractions from 0% to 100% by a 5% step as shown in Fig. 6.3.

6.3.2 Dijet mass fitting

The dijet mass distribution is shown in Fig. 6.4 for the CDF double b-tagged $W+\geq$4jet events where we used 0.5 GeV/c^2 instead of a cluster mass as the jet mass. It was fitted to the sum of HERWIG $t\bar{t}$ template with a certain hard gluon fraction and the VECBOS W+3jets background template, where the number of backgrounds were constrained to 1.3 ± 0.4. We repeated this procedure for various hard gluon fractions from 0% to 100% by a 5% step, and obtained a plot of likelihood versus hard gluon fraction as shown in Fig. 6.5. By fitting this plots to a quadratic function, we obtained the hard gluon fraction of $2.6^{+36.3}_{-2.6}$ (statistical only)%.

Next we performed 1000 pseudo-experiments as follows: We made 1000 event samples. Each sample has 11 double b-tagged $W+\geq$4jet events with a hard gluon fraction of 50% using HERWIG $t\bar{t}$ Monte Carlo. Then we applied the above fitting procedure to the dijet mass distribution of each event sample to obtain the fitted hard gluon fraction. The distributions of the hard gluon fraction and its error are shown in Fig. 6.6. We define a "pull" by the deviation of the observed variable from the true one divided by its resolution. Figure 6.7 shows the pull distribution of the hard gluon fraction which should have a mean of 0 and a sigma of 1. The pull mean value is consistent with 0 and its sigma is consistent with 1.

We have also obtained the fitted hard gluon fraction for HERWIG double b-tagged $W+\geq$4jet events with various hard gluon fractions. The fitted hard gluon fraction is consistent with the input fraction as shown in Fig. 6.8.

6.3.3 Systematic uncertainty in hard gluon fraction

Jet energy scale

The uncertainty in absolute jet energy scale due to the detector effects is given by "Behrends curve"[24]. This curve was parameterized using a polynomial function as shown in Fig. 6.9 and applied to raw jets. The uncertainties in detector stability and underlying events are also applied. The magnitude of these uncertainties are 2% and 0.1 GeV, respectively. We made 1000 samples in both positive and negative shifts and performed "pseudo experiments" with normal templates. From the means of these distributions, we estimated the uncertainty in hard gluon fraction to be $\pm 4.2\%$.

The energy scale uncertainty due to soft gluon effects is given in Reference [25], where authors parameterized the fractional energy difference between data and Monte Carlo as a function of jet P_T. The E_T of jet was shifted with this parameterized function in positive and negative directions. We performed "pseudo experiments" with normal templates and looked at the shift of fitted hard gluon fraction. This uncertainty depends on that of jet-parton assignment. So we can expect smaller uncertainty for double b-tagged events. Assigning the correct jet combination, the jet energy correction for $t\bar{t}$ events will work correctly and it will make the jet E_T closer to its true value. We also performed "pseudo experiments" in the same method with positive and negative shifted samples, and found that the positive and negative shifts yield $+6.3\%$ and $+5.3\%$ shifts from the expected hard gluon fraction, respectively. We take this uncertainty of $+6.3\%$. The shift due to an error of ± 1GeV for the jet energy beyond a radius of 1.0 has been esti-

mated using the same method. We estimated the uncertainty to be +1.0% and +3.2%. We take this uncertainty of +3.2%.

From these estimations, we evaluated the systematic uncertainty due to the uncertainty in jet energy scale as $^{+8.2}_{-4.2}$ %.

Jet energy resolution

We evaluated the hard gluon fraction uncertainty due to the uncertainty in the jet energy resolution which is 10% [23]. We made a fitting with templates where the jet energy resolution was shifted by ±10%. The shifts of hard gluon fraction were +3.1% and +6.1% for positive and negative shifts, respectively. From this result, we take the uncertainty of +6.1%.

Likelihood method

We evaluated the hard gluon fraction uncertainty due to the different conditions in likelihood fits. The conditions are background unconstrained, background constrained to 1.3±0.4 and background fixed to 1.3. The fitting results are tabulated in Table 6.1. From the variation in this result, the uncertainty is ±1.3%.

fit condition	estimated hard gluon fraction
1.3±0.4	$2.6\ ^{+36.3}_{-2.6}$ %
1.3(fix)	$2.8\ ^{+36.1}_{-2.8}$ %
no constraint	$0.0\ ^{+37.8}_{-0.0}$ %

Table 6.1: Estimated hard gluon fractions for 3 kinds of fit conditions.

Fitting method

In a likelihood fitting, if we have Monte Carlo templates at 1% intervals, this would not be a problem. But templates are limited. So we have to look at what will happen when we varied the fit regions. From the variation in fitted hard gluon fraction, we estimated the uncertainty to be ±1.3%.

fit condition	estimated hard gluon fraction
5 points fit	$3.1\ ^{+28.5}_{-3.1}\%$
7 points fit	$0.0\ ^{+43.3}_{-0.0}\%$
9 points fit	$2.6\ ^{+36.3}_{-2.6}\%$
11 points fit	$0.9\ ^{+38.1}_{-0.9}\%$
13 points fit	$0.0\ ^{+38.4}_{-0.0}\%$

Table 6.2: Estimated hard gluon fractions for various fit method.

Monte Carlo statistics

The uncertainty in Monte Carlo statistics appears in the likelihood fitting. The error of each -Log(likelihood) was calculated from the statistical error of signal and background templates. In order to estimate the uncertainty, we fluctuate the distribution of templates by its statistical error. We repeat fitting the CDF data with the templates fluctuated statistically 1000 times. Figure 6.10 shows the distribution of fitted hard gluon fraction. From the r.m.s. of fitted hard gluon fraction distribution, we estimated the uncertainty to be ±7.6%.

Total systematic uncertainty

The systematic uncertainties described above are summarized in Table 6.3. Total systematic uncertainty is $^{+12.9}_{-8.9}$%. Thus the hard gluon fraction is obtained to be $3^{+36}_{-3}(\text{stat})^{+13}_{-3}(\text{syst})$ %.

systematic uncertainties	values(%)
Jet energy Scale	$^{+8.2}_{-4.2}$%
Jet energy Resolution	+6.1 %
Likelihood Method	±1.3 %
Fitting Method	±1.3 %
Monte Carlo statistics	±7.6 %
total	$^{+12.9}_{-8.9}$%

Table 6.3: Systematic uncertainties in hard gluon fraction.

6.4 Dijet mass fitting with two parameters of hard gluon fraction and jet energy scale

6.4.1 Dijet mass fitting

In this section, we tried the two parameter fitting of the dijet mass distribution for the CDF double b-tagged $W+\geq$4jet events. The two parameters are the hard gluon fraction and the jet energy scale. In the same way as the one parameter fitting of hard gluon fraction described in the preceding section, the dijet mass distribution was fitted to the sum of the HERWIG

$t\bar{t}$ template with a certain hard gluon fraction and a certain jet energy scale and the VECBOS W+3jets background template, where the number of backgrounds were constrained to 1.3 ± 0.4. We repeated this procedure for various hard gluon fractions from 0% to 100% by a 5% step and various jet energy scale shift of $\pm$10%, $\pm$5%, $\pm$2% and 0%, and obtained a likelihood as a function of hard gluon fraction and jet energy scale as shown in Fig. 6.11. By fitting this distribution to a quadratic function, we obtained the hard gluon fraction of $9.1^{+44.9}_{-9.1}$ (statistical only) % and jet energy scale shift of -2.8 ± 8.0 (statistical only)%.

Next we did 1000 pseudo-experiments as follows: We made 1000 event samples. Each sample has 11 double b-tagged $W+\geq$4jet events with a hard gluon fraction of 50% using HERWIG $t\bar{t}$ Monte Carlo. Then we applied the above fitting procedure to the dijet mass distribution of each event sample to obtain the fitted hard gluon fraction and the fitted jet energy scale. The distributions of the hard gluon fraction and its error are shown in Fig. 6.12 and the pull distributions of the hard gluon fraction are shown in Fig. 6.13. The pull mean value is consistent with 0 but its r.m.s. is a little smaller than 1. So the statistical error of hard gluon fraction is overestimated. The distributions of the jet energy scale and its error are shown in Fig. 6.14 and the pull distribution of the energy scale is shown in Fig. 6.15. The pull mean value is consistent with 0 and its r.m.s. is consistent with 1.

6.4.2 Systematic uncertainty

The systematic uncertainties due to jet energy resolution, likelihood method, fitting method and Monte Carlo statistics were obtained in the same way as described in the preceding section. In order to estimate the uncertainty due to Monte Carlo statistics, we fluctuate the distribution of templates by its statistical error. Figure 6.16 shows the distributions of fitted hard gluon fraction and jet energy scale. From these distributions, we estimated the uncertainties in hard gluon fraction and jet energy scale to be ±4.9% and ±1.0%, respectively. They are summarized in Table 6.4. Total systematic uncertainty of the hard gluon fraction in $^{+6.7}_{-6.6}$%

systematic uncertainties	hard gluon fraction(%)	energy scale(%)
Energy Resolution	+1.2 %	$^{+0.2}_{-0.3}$ %
Likelihood Method	±4.4 %	±0.0 %
Fitting Method	±0.4 %	±0.1 %
Monte Carlo statistics	±4.9 %	±1.0 %
total	$^{+6.7}_{-6.6}$%	±1.0%

Table 6.4: Systematic uncertainties in hard gluon fraction.

Total systematic uncertainty of the jet energy scale is ±1.0%. Thus the hard gluon fraction and the jet energy scale shift are obtained to be 9^{+45}_{-9}(stat)±7(syst) % and −2.8±8.0(stat)±1.0(syst) %, respectively.

6.5 Summary

We estimated the hard gluon fraction in $W+\geq$4jet events by fitting the dijet mass distribution for the double b-tagged event sample to templates with various hard gluon fractions. As a result, we obtained the hard gluon fraction of 3^{+38}_{-3}(stat+syst) % in the double b-tagged $W+\geq$4jet events. The hard gluon fractions in HERWIG $t\bar{t}$ $W+\geq$4jet sample are about 50% in any samples: without b-tagging, one b-tagged or double b-tagged samples.

We also made the two parameter fitting of the dijet mass distribution for the double b-tagged event sample. The two parameters are the hard gluon fraction and the jet energy scale. As a result, we obtained the hard gluon fraction of 9^{+46}_{-9}(stat+syst) % and the jet energy scale shift of -2.8 ± 8.1%(stat+syst) in the double b-tagged $W+\geq$4jet events.

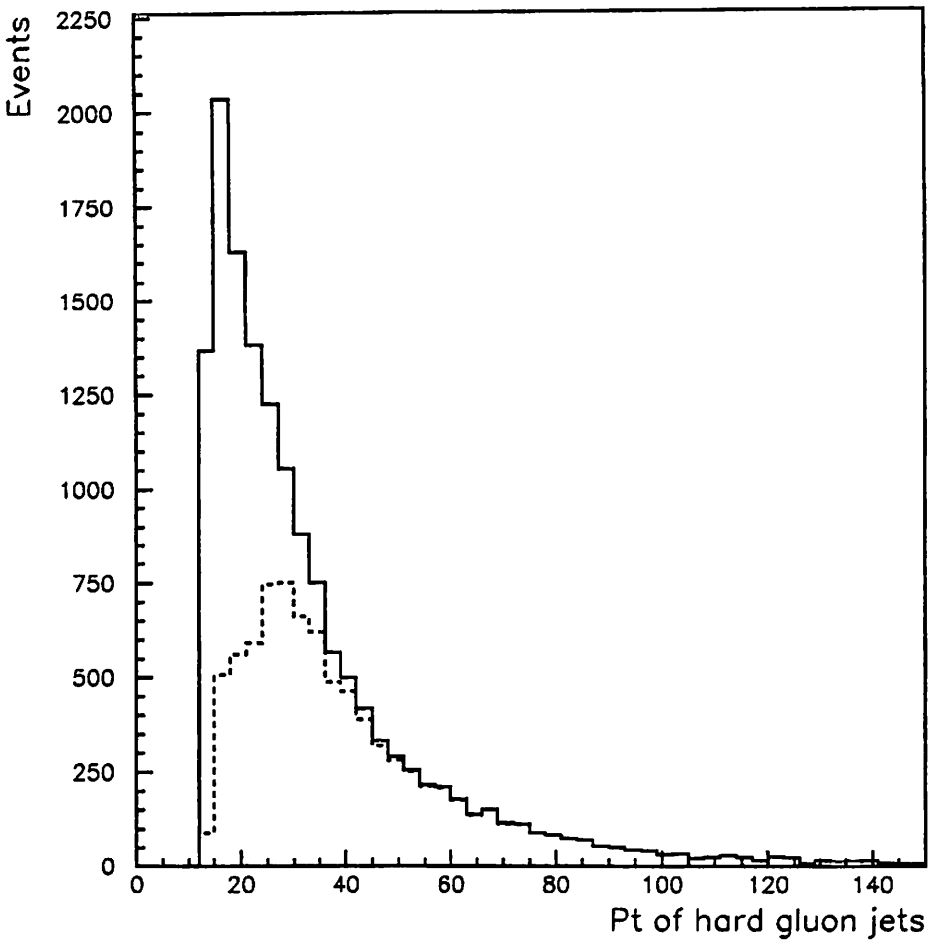

Figure 6.1: Transverse momentum distribution of hard gluon jets in HERWIG Monte Carlo. Solid histogram shows that in leading 6 jets, Dashed histogram shows that in leading 4 jets.

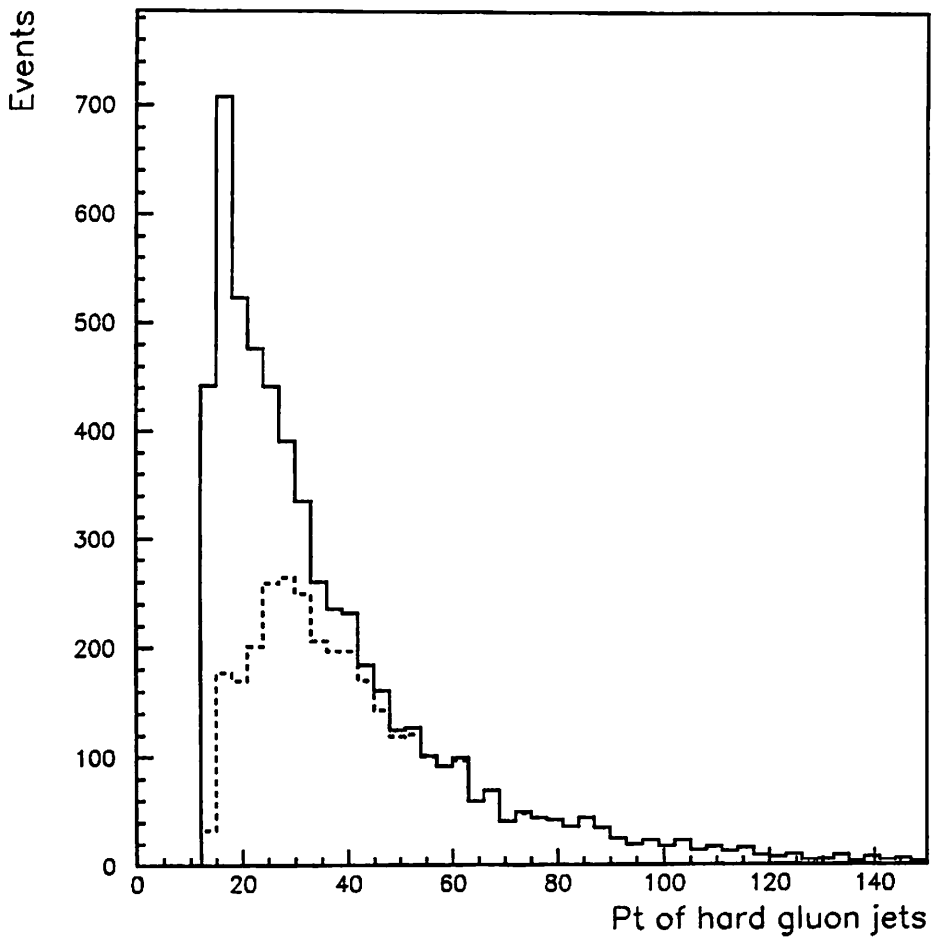

Figure 6.2: Transverse momentum distribution of hard gluon jets in PYTHIA Monte Carlo. Solid histogram shows that in leading 6 jets, Dashed histogram shows that in leading 4 jets.

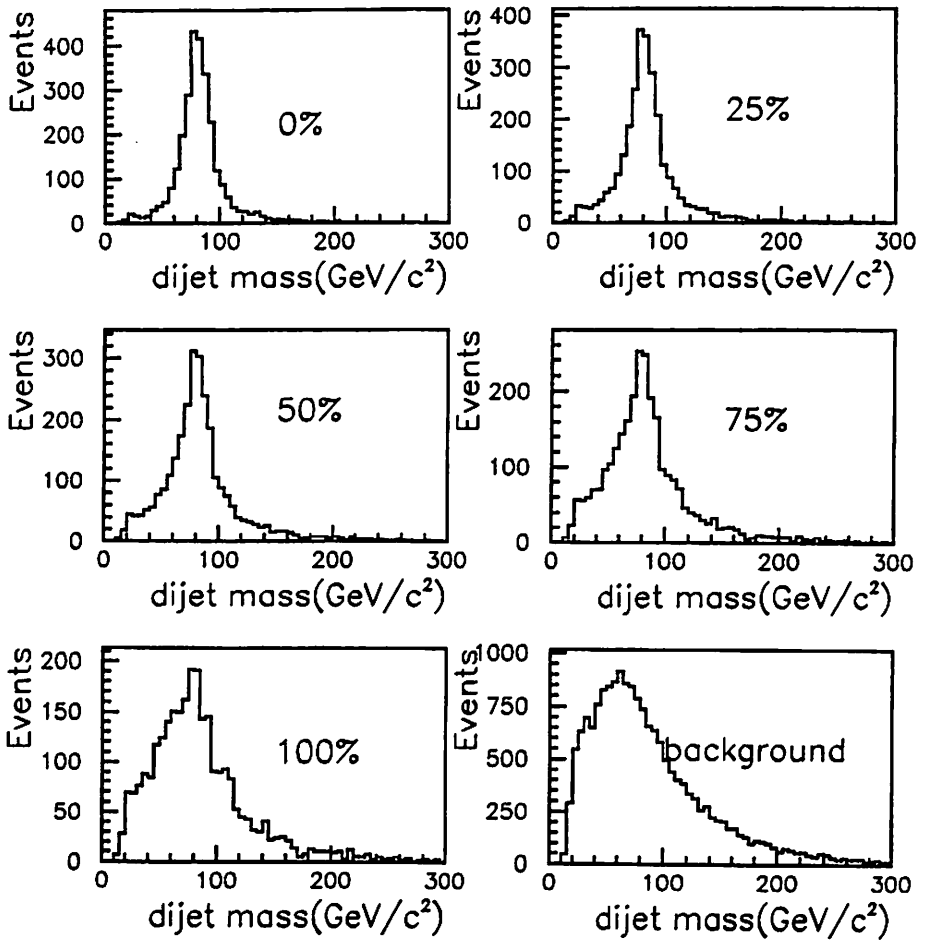

Figure 6.3: Dijet mass distributions for various hard gluon fractions. These histograms are used for a likelihood fitting as templates.

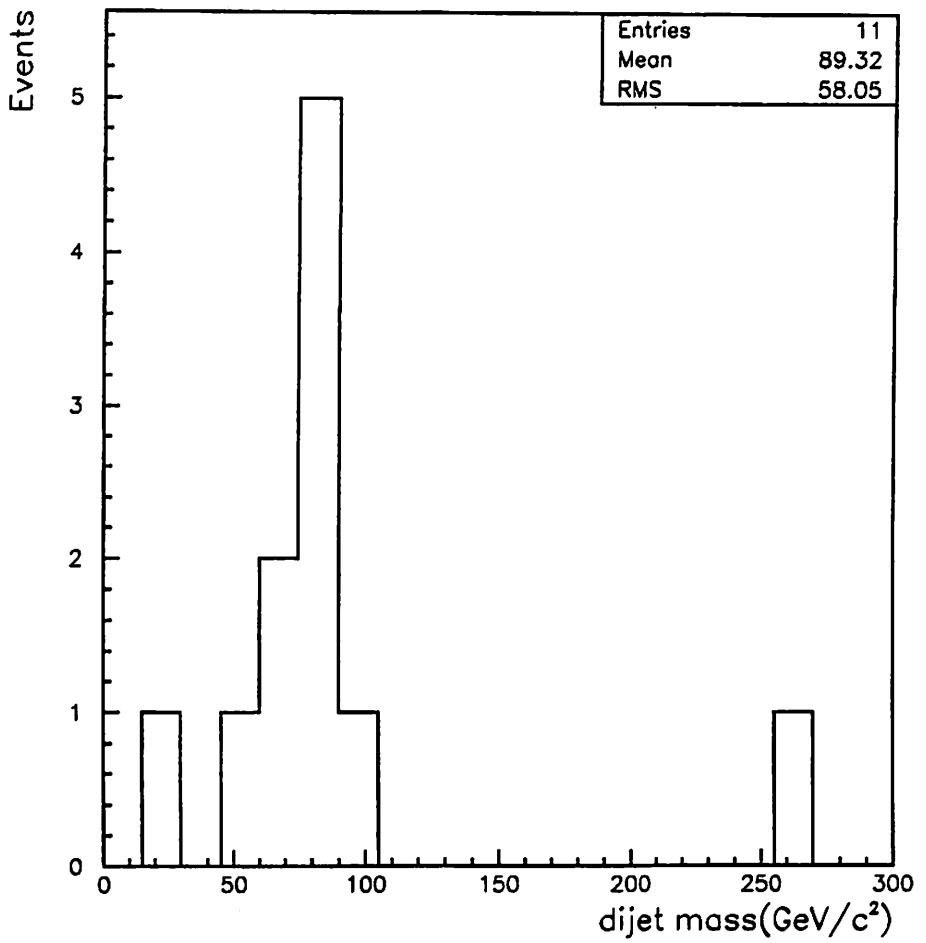

Figure 6.4: Dijet mass distributions of the CDF double b-tagged events.

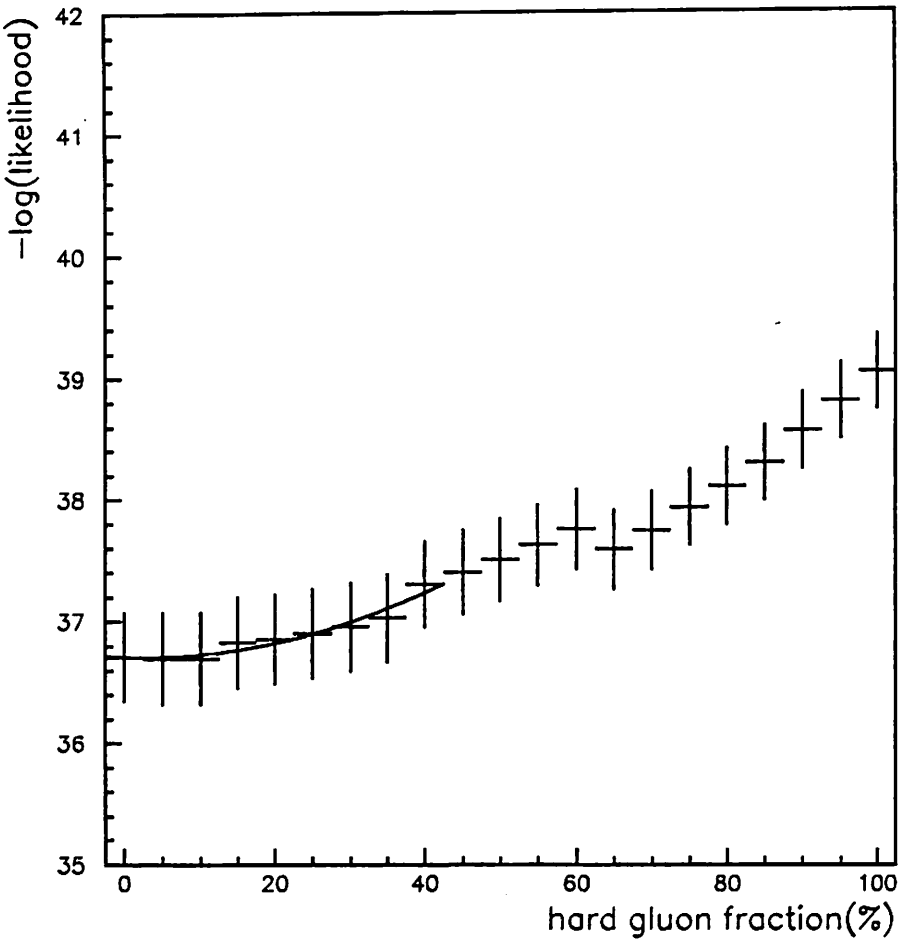

Figure 6.5: A plot of -log(likelihood) versus hard gluon fraction. This fit gives the hard gluon fraction on CDF data of $2.6^{+36.3}_{-2.6}$%.

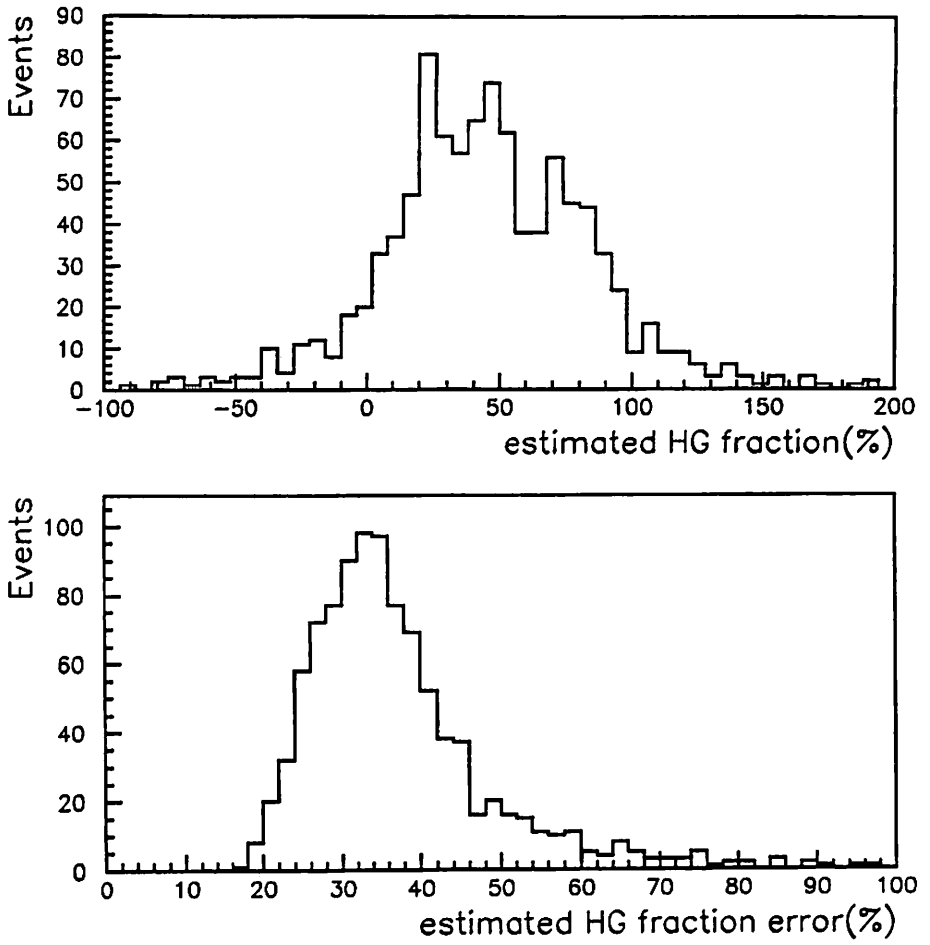

Figure 6.6: Top plot shows distribution of estimated hard gluon fraction on pseudo-experiments. Bottom plot shows distribution of its error.

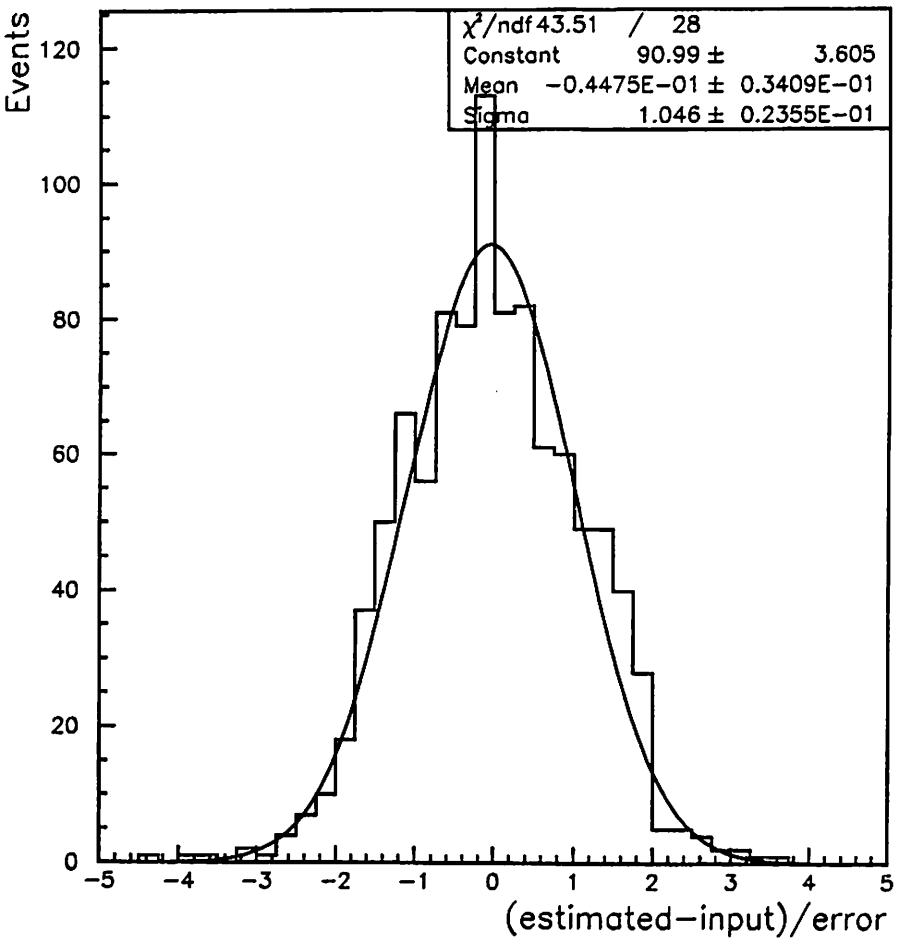

Figure 6.7: Pull distribution of pseudo-experiments. The mean value is consistent with 0 and sigma is consistent with 1.

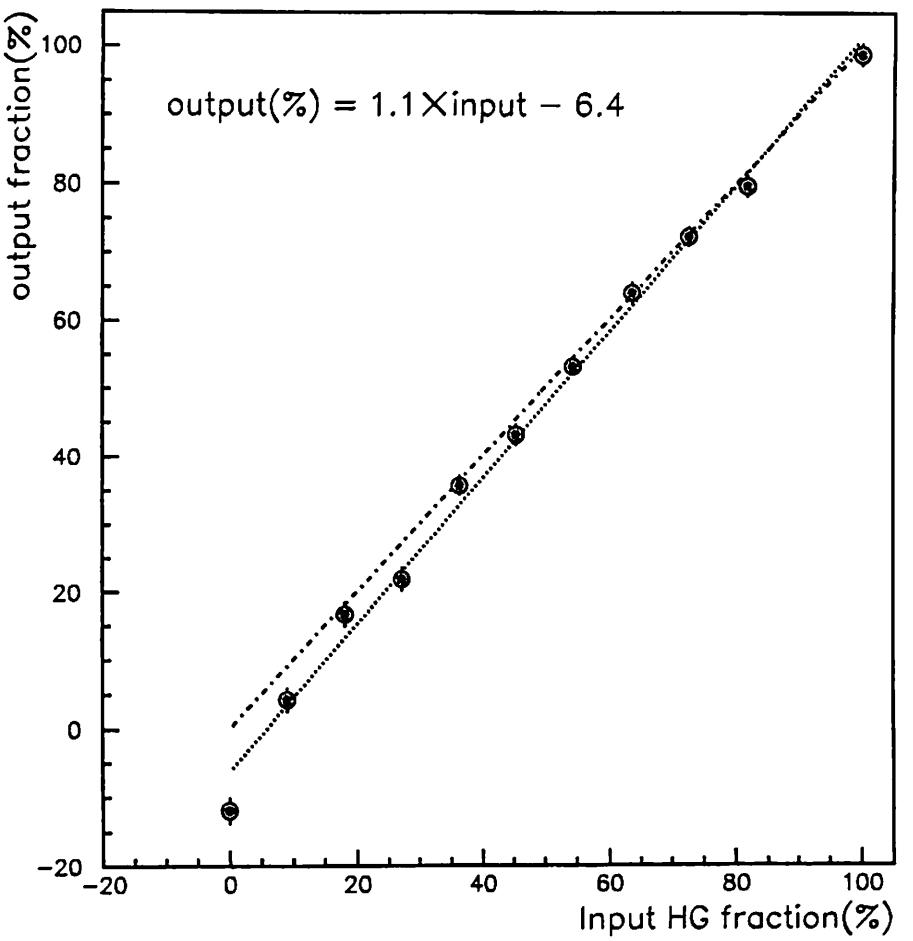

Figure 6.8: A plot of output fraction versus input fraction on pseudo experiments. Dashed line shows output = input and dotted line shows the best fit.

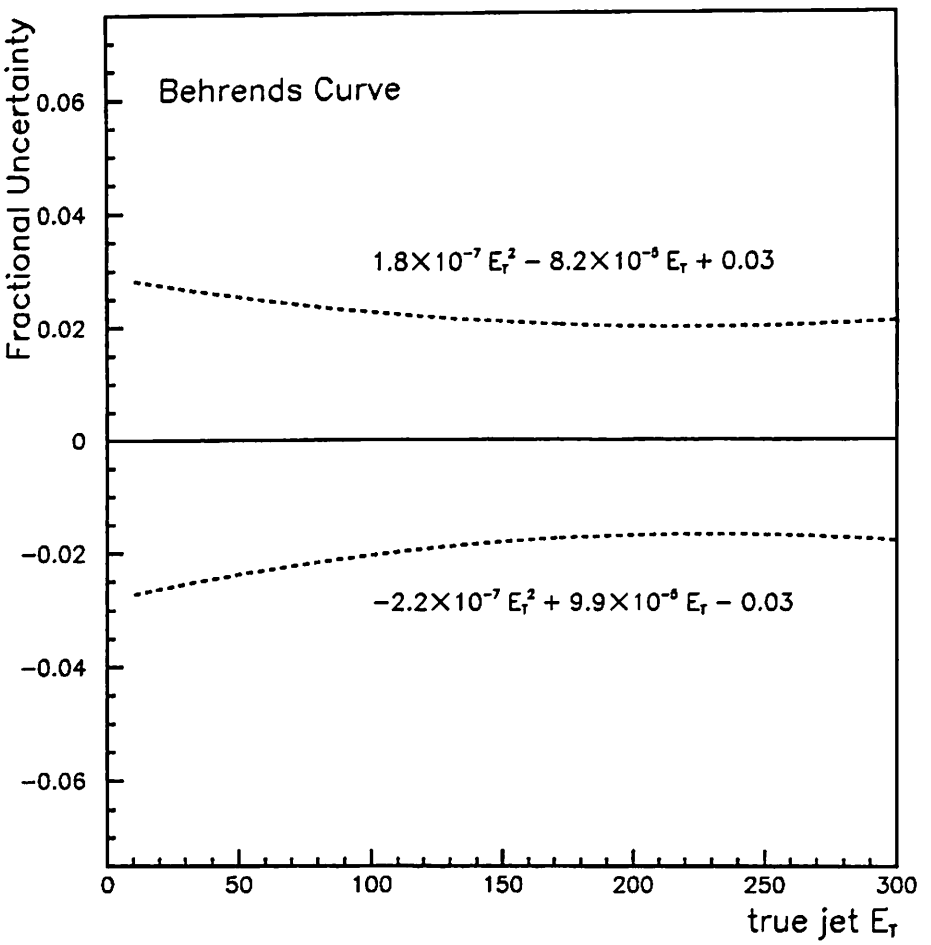

Figure 6.9: The systematic uncertainty on cone=0.4 jet energy scale estimated by Steve Behrends.

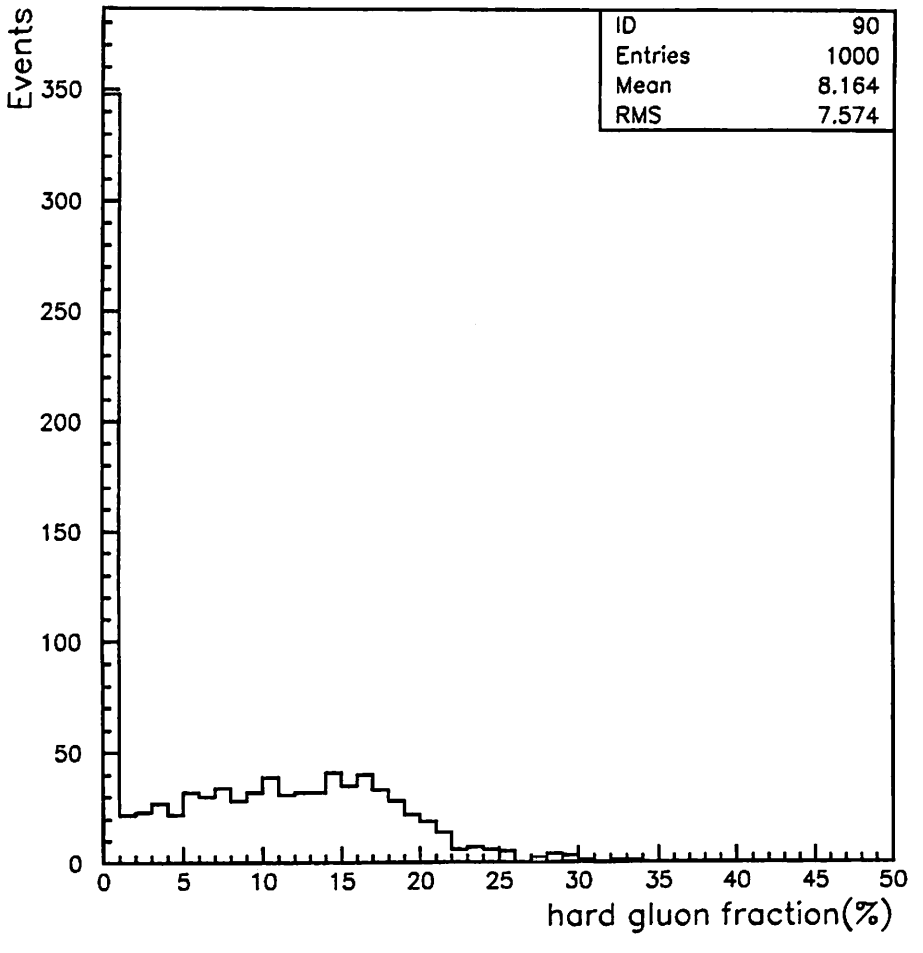

Figure 6.10: The distribution of estimated hard gluon fraction on 1000 pseudo experiments. In each experiments, templates were fluctuated by its statistical error.

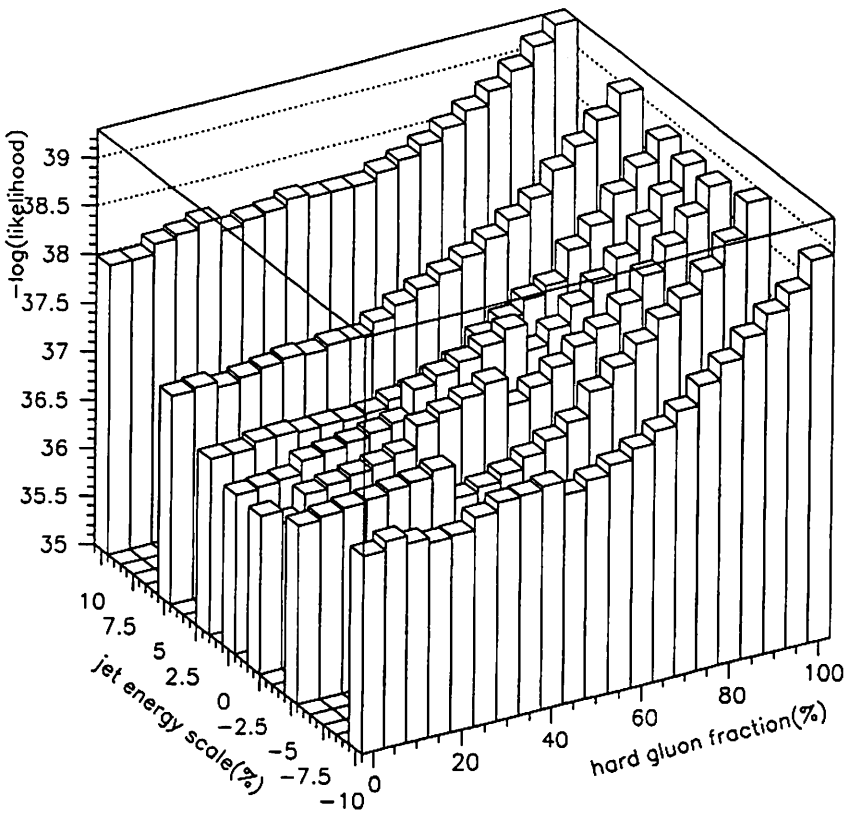

Figure 6.11: A plot of -log(likelihood) versus hard gluon fraction and the jet energy scale. This fit gives the hard gluon fraction of $9.1^{+44.9}_{-9.1}$% and the jet energy scale of -2.8 ± 8.0%.

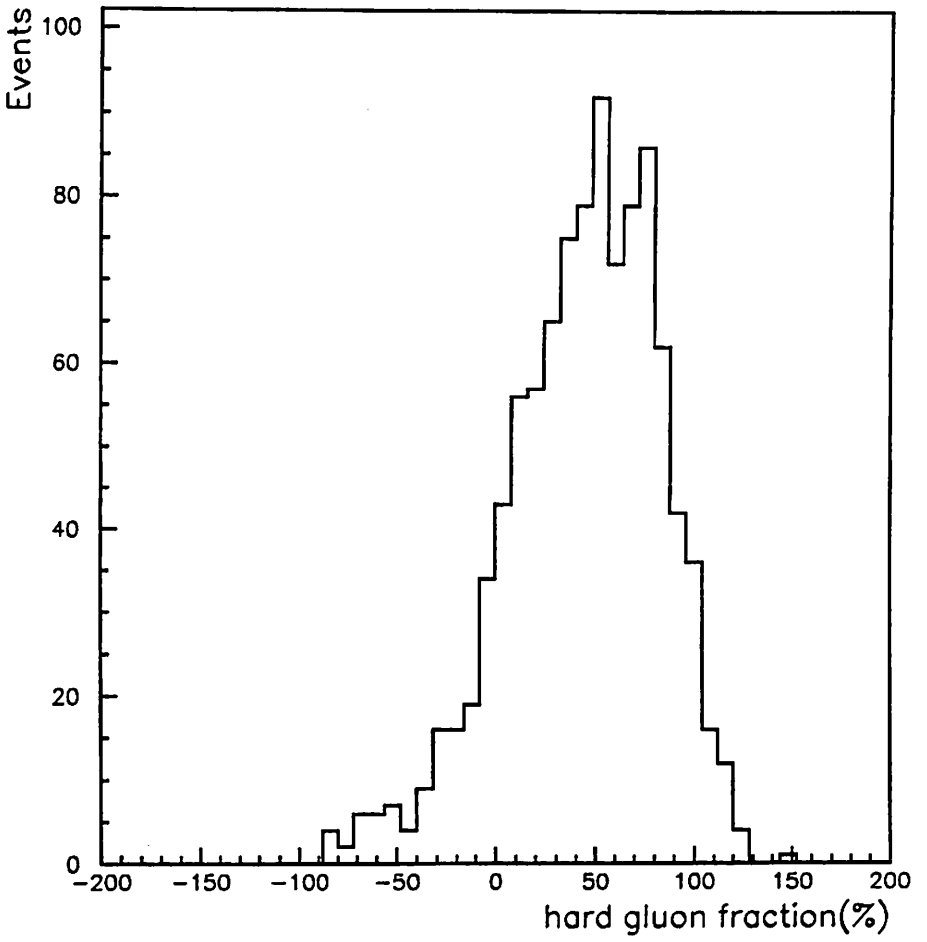

Figure 6.12: The distribution of estimated hard-gluon fraction on pseudo experiments using 2-parameter fit.

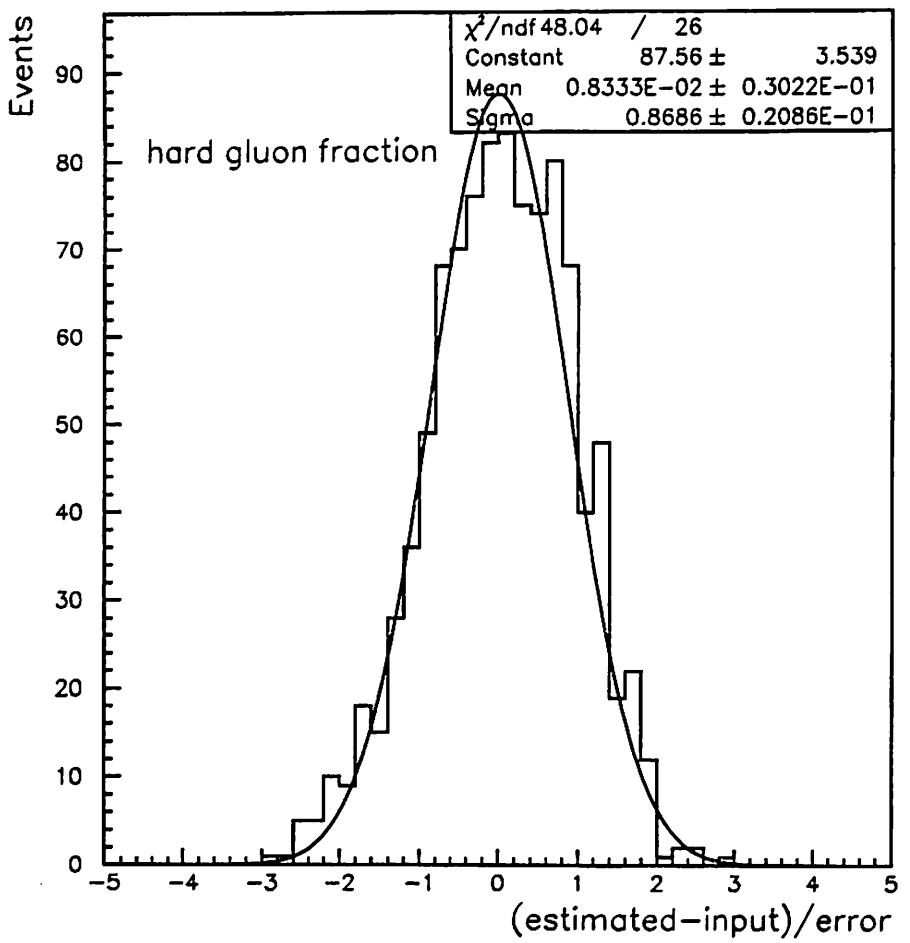

Figure 6.13: The pull distribution of hard gluon fraction on 2-parameter fit.

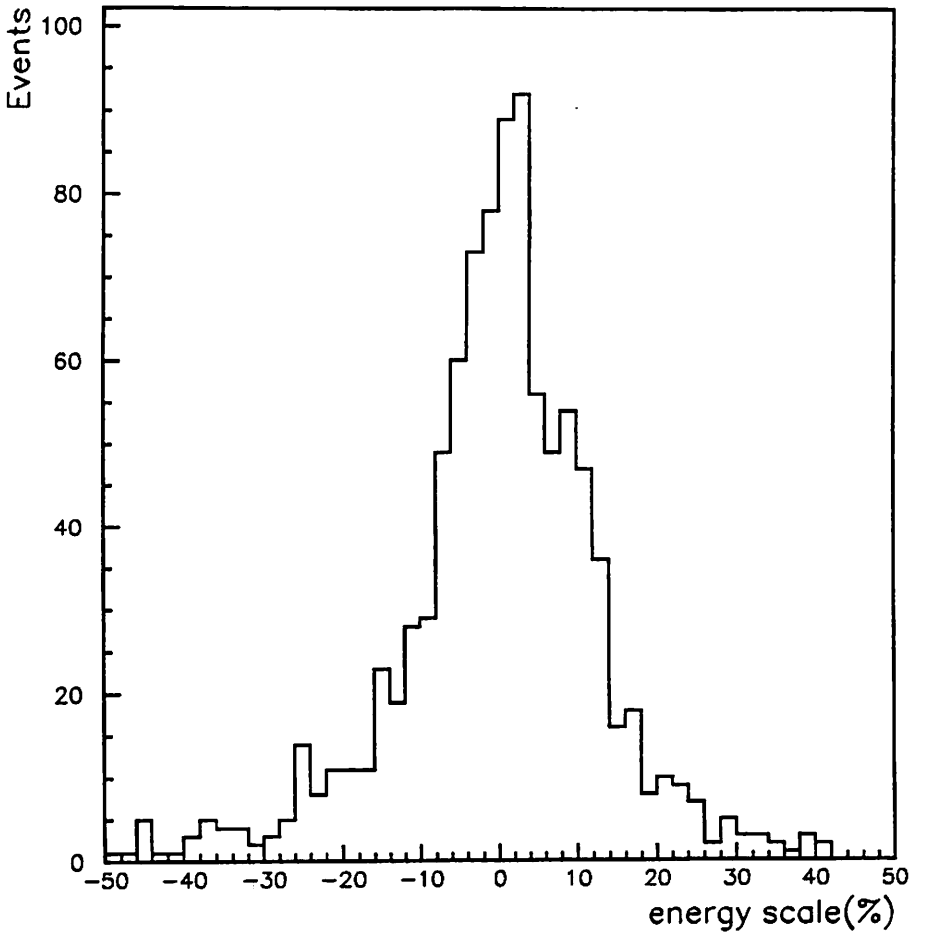

Figure 6.14: The distribution of estimated jet energy scale on pseudo experiments using 2-parameter fit.

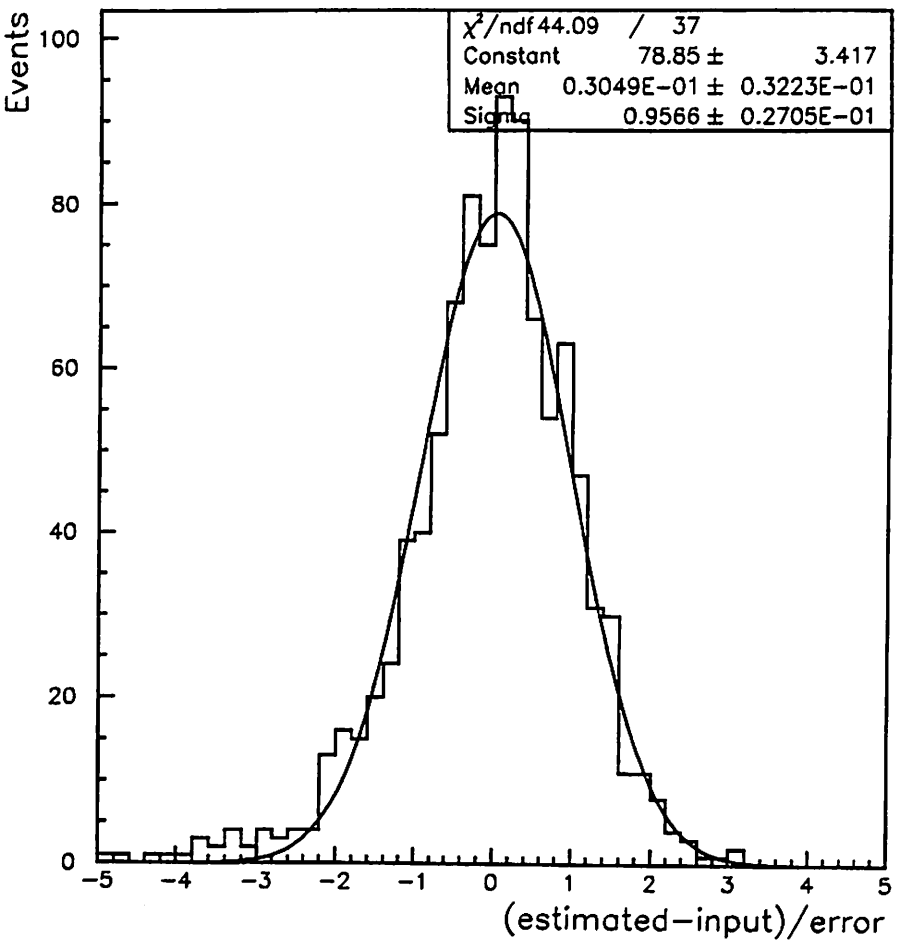

Figure 6.15: The pulls distribution of energy scale on 2-parameter fit.

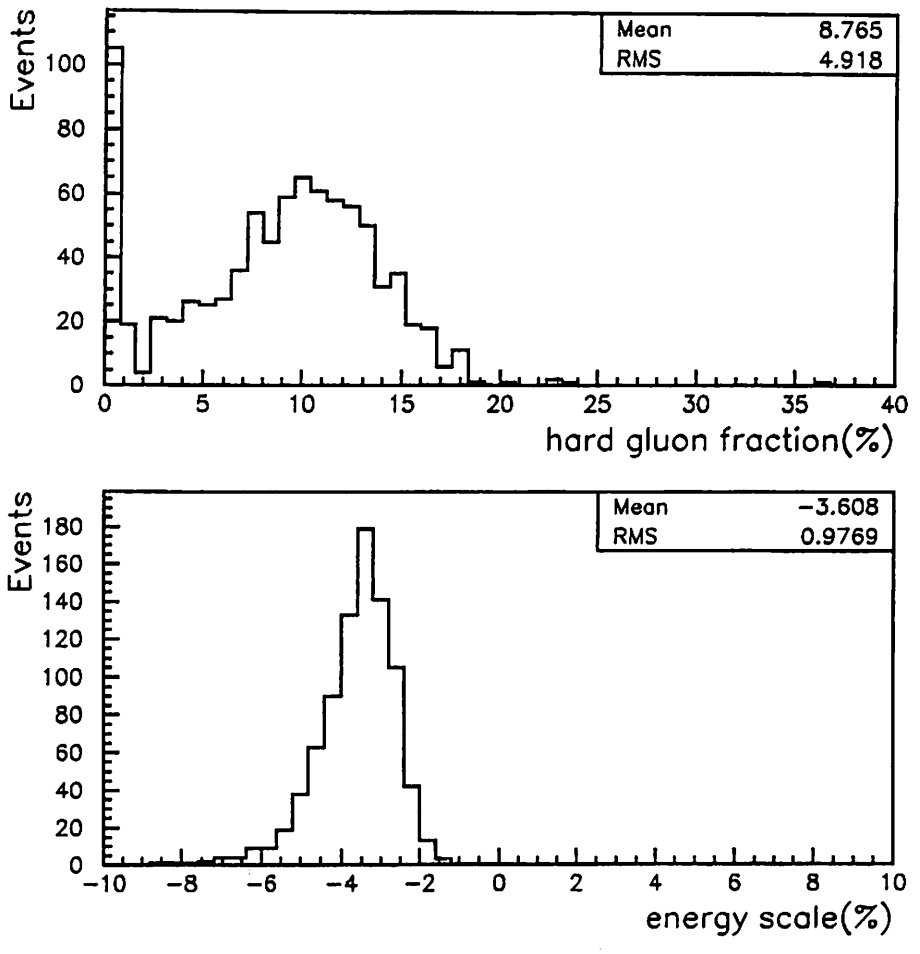

Figure 6.16: Top(Bottom) plot shows the estimated hard gluon fraction(energy scale) on pseudo experiments where templates were fluctuated using Poisson statistics.

Chapter 7

Top Quark Mass Reconstruction

The method of top quark mass reconstruction is based on the kinematical hypothesis on the top quark decay process as

$$\begin{aligned} p\bar{p} &\rightarrow t\bar{t} + X \\ &\rightarrow l\nu_l b_l + q\bar{q}b_j + X \end{aligned}$$

In order to determine a value of M_{top} event-by-event, we require each event to have four jets. This means we can match the jets with the quarks one-to-one. The 4 momenta of the 6 partons are optimized by a "mass fitter" which will be described in the following sections.

7.1 Fitting Method

The fitting procedure is basically a method of a χ^2 minimization. The fit is made for all jet configurations under the constraint that the b-tagged jet must be a b-quark. In assigning jets to quarks from top quark decay in each event, the four highest E_T jets are used to reduce the combinatoric possibilities. The other jets are used only in recomputing the missing E_T in each minimization attempt, and are not used in making invariant masses during the fit. In this analysis as we require two b-tagged[1] jets in an event, we only need consider two jet cofigurations. We use the MINUIT program for a χ^2 minimization.

The χ^2 consists of two pieces:

1. The physics constraints

2. The detector systematics

The physics constraints are the 2-body and 3-body invariant masses, which are given in the χ^2 as follows:

$$\chi^2 = \frac{(m_{l\nu} - M_W)^2}{\Gamma_W^2} + \frac{(m_{jj} - M_W)^2}{\Gamma_W^2} + \frac{(m_{l\nu j} - M_{top})^2}{\Gamma_{top}^2} + \frac{(m_{jjj} - M_{top})^2}{\Gamma_{top}^2}$$

where $M_W = 80.2$ GeV/c^2, $\Gamma_W = 2.1$ GeV, $\Gamma_{top} = 2.5$ GeV and M_{top} is a free parameter.

The detector systematics are included only as an overall scale factor f on the measured 4-momenta which are not allowed to change the direction but

[1]One of tagged jet must be tagged by SVX or SLT algorithm.

are allowed to change the energy scale for each measured objects as given by. The additional terms are added into the above χ^2

$$\frac{(f-1.0)^2}{\sigma_f^2},$$

The assumed resolutions are

$$\frac{\sigma_f}{f} = \begin{cases} 13.5\%/\sqrt{E_T} \oplus 2\% & \text{for electrons} \\ 0.11\% P_T & \text{for muons} \\ F(E_T) & \text{for jets} \end{cases}$$

where F is the energy resolution as a function of jet E_T described in Section 4.2.2 .

One of the other remaining unaddressed elements is the z-momentum of neutrino, its transverse components being fixed by the other objects. In principle, the P_Z of the neutrino has two solutions for each configuration, and the fit is redone at each P_Z solution for each assignment of the jets, unless the solutions are imaginary.

Another element is the jet energy corrections which are applied in order to infer the quark momenta from the measured jet energies. The correction functions for general jets were developed for QCD jet studies. In the determination of the top quark mass, we make use of an improved set of corrections which are more appropriate for top quark production events. These corrections account for the energy sharing between different jets in top quark production events as described in Section 4.2.2.

7.1.1 Test of the method with Monte Carlo events

To verify the reconstruction method and look at its performance, we perform the top quark mass fitting on Monte Carlo events. We use HERWIG $t\bar{t}$ and VECBOS W+jets Monte Carlo events passing the standard event selection described in Chapter 4.

A performance which we try to improve is the resolution of mass spectrum. It depends on the efficiency for getting the correct jet configuration.

The efficiency clearly depends on the number of jet combinations which the mass fitter has to evaluate. If we know one or two of 4 leading jets are b-jet, the mass fitter has a high efficiency for getting the correct jet configuration.

We compare 3 cases:

1. without b-tag information
2. with one b-tag information
3. with two b-tag information

Figure 7.1 shows the reconstructed mass distributions on HERWIG Monte Carlo events at M_{top} of 175 GeV/c^2. The top plot shows the distribution where the mass fitter does not use any b-tag information. It means the mass fitter evaluates all combinations of 24. As with all following figures, the solid histogram shows the mass spectrum chosen by the mass fitter and the dashed histogram shows the mass spectrum for the correct jet configuration. The middle plot shows the reconstructed mass distributions where one of b-jets is tagged by the b-tagger. It means the mass fitter evaluates 12 combinations.

The bottom plot shows the reconstructed mass distributions where two b-jets are tagged by the b-tagger. It means the mass fitter evaluates 2 combinations.

As a result, we see the highest efficiency for getting the correct jet configuration on double b-tagged events as expected above. In this analysis, we use double b-tagged events only. The mass distribution for the correct jet configuration has a little lower mean value. Assuming the shifts are due to the mass fitter, the real data shifts lower by the same amount. It is corrected in the top mass reconstruction.

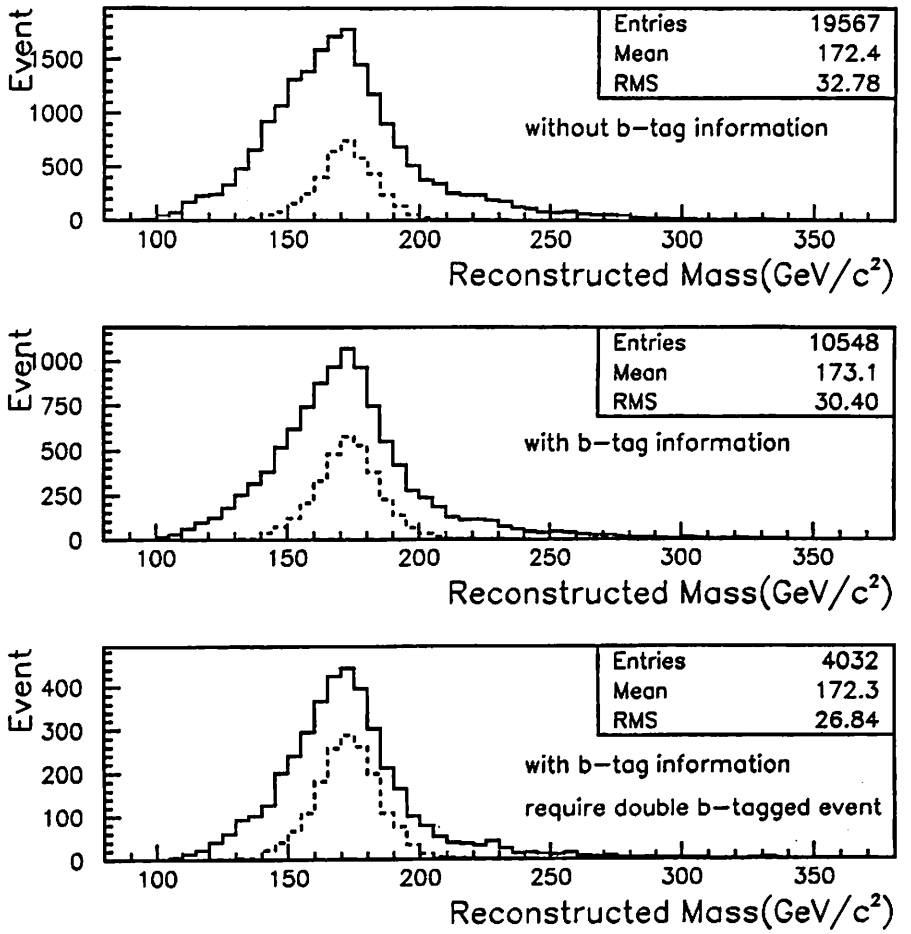

Figure 7.1: Distributions of reconstructed mass for 3 kinds of b-tag requirement. Top plot shows that without b-tag information. Middle plot shows that with one b-tag information. Bottom plot shows that with two b-tag information.

7.1.2 The W mass window cut

In order to reduce the acceptance for high E_T jets which do not originate from the quarks from top quark decay, we apply the W mass window cut that two leading untagged jets should have an invariant mass between 60 and 100 GeV/c^2. The cut and the width of the window are based on Monte Carlo study.

On HERWIG $t\bar{t}$ Monte Carlo events, we look at the top quark mass uncertainty (r.m.s./$\sqrt{N}$) for various W mass window cuts, including the case without W mass window cut. We also examine the rejection power for VECBOS W+jets background events. The rejection factors are normalized to that without W mass window cut. Figure 7.2 shows both quantities for various W mass window. The top quark mass uncertainty (r.m.s./$\sqrt{N}$) increases rapidly around 70~90 GeV/c^2 window. On the other hand, the background contamination decreases with a narrower window.

Another optimization was carried out with pseudo-experiments on Monte Carlo events. We made the same amount of Monte Carlo events as the real data and applied various W mass window cuts. Events that survived the cut are fitted with corresponding mass templates. We repeated this pseudo-experiments 100 times and looked at the mean values of the fitted mass uncertainty. The mean of the uncertainties for the mass window of 40~120 GeV/c^2, 50~110 GeV/c^2 and 60~100 GeV/c^2 are consistent with each other within the errors.

Thus we set the W mass cut window to 60~100 GeV/c^2 which has the most powerful rejection power against the background events.

W window cut	Mean of the uncertainty
No W mass cut	9.6±0.4
40∼120	8.8±0.4
50∼110	8.8±0.4
60∼100	8.2±0.4
70∼90	10.4±0.6

Table 7.1: The mean of the uncertainty of fitted mass for various W mass window cuts.

7.2 Top quark mass from double b-tagged events

We found 9 double b-tagged events in 110pb^{-1} data after the W mass window cut. The dijet masses and the reconstructed top quark masses are shown in Table. 7.2.

7.3 Likelihood fitting

The expected number of background events is 0.4±0.1 provided by Reference[22]. To extract the top quark mass, we fit the reconstructed top quark mass distribution of the nine events to the sum of the expected mass distributions of the W+jets background and the $t\bar{t}$ signal with a top quark mass M_{top}, using a maximum likelihood method. The likelihood function is

Event	tags	dijet mass (GeV/c^2)	Reconstructed mass (GeV/c^2)
40758-44414	SVX+SVX	82.3	173.2±8.6
59698-31639	SVX+JPB	79.6	187.5±10.3
63247-65096	SVX+JPB	81.4	161.1±8.1
64721-229200	SLT+SLT	81.7	181.1±14.5
65298-747402	SLT+JPB	60.1	149.7±8.8
65581-322592	SVX+SLT	66.2	152.5±9.0
67824-281883	SVX+SLT	73.3	170.2±11.2
67971-55023	SVX+SVX	98.2	184.3±11.5
68464-547303	SVX+SVX	87.3	151.0±8.4

Table 7.2: Top quark masses for 9 double b-tagged events.

given by

$$L(n_s, n_b, M_{top}) = \frac{1}{\sqrt{2\pi}\sigma_b} e^{\frac{(n_b - Nb)^2}{2\sigma_b^2}} \frac{e^{-(n_b+n_s)}(n_b+n_s)^N}{N!} \prod_{i=1}^{9} \frac{(n_b f_b + n_s f_s(m_i, M_{top}))}{(n_s+n_b)}$$

where N is total number of events(9), N_b is the expected number of background events(0.4) and σ_b is its uncertainty (0.1). n_b and n_s represent the numbers of backgrounds and signal events, respectively. The variable $f_s(m_i, M_{top})$ is the normalized top Monte Carlo mass distribution and f_b is the normalized W+jets background Monte Carlo distribution. The variable m_i is the top quark mass that gives the maximum likelihood for the fit.

7.3.1 Test of fitting procedure

In order to verify our fitting procedure, we generated 500 sets of 9 HERWIG $t\bar{t}$ events without any background contribution and repeated the mass

fitting procedure. The distribution of pulls (M_{top}^{fitted} - $M_{top}^{generated}$) / ΔM_{top} is shown in Fig. 7.3. This distribution should have a mean of 0.0 and a sigma of 1.0. The mean value in Gaussian fitting is consistent with 0 and the sigma is consistent to 1 within a 1.2σ.

7.3.2 Extracting a top quark mass

We performed the mass fitting procedure on the 9 events where the number of background events was constrained to 0.4 $\pm$ 0.1. The fitted mass is 174.8 $\pm$ 7.6 (statistical only) GeV/c^2 as shown in Fig. 7.4.

7.3.3 Pseudo experiments

Then we performed "pseudo experiments" with Monte Carlo events. We made 1000 samples with the 5% background contamination and repeated the mass fitting. Figure 7.5 shows the fitted mass and its error. The arrows indicate the value of CDF data. Figure 7.6 shows the distribution of minimum -log(likelihood). The arrow also indicates the value of the CDF data. These CDF values are clearly consistent with the expectation from Monte Carlo results.

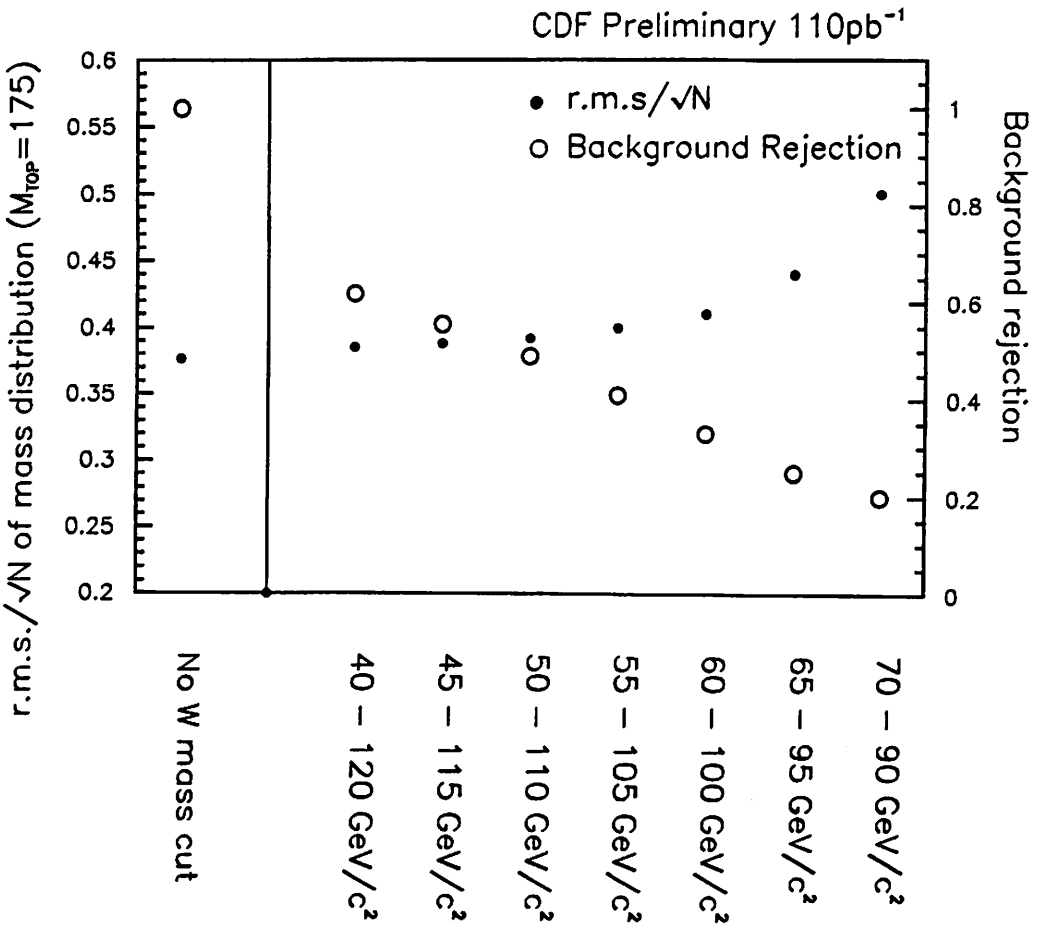

Figure 7.2: The plot of r.m.s. of reconstructed top mass divided by $\sqrt{N}$ where N is the number of events passing the W mass window cut and background rejection for various W mass window cuts.

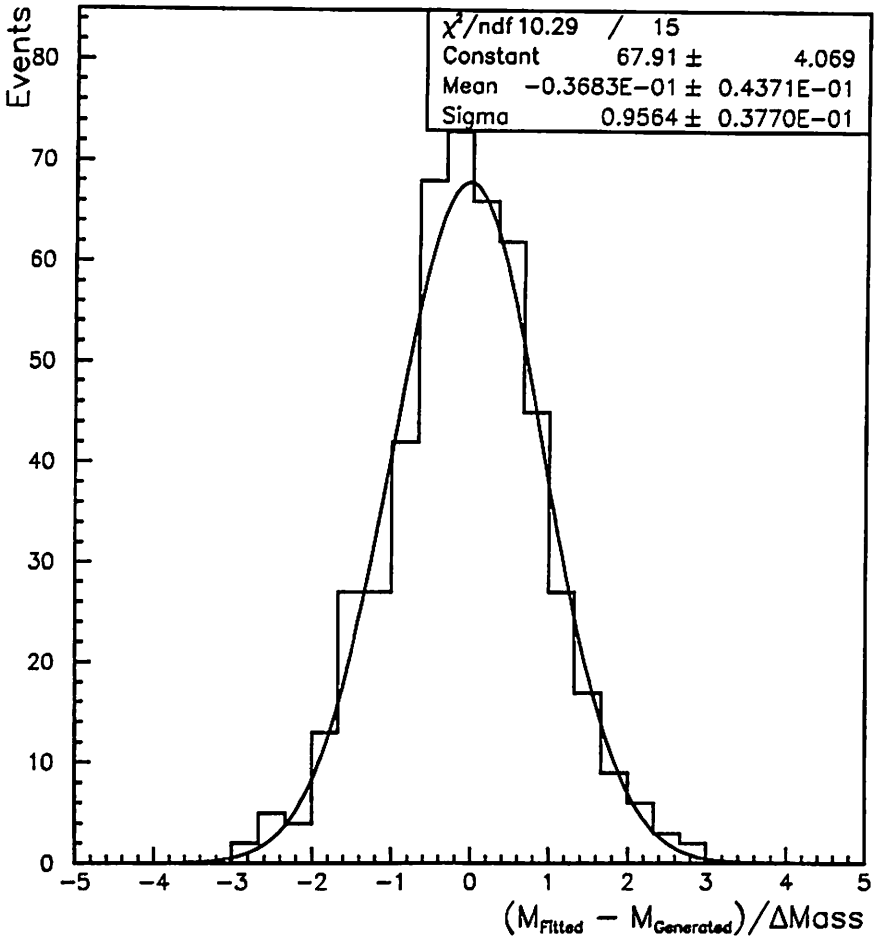

Figure 7.3: Pull distribution obtained from Monte Carlo experiments, where the pull is the difference between the fitted mass and generated mass 175 GeV/c^2, divided by its error.

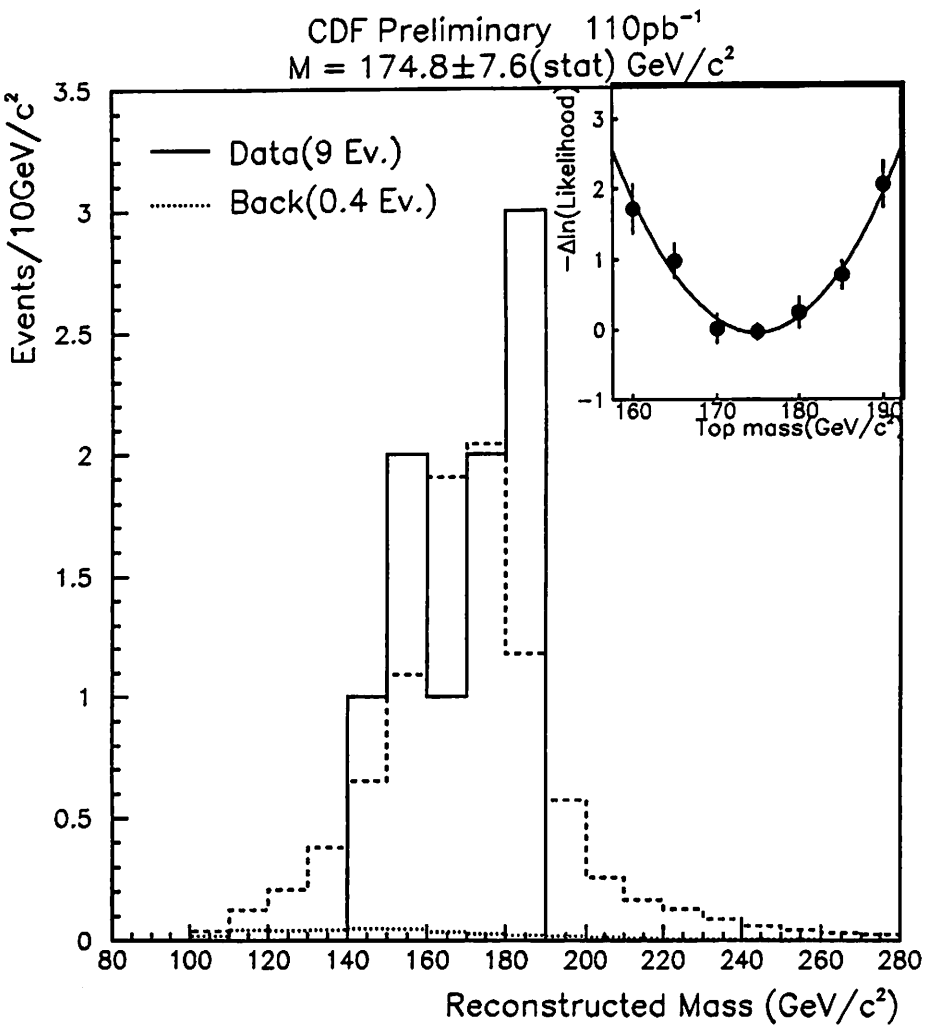

Figure 7.4: Result of likelihood fit with constrained background. Number of background events is constrained to 0.4±0.1. Extracted top mass is 174.8±7.6 GeV/c^2. Extracted number of background events is 0.04±0.01. Dashed histogram shows the mass distribution for the sum of the $t\bar{t}$ events (M_{top}=175 GeV/c^2) and W+jets background events. Dotted histogram shows that of background events.

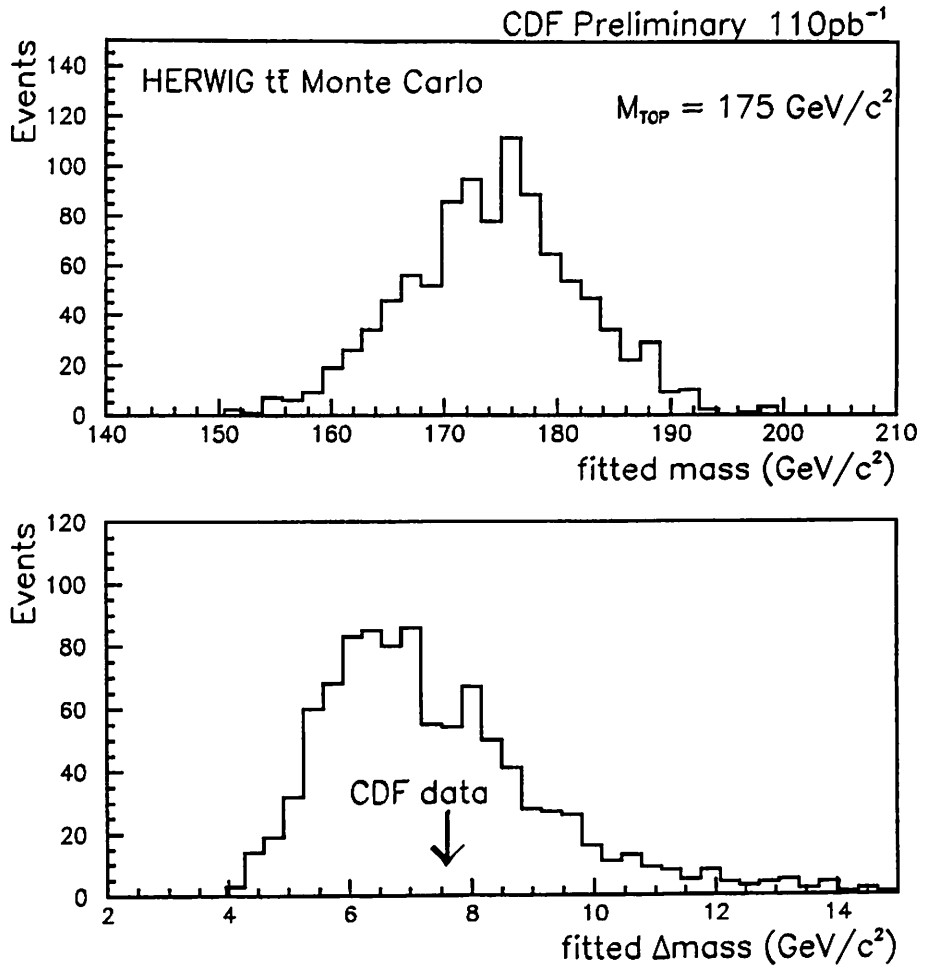

Figure 7.5: Mean(top plot) and spread(bottom plot) of the top masses on 9 event pseudo experiments. An arrow indicates the value of the CDF data.

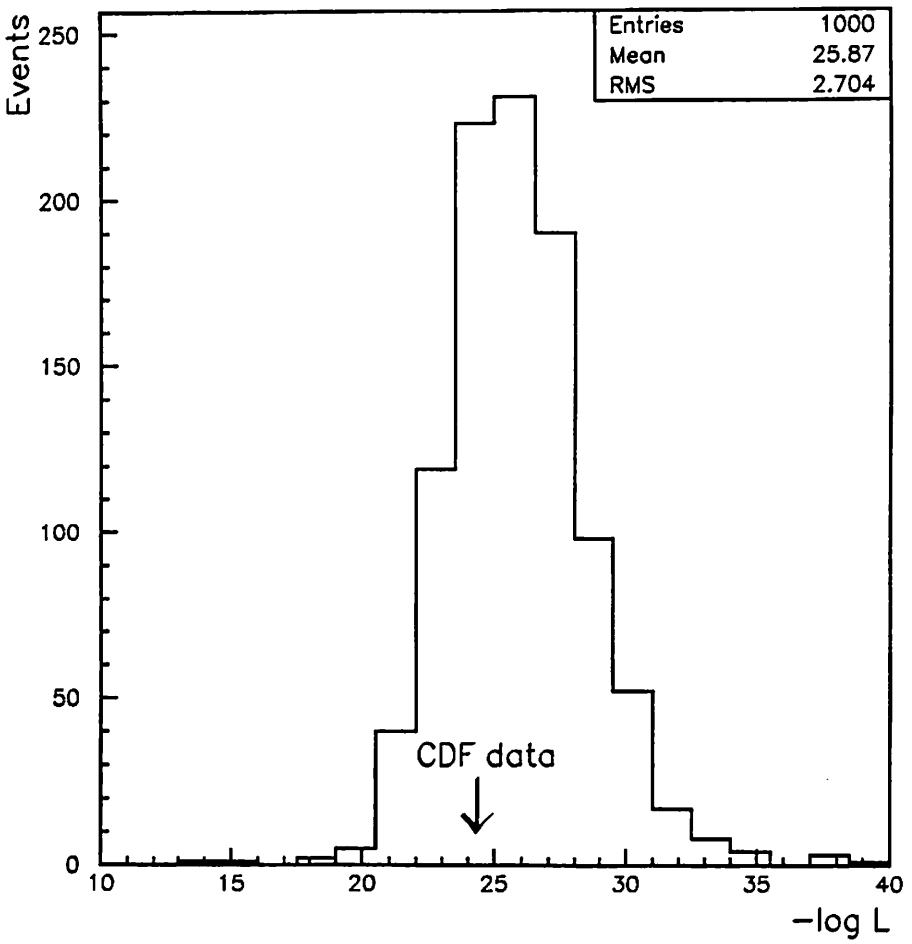

Figure 7.6: Minimum -log(L) distribution for top+background pseudo experiments. Arrow indicates the value of the CDF data.

Chapter 8

Systematics of Top Quark Mass Measurement

The systematic uncertainties in top quark mass arise from the uncertainties categorised as follows:

1. Jet energy scale uncertainty
2. The contamination of high E_T gluon jets
3. Systematic shifts of the E_T spectra of signal and background introduced by the b-tagging
4. The likelihood method uncertainty
5. Uncertainty in the mass fitting procedure.

Each of the above uncertainties is discussed in the following sections.

8.1 Jet energy scale

The uncertainty in the jet energy scale has several contributions. Generally the cluster energy obtained by using the CDF calorimeters is corrected by the offline correction program to get the correct jet energy. The correct jet energy was obtained by

$$P_T^{cor} = P_T^{raw} \times f_{rel} \times f_{abs} - UE + OC$$

where f_{rel} indicates the correction factor for the relative response depending on η position. f_{abs} indicates the correction factor which makes the absolute energy scale correction, UE takes into account the underlying event and OC corrects for the jet energy outside the jet cone of radius 0.4. So we have to consider the uncertainty on these corrections.

1. The absolute jet energy scale uncertainty
2. The relative jet energy scale uncertainty
3. Soft gluon radiation effects which covers uncertainties on jet energy with the cone of radius from 0.4 to 1.0
4. An additional $\pm$1GeV uncertainty to take into account the uncertainty on jet energy beyond the cone of radius 1.0

We estimate the first two uncertainties on the energy inside the clustering cone of radius 0.4. Next we estimate the last two uncertainties on the energy outside the cone.

For the estimation of these uncertainties, we shift the raw jet E_T, go through the event selection, correct the jet momenta, get the b-tagging information, apply the top specific jet correction and perform the top quark mass fitting. Then we perform 9 events pseudo-experiments to look at the systematic mass shift after the likelihood fitting.

8.1.1 Absolute jet energy scale

The uncertainty in the absolute jet energy scale due to the detector effects is given by "Behrends curve"[24]. This curve gives the uncertainty on the jet E_T due to the absolute correction factors. The curves include uncertainties on

- Detector effects, like pion response in the calorimeter etc..
- The fragmentation model
- The underlying event correction for the jet is considered. We added another term for the uncertainties in the UE corrections for events with many vertices.

We parameterized the curve using a polynomial function as shown in Fig. 6.9 and applied it to raw jets. The uncertainties in the detector stability and underlying events are also added in a quadrature.

$$f = \text{Behrends curve} \oplus \text{stability}(2\%) \oplus \text{UE}(0.1\text{GeV})$$

Figure 8.1 shows the distributions of the fitted mass for the positive and negative shifts. From the means of these distributions, we estimated the uncertainty to be $^{+2.0}_{-2.9}$ GeV/c^2.

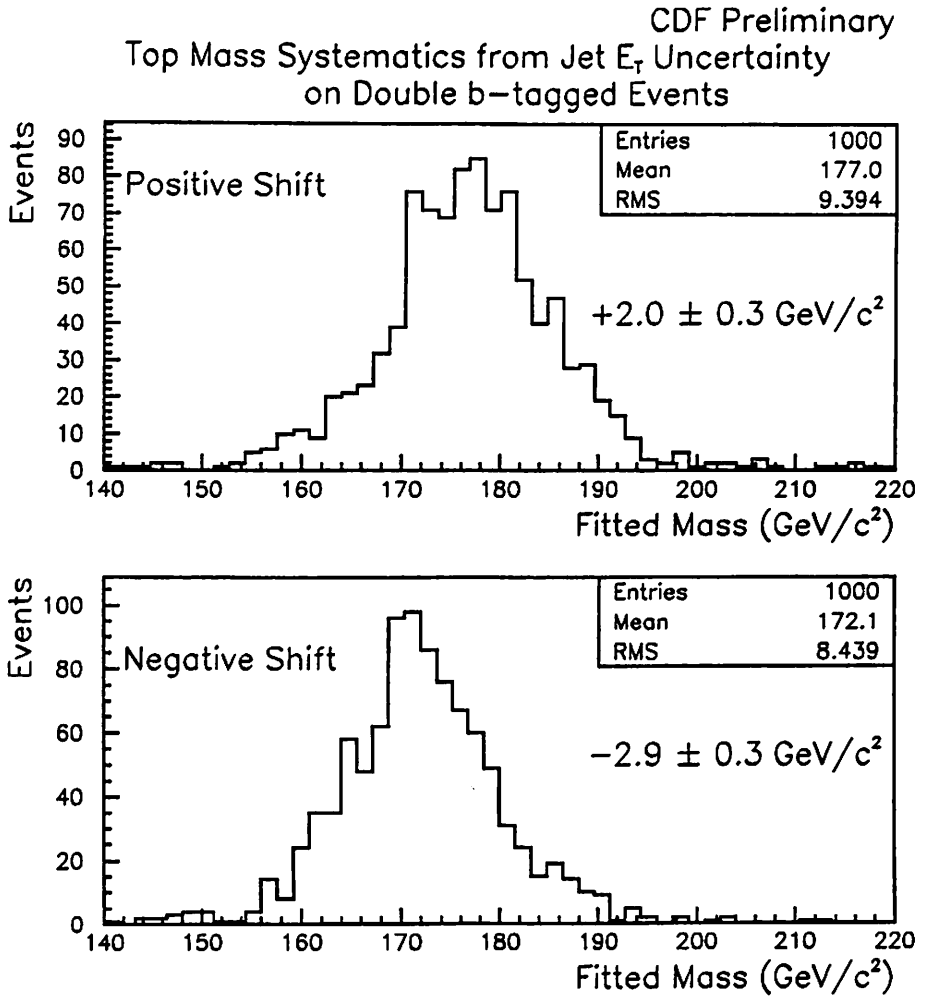

Figure 8.1: The top(bottom) plot shows the distribution of fitted masses for pseudo experiments with a positive(negative) E_T shift applied to the jets. The magnitude of the shift followed the "Behrends curve". The uncertainties on detector stability and underlying event are also applied.

8.1.2 Relative jet energy scale

The uncertainty in the relative correction factor f_{rel} is assumed to be $\pm 2\%$ of the correction. The estimation is carried out in the same way as above. The deviations from the mean value of 175 GeV/c^2 are $+0.0 \pm 0.3$ GeV/c^2 and $+0.2 \pm 0.3$ GeV/c^2, respectively. We estimated the uncertainty to be 0.1 GeV/c^2.

8.1.3 Jet energy scale in detector simulation

A +2% shift in the detector simulation is taken into account due to an additional systematic energy scale shift between Run0 and Run1B. The overall effect is a -2% shift in the "data sample" used for the estimation. We simply shift the raw jet energy scale by +2%. We estimated the uncertainty to be 1.0 GeV/c^2.

8.1.4 Soft gluon radiation

A theoretical uncertainty in jet energies can arise from the possibility of large-angle gluon radiation which may not be modeled correctly in parton shower Monte Carlo programs. The "soft gluon radiation" means the gluon radiation which causes a loss of the initial parton energy outside a jet cone and resuls in a minimal deviation of the reconstructed jet direction from the original parton direction, but is not reconstructed as a separate jet due to its insufficient energy below a jet E_T threshold of 8 GeV.

The extensive studies of a single jet in Z,W and photon sample have been

done by taking the difference of P_T's measured by two different sizes of jet cones, R=0.4 and 1.0, in order to estimate the uncertainty in the jet energy scale due to the soft gluon radiation. The raw jet E_T observed in the jet cone radius of 1.0 must be larger than that observed in the jet cone radius of 0.4 due to the energy flow outside of the smaller cone.

A useful quantity for characterizing jet fragmentation is the energy flow around the jet axis. This can be measured by plotting the measured E_T in an annulus around the jet axis between radius of 0.4 and 1.0. The plots show the agreement better than 2% for a jet E_T above 30 GeV, rising to 4−6% at the minimum E_T of 8 GeV[25]. We define the quantity F for a jet by

$$F = [P_T(1.0) - P_T(0.4)]/P_T(0.4)$$

where $P_T(1.0)$ and $P_T(0.4)$ are jet P_T with a cone radius of 1.0 and 0.4, respectively. Then the quantity DF = F(data)−F(Monte Carlo) in bins of P_T is plotted as a function of P_T as shown in Fig. 8.2. We shifted the jet energy scale using this curve in both positive and negative directions. The distribution of fitted mass are shown in Fig. 8.3. From the mean value we estimated the uncertainty to be $+0.8\pm0.2$ GeV/c^2 and -0.5 ± 0.2 GeV/c^2 for positive and negative shifts, respectively.

Another uncertainty comes from the jet energy flow outside the cone of 1.0. It has been considered as an additional energy uncertainty of 1 GeV. Simply we shifted the corrected jet energy by ±1GeV and looked at the fitted mass. We estimated the uncertainty to be $+1.6\pm0.2$ GeV/c^2 and -1.0 ± 0.2 GeV/c^2 as shown in Fig. 8.4.

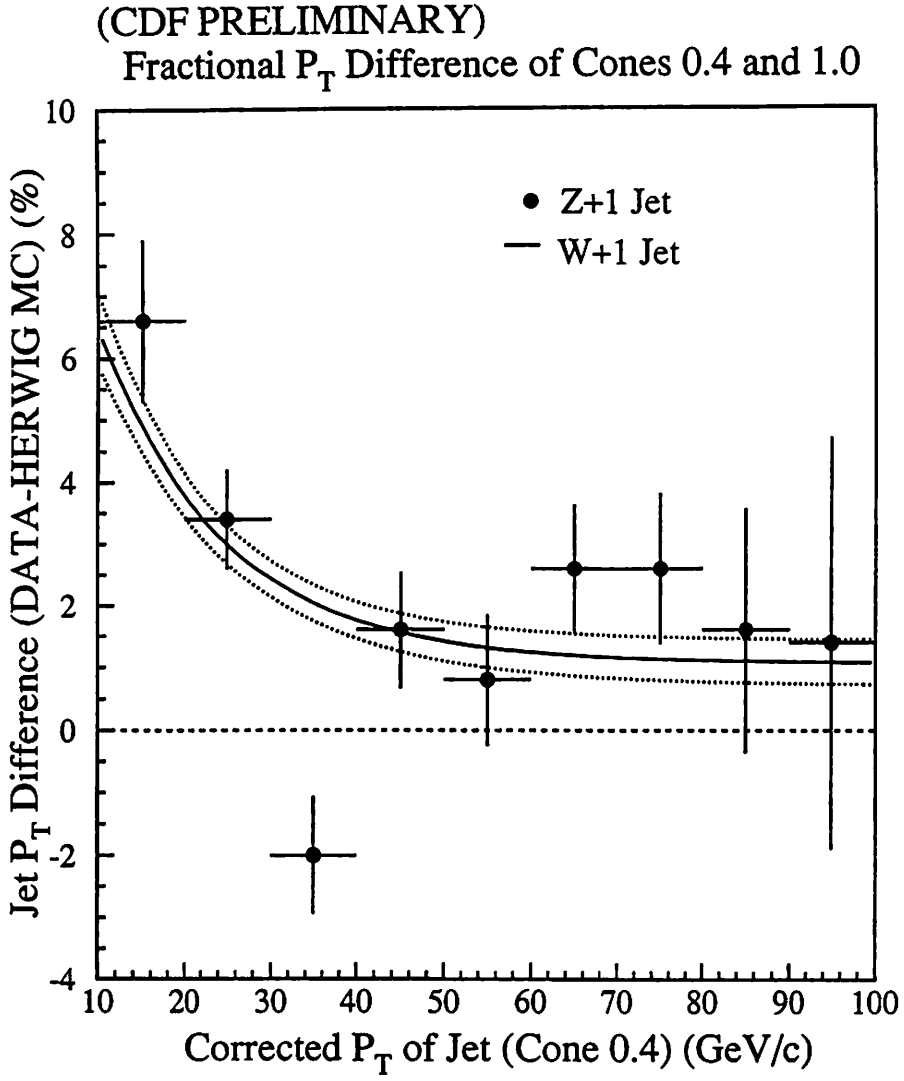

Figure 8.2: The plot of DF versus P_T of the jet. Solid lines shows the curve for W+1jet events, Black points shows for Z+1jet events. The curve for W+1jet was used to evaluate the top mass uncertainty due to soft gluon radiation.

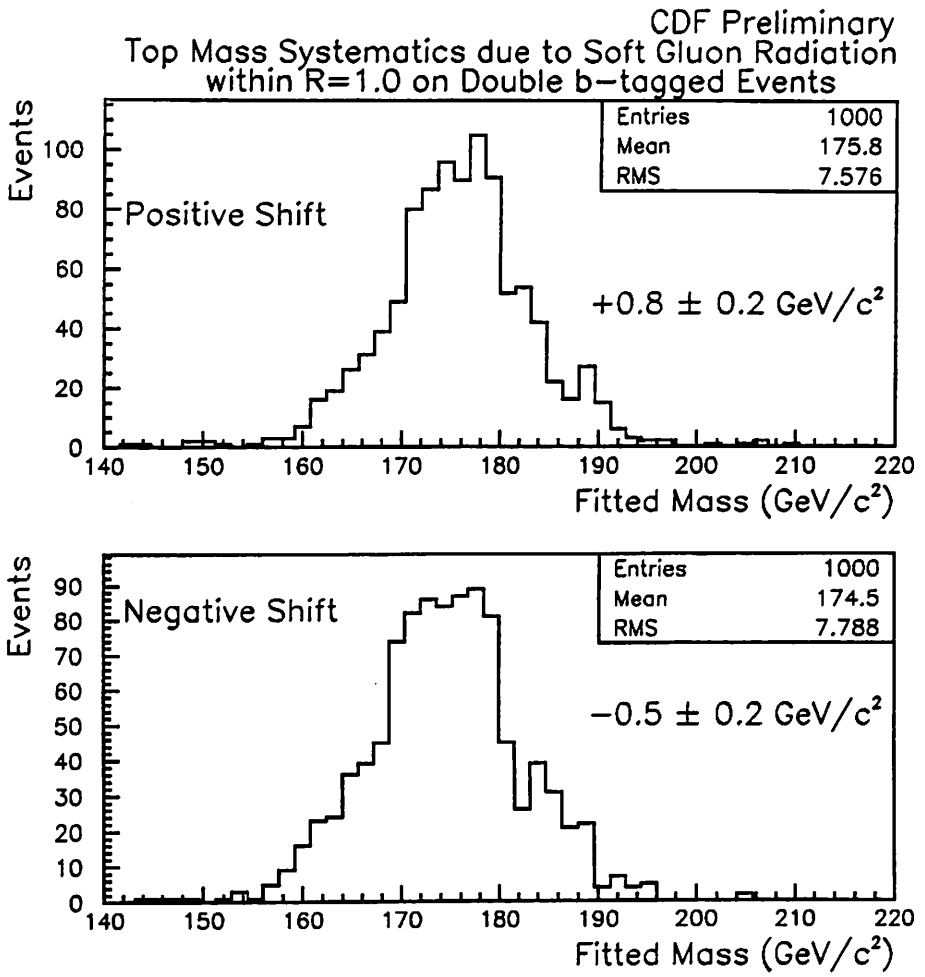

Figure 8.3: The distributions of fitted masses for pseudo experiments with positive(top plot) and negative(bottom plot) E_T shifts applied to the jets. The magnitude of the shift is fractional jet energy difference between data and Monte Carlo.

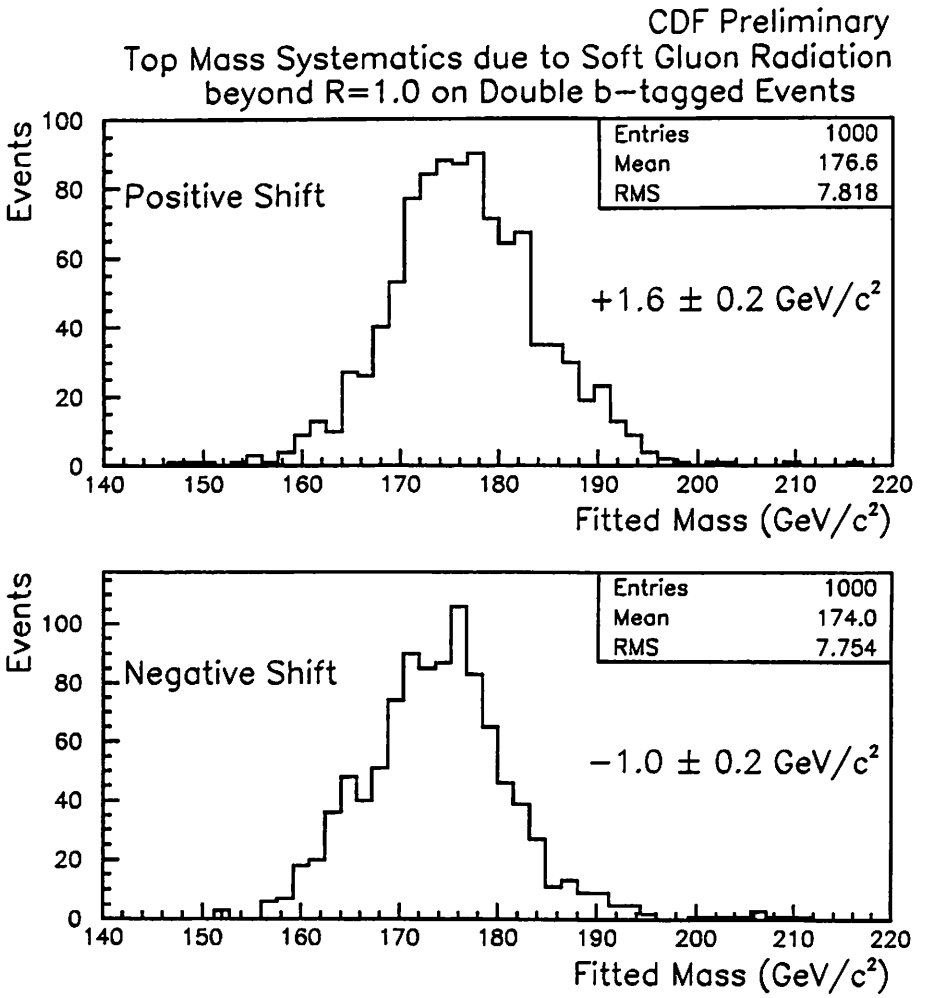

Figure 8.4: The distributions of fitted masses for pseudo experiments with positive(top plot) and negative(bottom plot) E_T shifts applied to the jets. The magnitude of the shift is obtained from the jet energy beyond a radius of 1.0.

8.2 Hard gluon radiation

The "hard gluon radiation" means the violent gluon radiation which results in an extra jet and causes mismatch between the parton and jets. In measuring the top quark mass we assume that the 4 highest E_T jets in the events are the jets associated with the partons from the top quark decay, two bottom quarks and two light quarks from a hadronic W decay. However Monte Carlo studies indicate that at least one of the 4 highest E_T jets does not match well with a parton frequently. These jets are typically due to gluons radiating from one of the initial or final-state partons. We refer to this radiation as hard gluon radiation and to the jets as gluon jets.

In order to distinguish between a gluon jet and a quark jet from the top quark decay, we try to match the primary partons from a HERWIG top decay with the 4 highest E_T jets passing the mass analysis selection criteria. We define a gluon jet by a jet which is away from any quarks from the top quark decay by larger than 0.4. Also we define a gluon jet event by an event which has at least one of the 4 highest E_T jets identified as a gluon jet. In HERWIG top quark decay, we found 30% of total events are the gluon jet event on the double b-tagged events.

To estimate the uncertainty on top quark mass measurement due to the hard gluon radiation, we compared top quark masses on the following three cases:

1. Events with no gluon jet

2. 30% gluon jet events(Standard HERWIG)

3. 100% gluon jet events

The results of pseudo-experiments are shown in Figs. 8.5 and 8.6. The mean of fitted mass distribution is not affected so much, but the uncertainty in the fitted mass clearly depends on the fraction of gluon jet event.

Ideally one would like to measure the amount of gluon radiation in the CDF data directly. Some studies have been done so far, but the significant measurement has not been achieved because of a limited statistics. In the present, as we do not have any information about the amount of gluon radiation in the CDF data, we assumed a flat distribution for hard gluon fraction pessimistically. It means all fractions are equally likely. Thus we use 60% confidence interval centered at 30%. The result is summarized in Table 8.1.

Gluon%	Mean Mass(GeV/c^2)	Mean Uncertainty(GeV/c^2)	Systematic(GeV/c^2)
0	175.8	7.1	3.5
20	175.8	7.8	2.5
30(standard)	175.3	7.9	—
40	174.9	8.2	2.2
60	174.8	8.7	3.6
80	175.0	8.9	4.1
100	173.9	9.9	6.0

Table 8.1: The mean of fitted mass and its errors for pseudo experiments with various amount of gluon jet compared to the standard HERWIG templates(30%).

The last column shows the additional systematic uncertainty to the statistical uncertainty of 7.9 GeV/c^2. We take ± 3.6 GeV/c^2 as the systematic uncertainty. Adding the mass shift of 0.7 GeV/c^2 in a quadrature, we obtain

the uncertainty of ± 3.6 GeV/c^2 from the 0% and 60% gluon fractions.

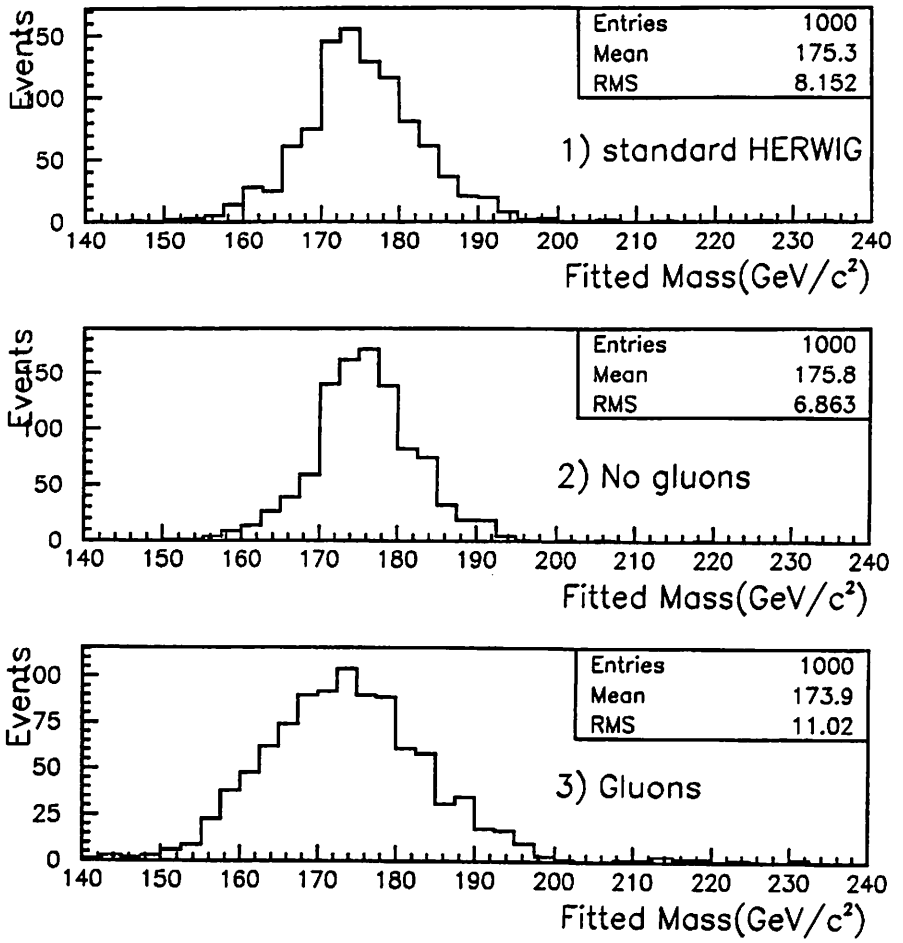

Figure 8.5: The mass distributions returned from the likelihood fitting for the three different pseudo-experiments : 1) standard HERWIG 2) events with no gluon jets 3) events with at least 1 gluon jet.

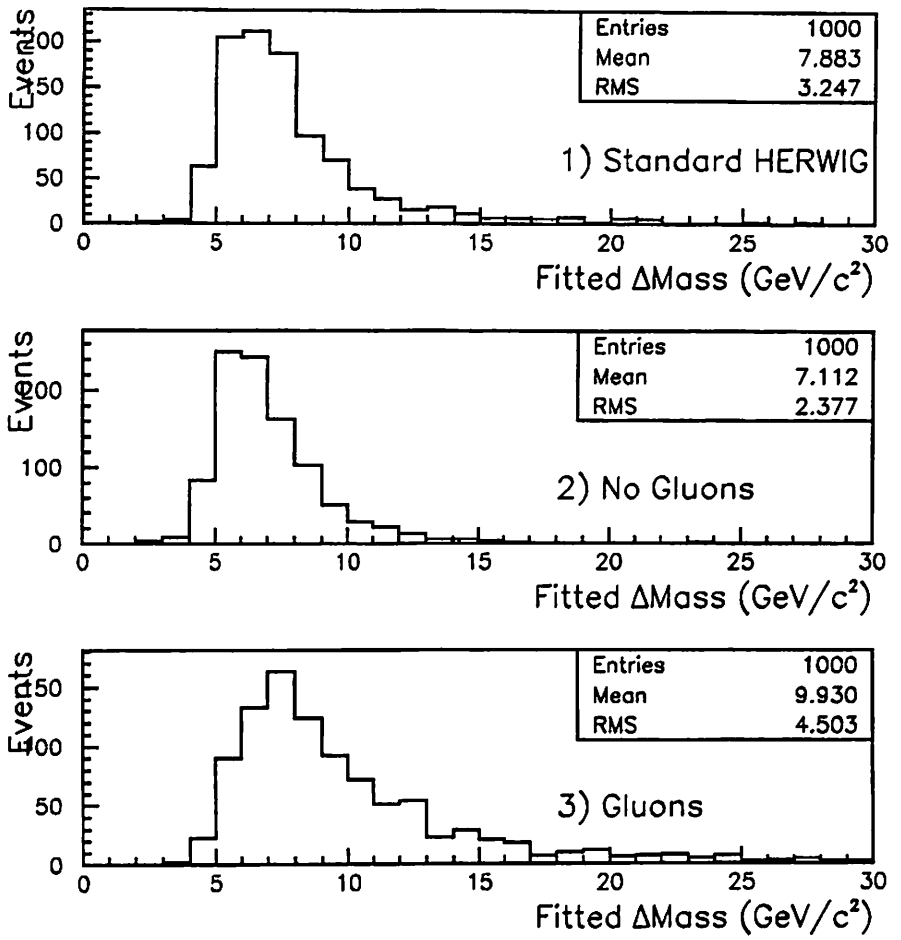

Figure 8.6: The distributions of uncertainties returned from the likelihood fitting for the three different pseudo-experiments : 1) standard HERWIG 2) events with no gluon jets 3) events with at least 1 gluon jet.

8.3 Different generators

So far, we have used HERWIG Monte Carlo for top signal but there is no proof that the fragmentation model is correct. Another fragmentation model of ISAJET is different from that of HERWIG. The comparison between these two Monte Carlos will provide a good evaluation of this uncertainty. We extracted double b-tagged events from ISAJET $t\bar{t}$ events and performed the top quark mass reconstruction. We carried out "pseudo experiments" using ISAJET samples and looked at the difference between two Monte Carlos. From the mean values of the mass distributions, we estimated the uncertainty to be ± 0.9 GeV/c^2.

8.4 Fit configuration

In this analysis, we used the MINUIT minimization routine to calculate a top quark mass. There is another "mass fitter" which uses SQUAW minimization routine. The uncertainty due to a fit configuration can be estimated by a comparison between the results of these two fitters. We performed "pseudo experiments" and obtained two top quark masses using the above two mass fitters. From the difference between the two masses, the uncertainty was estimated to be 0.3 GeV/c^2.

Another uncertainty which comes from the ambiguous solutions in the mass fitter is taken into account. We always have 2 different top mass solutions with its χ^2s. To evaluate the uncertainty, we take a weighted average of the 2 solutions. The weights are $\exp(-\chi^2/2)$. From the mean value of the

mass distribution, we estimated the uncertainty to be 0.9 GeV/c^2.

As a summary of the estimation, we added the above two uncertainties in a quadrature and obtained the systematic uncertainty of 0.9 GeV/c^2.

8.5 Tagging bias

8.5.1 Signal shift due to b-tagging

To estimate the b-tagging bias on the mass spectrum, a flat efficiency of 100% is used. It means that a tagged jet is always a true b-jet and the efficiency does not depend on the jet E_T. From the mean value of the mass distribution, we estimated the uncertainty due to the bias to be 2.0 GeV/c^2.

Another uncertainty arises from the uncertainty in the mistag event fraction. We know the mistag fraction is around 9% in our sample. We assigned the uncertainty of $\pm$9%. The results are shown in Table 8.2.

mistag fraction	Mean of fitted mass (GeV/c^2)	Mean of fitted uncertainty (GeV/c^2)
0%	175.1$\pm$0.2	7.0
9%(standard)	175.1$\pm$0.2	7.1
18%	175.2$\pm$0.2	7.2

Table 8.2: The mean of fitted mass and the uncertainty of fitted mass for various mixtures of mistag events.

As the mean values are consistent with each other within their error of $\pm$0.2 GeV/c^2, the top quark mass uncertainty is less than 0.2 GeV/c^2.

8.5.2 Background shift due to b-tagging

So far, we used the background spectrum where we did not require b-tagged jets because if we require double b-tagged jet on background events, the statistics is quite low. Ignoring the statistics, we perform the fit with b-tagged background shape. The fitted mass using the b-tagged background spectrum is 174.9±7.6 GeV/c^2. From this value, we estimated the uncertainty to be ±0.1 GeV/c^2.

8.6 Background spectrum

There are several kinds of background sources.

1. Background from W decay into τ and dilepton events. As the top templates include these events, we do not have to consider this effect here.

2. Q^2 definition in VECBOS:
   We made a mass fitting using VECBOS W+3jet with $Q^2 = \langle P_T \rangle^2$. Using VECBOS W+3jet with $Q^2 = M_W^2$, we found the difference between top quark masses with these two Q^2 definitions is less than 0.1 GeV/c^2. Mass spectrum with $Q^2 = \langle P_T \rangle^2$ is compared to that with $Q^2 = M_W^2$ in Fig. 8.7.

3. Statistical effect of Monte Carlo :
   To see the effect of statistics of background MC, we compared the results with and without smoothing. The uncertainty in top quark

mass was found to be less than 0.1GeV/c^2.

4. W+3jet vs. W+4jet :

   We used the VECBOS W+3jet background events. We need to compare it with the W+4jet background events. From the comparison between W+3jet with $Q^2 = \langle P_T \rangle^2$ and W+4jet with $Q^2 = \langle P_T \rangle^2$, we found the uncertainty to be less than 0.1 GeV/c^2. Both mass spectra are compared in Fig. 8.8.

From all of these results, we could not find any significant difference. This is a reasonable result because the background contribution is quite small.

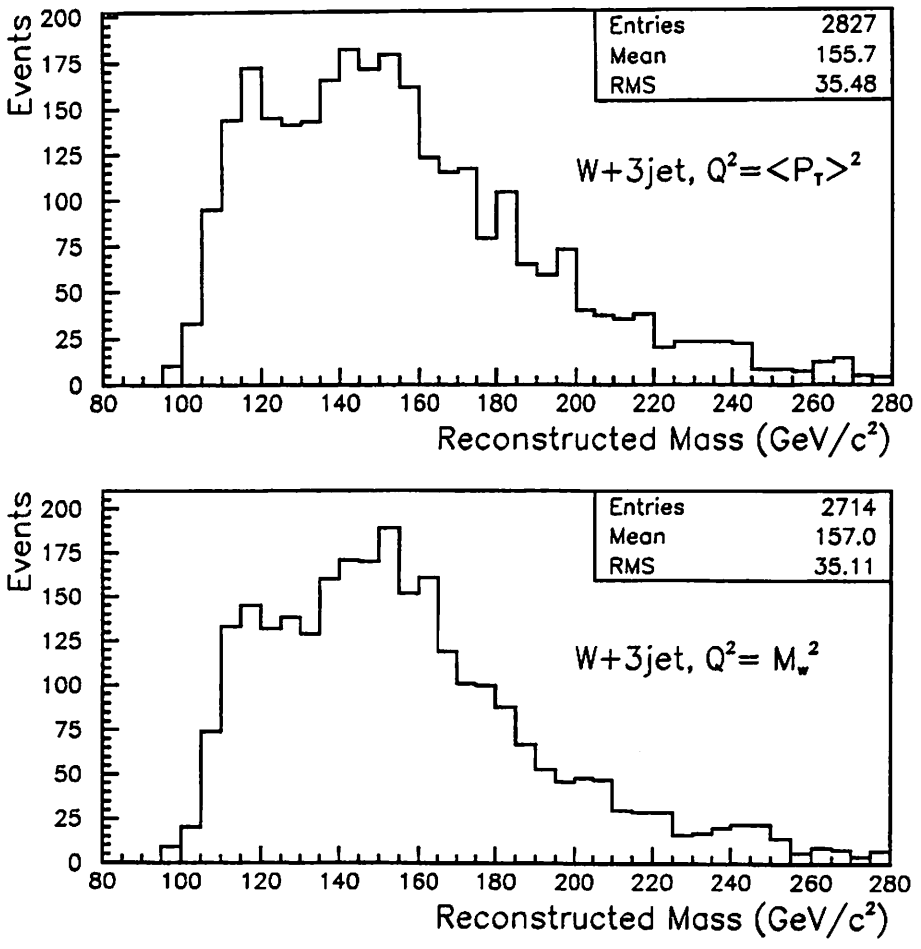

Figure 8.7: The mass distributions of background events for different Q^2 definition.

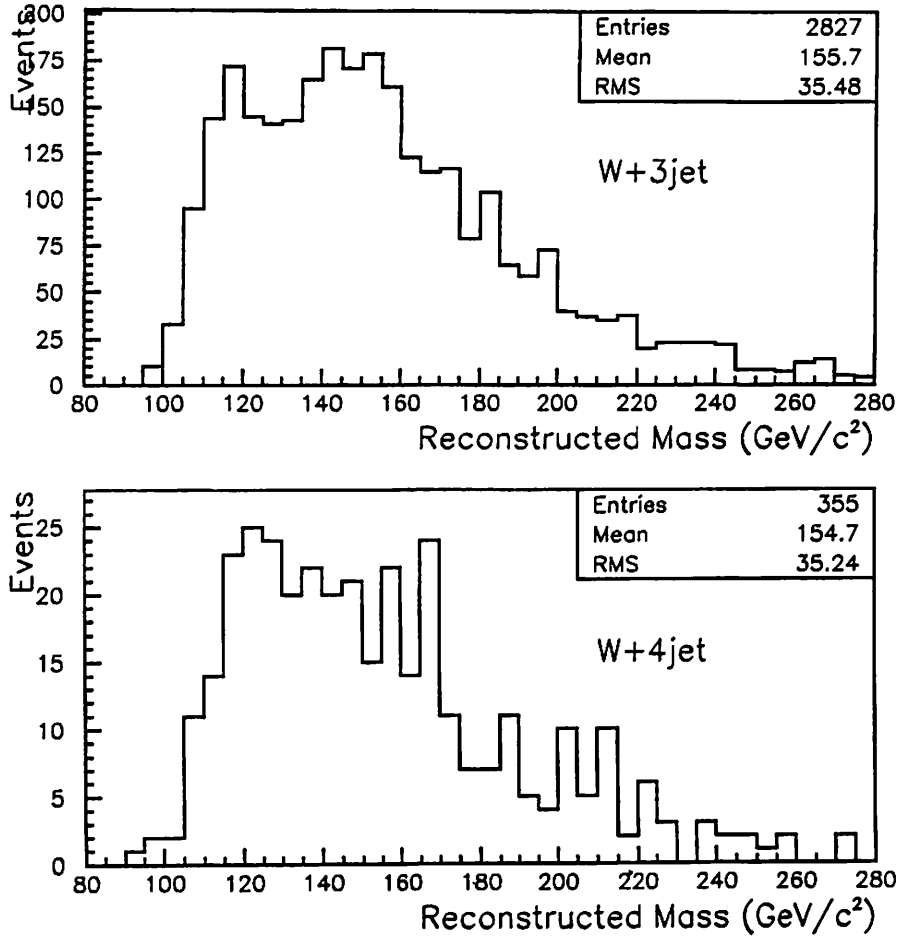

Figure 8.8: The mass distributions of background events for W+3jet and W+4jet.

Fit condition	Fitted mass	min(L)	α
n_b,n_s free No Gaussian term	174.6 ± 7.4	25.6	$0.00^{+0.16}_{-0.00}$
n_b=0.4±0.1 Gaussian term	174.8±7.6	24.4	0.04±0.01
n_b=0.4(fix) No Gaussian term	174.8±7.6	25.8	—

Table 8.3: The fitted masses, minimized −log(likelihood) values and estimated background fraction α for each fitting condition.

8.7 Likelihood method

We evaluated the top quark mass uncertainty due to the following two sources in likelihood fits.

8.7.1 Different types of likelihood fits

We varied the condition of likelihood fitting to estimate the top quark mass uncertainty due to likelihood fits. The conditions are background unconstrained, background constrained to 0.4±0.1 and background fixed to 0.4. The results are summarized in Table. 8.3. From this result, the uncertainty is less than 0.1 GeV/c^2.

8.7.2 Different ways to fit the points

In a likelihood fitting, if we have Monte Carlo templates at 0.1GeV intervals, this would not be a problem. But templates are limited. So we have to estimate the top quark mass uncertainty due to the fitting function

Parabola	Fitting region	Fitted mass (GeV/c^2)
	160~190	174.8 ± 7.6
	165~190	175.1 ± 7.2
	160~185	175.0 ± 7.9
	165~185	175.2 ± 7.3
	150~200	174.9 ± 8.7
	150~190	174.4 ± 8.2
	160~200	175.2 ± 8.6
Cubic		
	160~190	$175.4^{+7.4}_{-7.8}$
	165~190	$174.8^{+7.2}_{-6.8}$
	160~185	$175.2^{+7.6}_{-7.9}$
	165~185	$173.3^{+7.8}_{-5.9}$
	150~200	$175.8^{+8.6}_{-9.0}$
	150~190	$175.6^{+7.3}_{-7.9}$
	160~200	$174.0^{+8.0}_{-7.3}$

Table 8.4: The fitted regions and fitted masses for parabola fitting and cubic fitting.

and fit regions. Table 8.4 shows the fitted masses for various fitting regions. We tried a parabola and a cubic as a fitting function. From the variation in fitted mass, we estimated the uncertainty to be 0.6 GeV/c^2.

8.8 Monte Carlo statistics

This uncertainty appears in the likelihood fitting. The error of each −log(likelihood) was calculated from the statistical error of signal and background templates. In order to estimate the uncertainty, we fluctuate the distribution of templates by its statistical error. We repeat the mass fitting

1000 times with the CDF data using fluctuated templates. From the r.m.s. of the fitted mass distribution, we estimated the uncertainty to be 1.0 GeV/c^2.

8.9 Total systematic uncertainty

We summarized the systematic uncertainties in top quark mass with the double b-tagged events in Table 8.5.

Systematic Uncertainties	values	
	(GeV/c^2)	(%)
Jet Energy Scale	2.9	1.7
Hard gluon effects	3.6	1.3
Soft gluon effects	1.7	1.0
Different Generators	0.9	0.5
Tagging bias	2.0	1.1
Background spectrum	0.1	<0.1
Likelihood method	0.6	0.3
Monte Carlo statistics	1.0	0.6
Fit configuration	0.9	0.5
total uncertainty	5.6	3.2

Table 8.5: The summary of the systematic uncertainties in top quark mass with the double b-tagged events.

Chapter 9

Kinematic Distributions of Top Quark Production Events

9.1 Purpose

In this chapter, we compare several kinematic quantities which describe $t\bar{t}$ production between the CDF data and Monte Carlo events. This comparison will provide a good check on our reconstruction method and on the $t\bar{t}$ production and decay kinematics predicted by the Standard Model.

9.2 Reconstructed properties

Reconstructed quantities are

1) Invariant mass of $t\bar{t}$	$\mathrm{M}(t\bar{t})$
2) Transverse momentum of $t\bar{t}$ system	$\mathrm{P}_T(t\bar{t})$
3) Transverse momentum of t	$\mathrm{P}_T(\mathrm{top})$
4) $\Delta\phi$ distribution between t and $\bar{t}$	$\Delta\phi(t-\bar{t})$
5) Rapidity distribution of $t\bar{t}$, t	$\mathrm{y}(t\bar{t})$, $\mathrm{y}(\mathrm{top})$
6) Δ rapidity between t and $\bar{t}$	$\Delta\mathrm{y}(t-\bar{t})$

Production of $t\bar{t}$ pairs through non-Standard Model processes should be observable in the $\mathrm{M}(t\bar{t})$, $\mathrm{P}_T(t\bar{t})$ and $\mathrm{P}_T(\mathrm{top})$ distributions. The $\Delta\phi$ and rapidity distributions also provide information about the production and decay process.

We emphasize that all the distributions shown in this chapter are biased by detector resolution, event selection cuts and the reconstruction method. We plot the "observed" variables, not the "true" one. Only the comparison between data and Monte Carlo is of significance.

9.3 Measurement Resolution

We will be mostly concerned with distributions of the true measurement error

$$\varepsilon(X) = X_{\mathrm{meas}} - X_{\mathrm{true}} \tag{9.1}$$

on a variable X which can be any one of the followings:

- top quark P_T, y or ϕ;
- bottom quark P_T or y;
- $t\bar{t}$-system mass, P_T, y, or ϕ, or the $\Delta\phi$ or Δy between the t and the $\bar{t}$.

Since we are dealing with lepton+jets events, it is more natural to talk of a "lepton side" and a "jet side" for each event, rather than a t and a $\bar{t}$ side. By lepton side, we mean the set of decay products from the semileptonically decaying top quark, whereas the jet side contains the decay products of the hadronically decaying top quark. Clearly, it will be necessary to separately study the resolution of kinematical measurements on each side.

In the equation above, the subscript "meas" refers to the MINUIT mass fitter solution with the smallest χ^2. The subscript "true" refers to the generator level value of X, determined at the t or $\bar{t}$ decay vertex.

9.3.1 Analysis techniques

There are several ways of running the mass fitter: with or without b-tags, and with or without constraining the top mass to its measured value. The effect of these constraints is to improve parton-jet matching by the fitter, and therefore also the kinematical measurement resolution. Since there is still a substantial uncertainty on the top mass value, it is important to check our sensitivity to this value when constraining the top mass in the fit. Table 9.1 summarizes the analysis techniques investigated in the present study.

We have used two tagging algorithms: SECVTX and SLT (with fake as well as real tags). When running the mass fitter on tagged events, we require

	Standard fit	Fit with $M_{\rm top}$ constrained to:		
		175 GeV/c^2	165 GeV/c^2	185 GeV/c^2
pretag	$\surd$	$\surd$		
1 or 2 tagged jets	$\surd$	$\surd$	$\surd$	$\surd$
2 tagged jets + M_W cut	$\surd$	$\surd$		

Table 9.1: Possible fitting techniques to measure the kinematical variables which describe $t\bar{t}$ production and decay. The checked boxes ($\surd$) indicate techniques investigated in this thesis.

the tags to be "satisfied": they must be matched to b-partons by the fitter. Thus, for tagged events $X_{\rm meas}$ refers to the MINUIT mass fitter solution with the smallest χ^2 *and* with satisfied tags. Events with three or more tagged jets among the four leading jets can not be satisfied and are not used.

For consistency with the double-tag top quark mass analysis of Chapter 7 we require that the invariant mass of the two untagged jets in double-tag events be between 60 and 100 GeV/c^2. This cut is made after correcting the untagged jet energies but prior to the top quark mass fit itself. The double-tag results shown in all tables and figures of this thesis include the W mass cut.

In order to be able to distinguish parton-jet assignment mistakes made by the fitter from other resolution-smearing effects, we also analyzed the following two subsets of events:

1. Subset A: Events where the fitter correctly identifies the b-jet on the lepton side, regardless of what happens on the jet side. For such events, the top and bottom quark momenta on the lepton side should be almost

as well reconstructed as in the rarer case where *all* the parton-jet assignments are correctly made. However, it should be kept in mind that even if parton-jet assignment mistakes are made on the jet side only, the missing momentum determination will be affected, and therefore also measurements made on the lepton side.

2. Subset B: Events where the fitter correctly makes *all* the parton-jet assignments. Note that this event selection has a physical bias, since it implies that there is no gluon jet among the four leading jets.

To determine whether the parton-jet assignments made by the fitter are correct or not, we need a procedure to match reconstructed jets with generator-level partons. This is done as follows. For each parton, we start by finding the nearest jet in (η, ϕ)-space, using the standard distance measure $\Delta R = \sqrt{\Delta\eta^2 + \Delta\phi^2}$. We then call the match successful if $\Delta R \leq 0.4$.

9.3.2 Measurement resolution

When the distribution of the true measurement error $\varepsilon(X)$ on a quantity X is Gaussian and centered at zero, the resolution is simply defined as the R.M.S. deviation of that distribution. Unfortunately, as we will show in the next section, top kinematical variables have error distributions with non-Gaussian tails, asymmetric shapes and non-zero modes. It is not possible to summarize such distributions by a single number such as their R.M.S. deviation. However, for the purpose of comparing analysis techniques, it is convenient to represent the resolution by a single number:

We define the resolution $r(X)$ of a quantity X to be such that 68% of the measurements of X have a true error $|\varepsilon(X)| = |X_{\text{meas}} - X_{\text{true}}| \leq r(X)$.

For Gaussian error distributions centered at zero, this definition coincides with the R.M.S. deviation.

9.3.3 Results

Characteristics of events processed by the mass fitter

Table 9.2 shows some properties of events processed by the mass fitter. The success of a mass fit is usually decided by looking at the fit χ^2, which is required to be less than 10. As expected, the efficiency of this cut decreases as more and more constraints are put on the fit. If no W mass cut is applied on the double-tag events, the efficiency of the χ^2 cut is 71.2% and 62.2% for the unconstrained and constrained double-tag analyses respectively. The W mass cut and the χ^2 cut are clearly correlated. The fraction of events with a true e/μ+jets topology at the generator level is approximately 91%, independently of the fitting technique. The table also shows how various constraints can improve the parton-jet assignments made by the fitter.

Since the top quark mass is currently known to about 10 GeV/c^2, it is important to check how the numbers in Table 9.2 change when one constrains the fit to a top quark mass value which is wrong by $\pm$ one standard deviation. This is shown in Table 9.3. From looking at the parton-jet assignment efficiencies, it is clear that constraining improves the fit, even if the top quark mass value is off by one standard deviation.

Overall measurement resolutions

Figures 9.1 through 9.8 present distributions of the true measurement error on various top kinematical variables calculated with the fitter. For each variable we show two plots, one for the pretag sample, and one for the double-tag sample where the fit is constrained to the correct top quark mass. This brackets parton-jet assignment efficiencies realistically achievable with current analysis techniques. The dashed lines in these figures are distributions one would obtain if the parton-jet assignments where correctly made by the fitter. Table 9.4 summarizes the resolutions for several analysis techniques.

For a comparison, we show in Table 9.5 the resolutions obtained from event subsets A and B defined in Section 9.3.1. With two exceptions, the resolutions in this table are insensitive to the constraints applied on the fit, demonstrating that the various analysis techniques discussed so far only affect the parton-jet matching efficiency, and not so much other sources of resolution smearing, such as jet energy scale and neutrino momentum reconstruction. The two exceptions are the $t\bar{t}$ invariant mass and the b transverse momentum on the jet side. In both cases, adding the top quark mass constraint to the fit improves the resolution by a factor of two.

Finally, we show in Table 9.6 the effect on resolutions of constraining to the wrong top quark mass value. Here again, it appears that even if one constrains the fit to a top quark mass value that is wrong by $\pm$ one standard deviation, the resolution improves with respect to the unconstrained fit.

Resolution functions

In this section we investigate how the measurement resolution of a variable X depends on the value of X. We only look at the pretag sample, without constraining the top mass in the fitter.

As the first example we consider the invariant mass of the $t\bar{t}$ system. Figure 9.10(a) shows a V-shaped dependence of the M($t\bar{t}$) resolution on the value of M($t\bar{t}$). This shape is easily understood by looking at a scatter plot of the true error ΔM on the $t\bar{t}$ invariant mass, versus M (Fig. 9.10(b)). The sharp edge on this plot corresponds to the line $\Delta M = M - 350$ GeV/c^2. All the points lie below this line since the true $t\bar{t}$ invariant mass must be larger than 350 GeV/c^2 when $M_{\rm top} = 175$ GeV/c^2. When plot (b) is folded over itself to give $|\Delta M|$ versus M, plot (c) results. The shape of plot (a) is a direct consequence of the distribution of the points in plot (c).

The second example is the transverse momentum P_T of the jet-side top quark. Figure 9.11 has the same layout as Fig. 9.10. The sharp edge in plot (b) corresponds to the boundary $P_{T\rm true} \geq 0$. Plot (d) shows the same as plot (b) for events in which all parton-jet assignments were correctly made by the fitter. Clearly, for such events the resolution will be much flatter as a function of P_T.

Our third and last example is the rapidity of the lepton-side top quark (Fig. 9.12). Here, mismeasurement of the z-component of the neutrino momentum is responsible for the bad resolution at large top quark rapidity. Plot 9.12(d) shows the relative error on the z-component of the reconstructed neutrino momentum. The fitter reconstructs this quantity by constraining

the invariant mass of the lepton and the neutrino to the nominal W-boson mass. This is a quadratic constraint, yielding two possible solutions for the neutrino P_Z. In the plot, the peak at 0.0 corresponds to the correct solution, whereas the peak just above 1.0 corresponds to the wrong solution. When one selects events around the correct solution, the rapidity y of the lepton-side top quark is much flatter as a function of y. This is shown by the white circles in plot (a).

Figures 9.13 to 9.15 show several other resolution functions calculated from the pretag sample without the top quark mass constraint in the fitter.

9.3.4 Conclusions on measurement resolution

Using the standard HERWIG $t\bar{t}$ sample, we have estimated the measurement resolution of several kinematical parameters which characterize $t\bar{t}$ production and decay.

There are two independent methods for improving parton-jet matching by the fitter and hence kinematical resolutions. The first method is to use tagged events and to force the fitter to assign the tagged jets to b-partons. The second method is to constrain the top quark mass to its measured value when fitting $t\bar{t}$ candidate events. Even if the measured top quark mass is one standard deviation away from the true top quark mass, this second method improves the resolutions.

So far we have not looked at background events. While it makes no sense to speak of the top quark momentum resolution in background events, the latter will smear the kinematical distributions of the $t\bar{t}$ candidate events.

This needs to be studied before any attempt can be made at unfolding these distributions.

There may be other ways to improve the resolutions. For example, the current mass fitter only uses the four leading jets of the event it reconstructs. Since it sometimes happens that one of these jets comes from a gluon rather than from a top quark decay product, it may make sense to try and include jets beyond the leading four in the fit, if some way is found to reduce the resulting combinatoric smearing. Also, we have not yet studied the effect of the χ^2 cut on resolution. A tighter χ^2 cut might improve parton-jet matching. Finally, there may be some variables which do not benefit from the fitting procedure. Consider the b-jet transverse momentum for example. We may be better off studying the P_T spectrum of tagged jets in the sample of $t\bar{t}$ candidates, rather than a spectrum obtained with the fitter.

	pretag (%)	pretag +constr. (%)	1-tag (%)	1-tag +constr. (%)	2-tag (%)	2-tag +constr. (%)
$60 \leq M_W(jj) \leq 100$ GeV/c^2					60.3	60.3
$\chi^2 \leq 10$	96.3	87.6	84.5	75.2	96.0	88.0
e/μ+jets topology	90.7	91.0	90.8	91.1	91.9	91.9
correct lepton side $b-$jet assignment	43.3	50.6	52.2	61.0	66.7	76.0
all parton-jet assignments correct	20.8	28.1	31.4	41.0	50.9	61.6

Table 9.2: Characteristics of events processed by the mass fitter, for various analysis techniques. Columns marked "+ constr." are for fits where the top mass was constrained to its nominal value of 175 GeV/c^2. The second row shows the efficiency of the W mass cut for the double-tag analyses. The third row then gives the efficiency of the χ^2 cut. For the "2-tag" columns, this is the efficiency after the W mass cut. For events remaining after the M_W and χ^2 cuts, the fourth row shows the percentage of events with a true e or μ + jets topology at the generator level. Then, for this subset of events which pass the M_W and χ^2 cuts, and have a true e/μ+jets topology, row 5 gives the percentage for which the lepton-side b-jet was correctly identified, whereas row 6 shows the percentage with *all* parton-jet assignments correct.

	1-tag	1-tag & M_{top} constrained to:		
	(%)	175 GeV/c^2 (%)	165 GeV/c^2 (%)	185 GeV/c^2 (%)
$\chi^2 \leq 10$	84.5	75.2	76.3	71.2
e/μ+jets topology	90.8	91.1	91.3	91.2
correct lepton side $b-$jet assignment	52.2	61.0	62.3	56.8
all parton-jet assignments correct	31.4	41.0	39.9	38.5

Table 9.3: Effect of constraining the fit to the wrong top mass. The rows in this table have the same meaning as in table 9.2.

Quantity		pretag	pretag +constr.	1-tag	1-tag +constr.	2-tag	2-tag +constr.
P_T(lepton side t)	(GeV/c)	35.8	28.8	31.3	24.2	23.9	18.7
P_T(jet side t)	(GeV/c)	34.4	27.7	30.8	23.5	23.2	17.2
$P_T(t\bar{t})$	(GeV/c)	16.2	15.4	15.3	14.6	13.3	13.0
y(lepton side t)		0.42	0.37	0.37	0.32	0.29	0.25
y(jet side t)		0.25	0.19	0.20	0.14	0.11	0.08
$y(t\bar{t})$		0.18	0.17	0.16	0.15	0.13	0.12
ϕ(lepton side t)	(degrees)	44.4	36.4	36.1	25.7	20.2	14.1
ϕ(jet side t)	(degrees)	43.8	35.5	36.0	24.9	19.3	12.0
$\phi(t\bar{t})$	(degrees)	93.9	92.8	91.0	89.8	85.7	87.3
Mass($t\bar{t}$)	(GeV/c^2)	56.0	36.9	49.3	31.6	41.4	23.6
$\Delta y(t,\bar{t})$		0.40	0.35	0.36	0.30	0.29	0.24
$\Delta\phi(t,\bar{t})$	(degrees)	10.6	10.8	9.6	9.2	7.4	7.1
P_T(lepton side b)	(GeV/c)	19.7	16.6	17.1	13.8	13.4	10.9
P_T(jet side b)	(GeV/c)	27.6	23.1	21.0	16.7	14.8	10.0
y(lepton side b)		0.74	0.56	0.53	0.32	0.18	0.09
y(jet side b)		0.87	0.76	0.56	0.33	0.20	0.09

Table 9.4: Measurement resolutions of top kinematic variables in pretag, single-tag, and double-tag samples of $t\bar{t}$ events ($M_{\rm top} = 175\ GeV/c^2$), with and without constraining the top mass to 175 GeV/c^2 in the fit.

Quantity			pretag	pretag +constr.	1-tag	1-tag +constr.	2-tag	2-tag +constr.
P_T(lepton side t)	(GeV/c)	$\star$	16.7	15.0	15.9	14.7	15.0	14.2
P_T(jet side t)	(GeV/c)	†	10.6	8.9	10.9	9.4	10.9	9.5
$P_T(t\bar{t})$	(GeV/c)	†	10.9	11.0	11.1	11.2	11.2	11.1
y(lepton side t)		$\star$	0.21	0.18	0.20	0.17	0.19	0.18
y(jet side t)		†	0.05	0.04	0.04	0.04	0.04	0.04
$y(t\bar{t})$		†	0.09	0.08	0.09	0.09	0.09	0.09
ϕ(lepton side t)	(degrees)	$\star$	8.0	8.1	8.2	8.2	7.4	7.7
ϕ(jet side t)	(degrees)	†	5.2	4.8	5.5	5.3	4.7	4.9
$\phi(t\bar{t})$	(degrees)	†	76.2	75.7	74.9	74.8	76.8	77.8
Mass$(t\bar{t})$	(GeV/c^2)	†	32.3	15.4	33.2	15.0	33.2	14.8
$\Delta y(t,\bar{t})$		†	0.17	0.16	0.16	0.16	0.17	0.16
$\Delta\phi(t,\bar{t})$	(degrees)	†	4.8	4.8	4.9	4.9	5.1	4.9
P_T(lepton side b)	(GeV/c)	$\star$	10.7	8.7	10.5	8.5	9.9	8.3
P_T(jet side b)	(GeV/c)	†	9.0	4.7	9.2	5.2	9.2	5.3
y(lepton side b)		$\star$	0.05	0.05	0.05	0.05	0.04	0.04
y(jet side b)		†	0.05	0.05	0.04	0.04	0.04	0.04

Table 9.5: Measurement resolutions of top kinematic variables, without the smearing due to parton-jet assignment mistakes. Rows with a star were calculated from a subset of events where the lepton-side b-jet is correctly assigned by the fitter. Rows with a dagger were calculated from a subset of events where all parton-jet assignments are correctly made by the fitter.

Quantity		1-tag	1-tag & M_{top} constrained to:		
			175 GeV/c^2	165 GeV/c^2	185 GeV/c^2
P_T(lepton side t)	(GeV/c)	31.3	24.2	26.2	26.7
P_T(jet side t)	(GeV/c)	30.8	23.5	22.8	28.0
$P_T(t\bar{t})$	(GeV/c)	15.3	14.6	15.0	14.4
y(lepton side t)		0.37	0.32	0.30	0.37
y(jet side t)		0.20	0.14	0.14	0.17
$y(t\bar{t})$		0.16	0.15	0.15	0.17
ϕ(lepton side t)	(degrees)	36.1	25.7	23.4	31.7
ϕ(jet side t)	(degrees)	36.0	24.9	23.5	30.8
$\phi(t\bar{t})$	(degrees)	91.0	89.8	90.4	90.2
Mass($t\bar{t}$)	(GeV/c^2)	49.3	31.6	40.1	40.2
$\Delta y(t,\bar{t})$		0.36	0.30	0.30	0.34
$\Delta\phi(t,\bar{t})$	(degrees)	9.6	9.2	9.4	9.5
P_T(lepton side b)	(GeV/c)	17.1	13.8	14.2	15.6
P_T(jet side b)	(GeV/c)	21.0	16.7	18.1	20.2
y(lepton side b)		0.53	0.32	0.28	0.42
y(jet side b)		0.56	0.33	0.35	0.43

Table 9.6: Effect on resolution of constraining the kinematical fit to the wrong top mass. Columns 2 & 3 in this table are identical to columns 4 & 5 in Table 9.4. The last two columns show the resolutions obtained when constraining to a top mass value that is one standard deviation away from the nominal value.

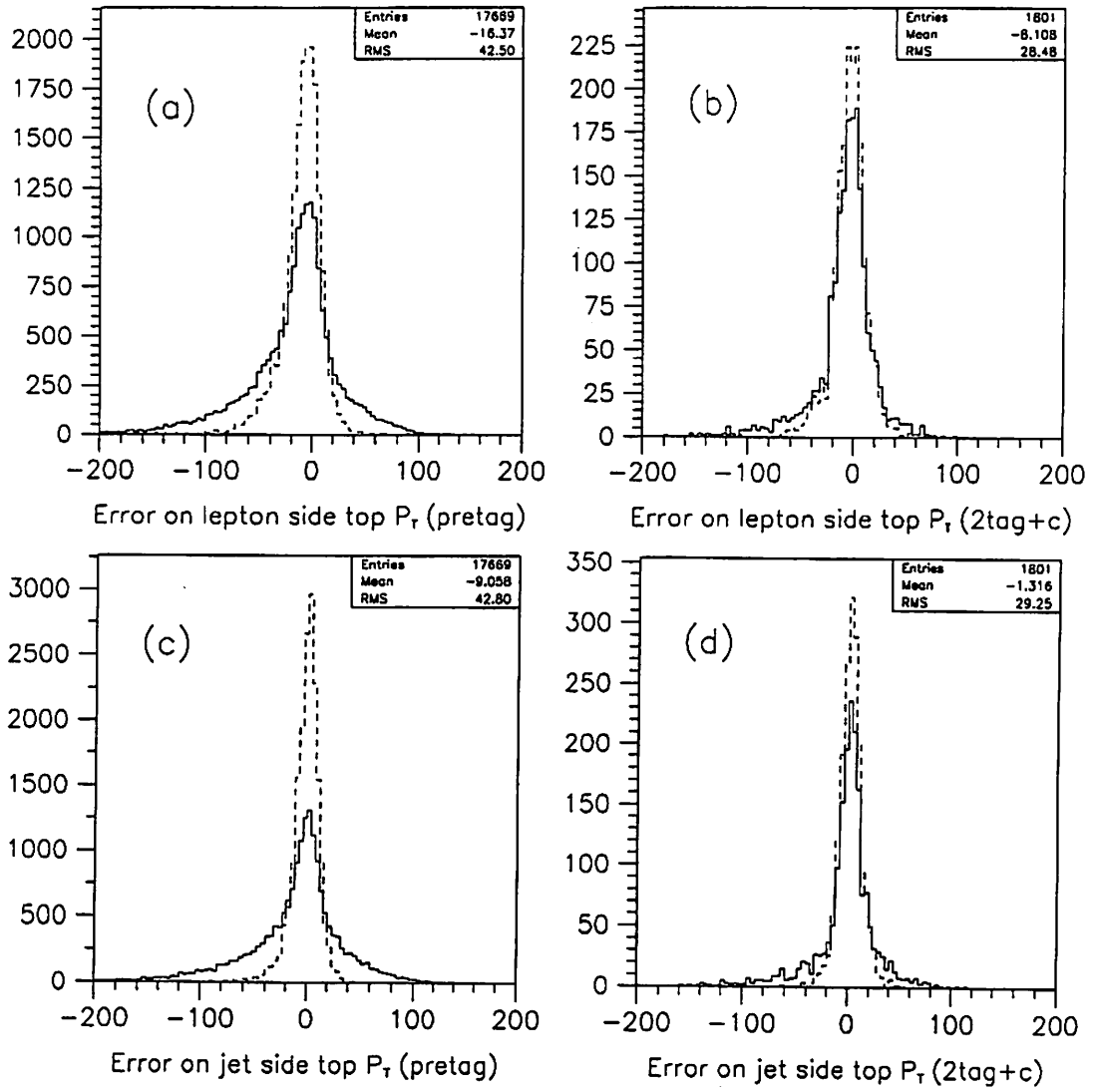

Figure 9.1: Measurement error on the top quark transverse momentum for (a) lepton side in the pretag sample, (b) lepton side in the double-tag sample with mass constraint, (c) jet side in the pretag sample, and (d) jet side in the double-tag sample with mass constraint. The dashed lines show the corresponding distributions for events in which the b-jet is correctly identified on the lepton side (plots (a) and (b)), and for events in which all parton-jet assignments are correctly made by the fitter (plots (c) and (d)). In all plots, the dashed histograms are normalized to the same area as the solid ones.

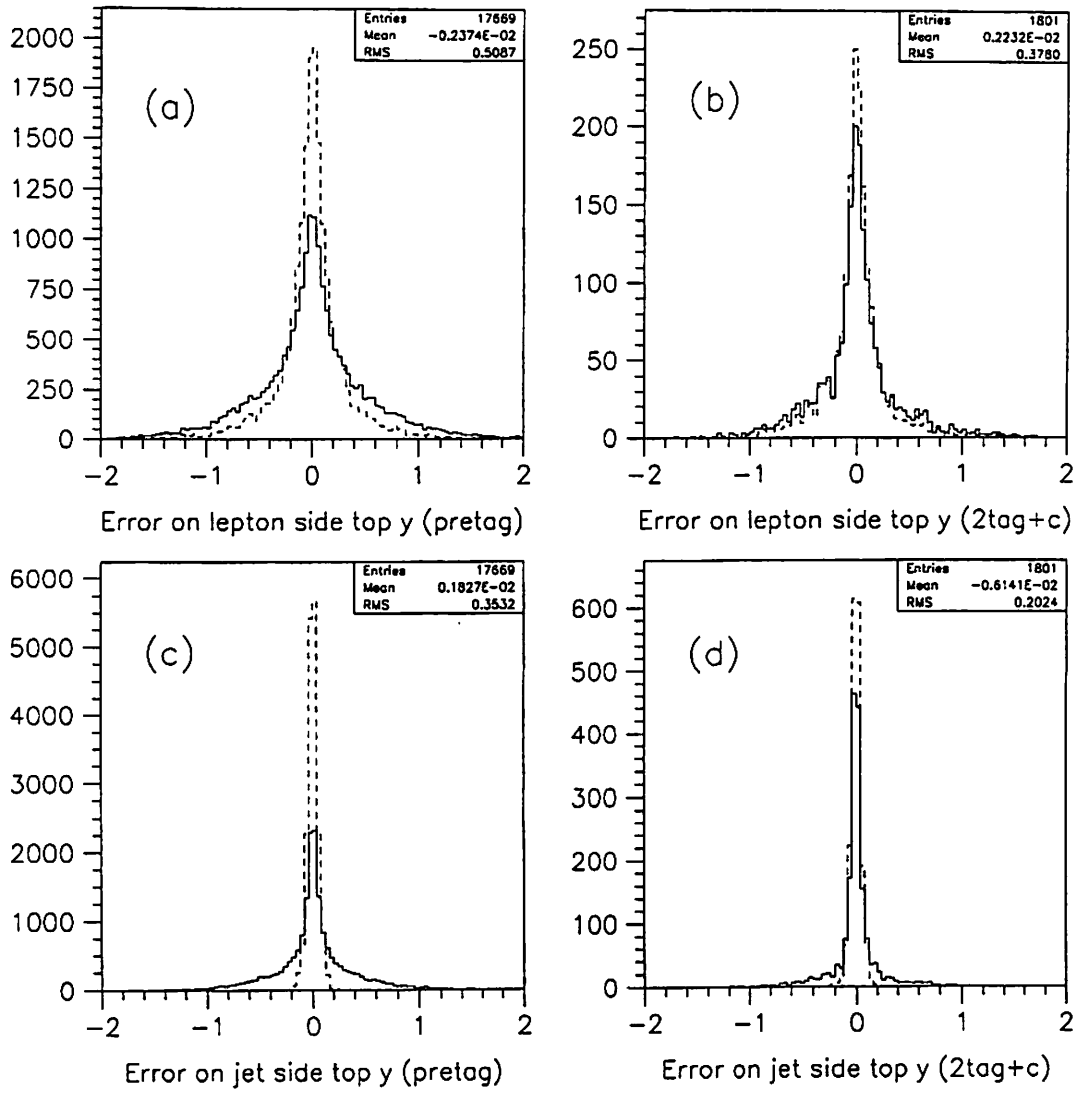

Figure 9.2: Measurement error on the top quark rapidity for (a) lepton side in the pretag sample, (b) lepton side in the double-tag sample with mass constraint, (c) jet side in the pretag sample, and (d) jet side in the double-tag sample with mass constraint. The dashed lines show the corresponding distributions for events in which the b-jet is correctly identified on the lepton side (plots (a) and (b)), and for events in which all parton-jet assignments are correctly made by the fitter (plots (c) and (d)). In all plots, the dashed histograms are normalized to the same area as the solid ones.

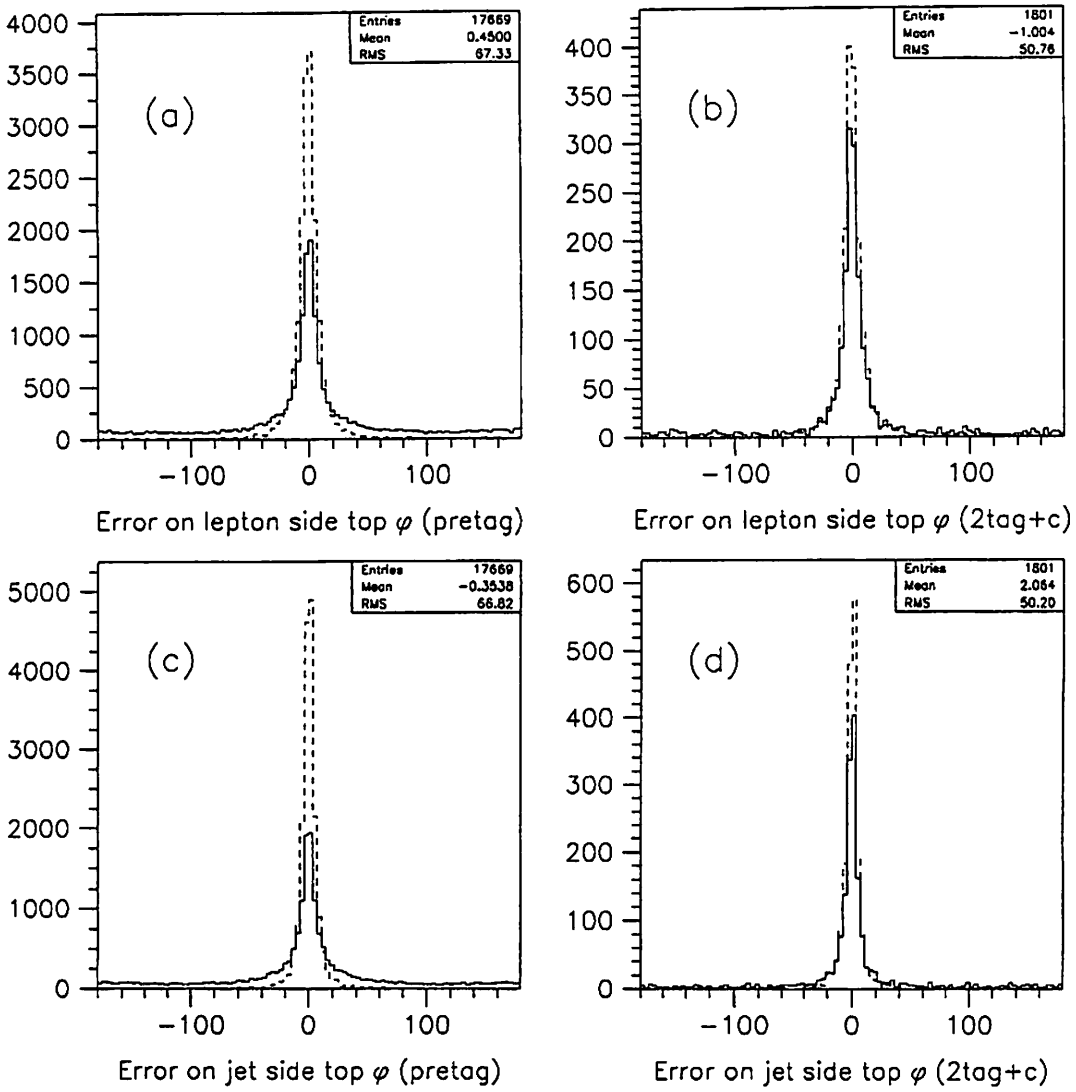

Figure 9.3: Measurement error on the top quark azimuth for (a) lepton side in the pretag sample, (b) lepton side in the double-tag sample with mass constraint, (c) jet side in the pretag sample, and (d) jet side in the double-tag sample with mass constraint. The dashed lines show the corresponding distributions for events in which the b-jet is correctly identified on the lepton side (plots (a) and (b)), and for events in which all parton-jet assignments are correctly made by the fitter (plots (c) and (d)). In all plots, the dashed histograms are normalized to the same area as the solid ones.

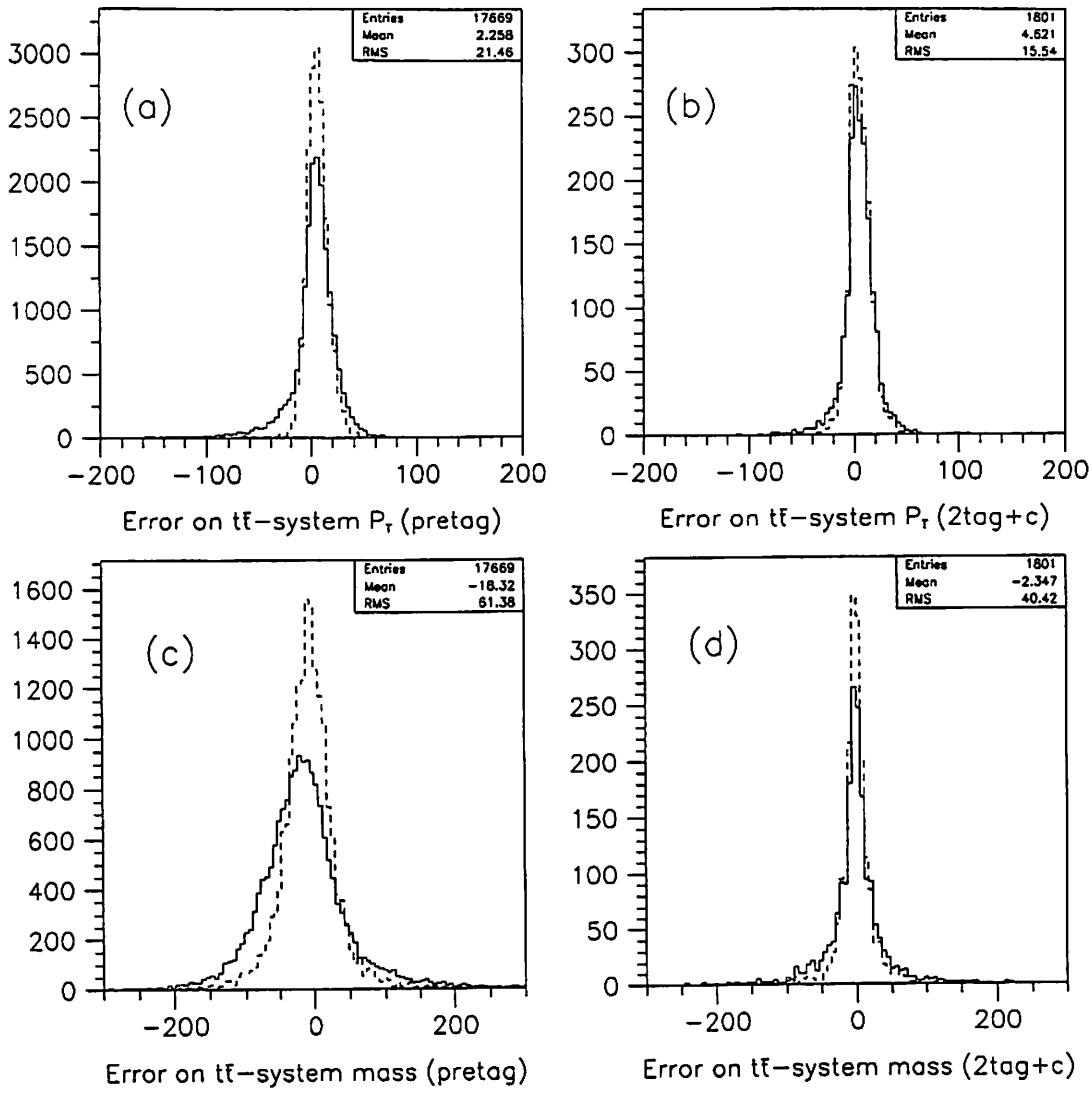

Figure 9.4: Measurement error on the $t\bar{t}$ system transverse momentum (plots (a) and (b)) and invariant mass (plots (c) and (d)). The left-hand side plots are for the pretag sample, whereas the right-hand side plots are for the double-tag sample, with top mass constraint used in the fit. The dashed lines show the corresponding distributions for events in which all parton-jet assignments are correctly made by the fitter. The dashed histograms are normalized to the same area as the solid ones.

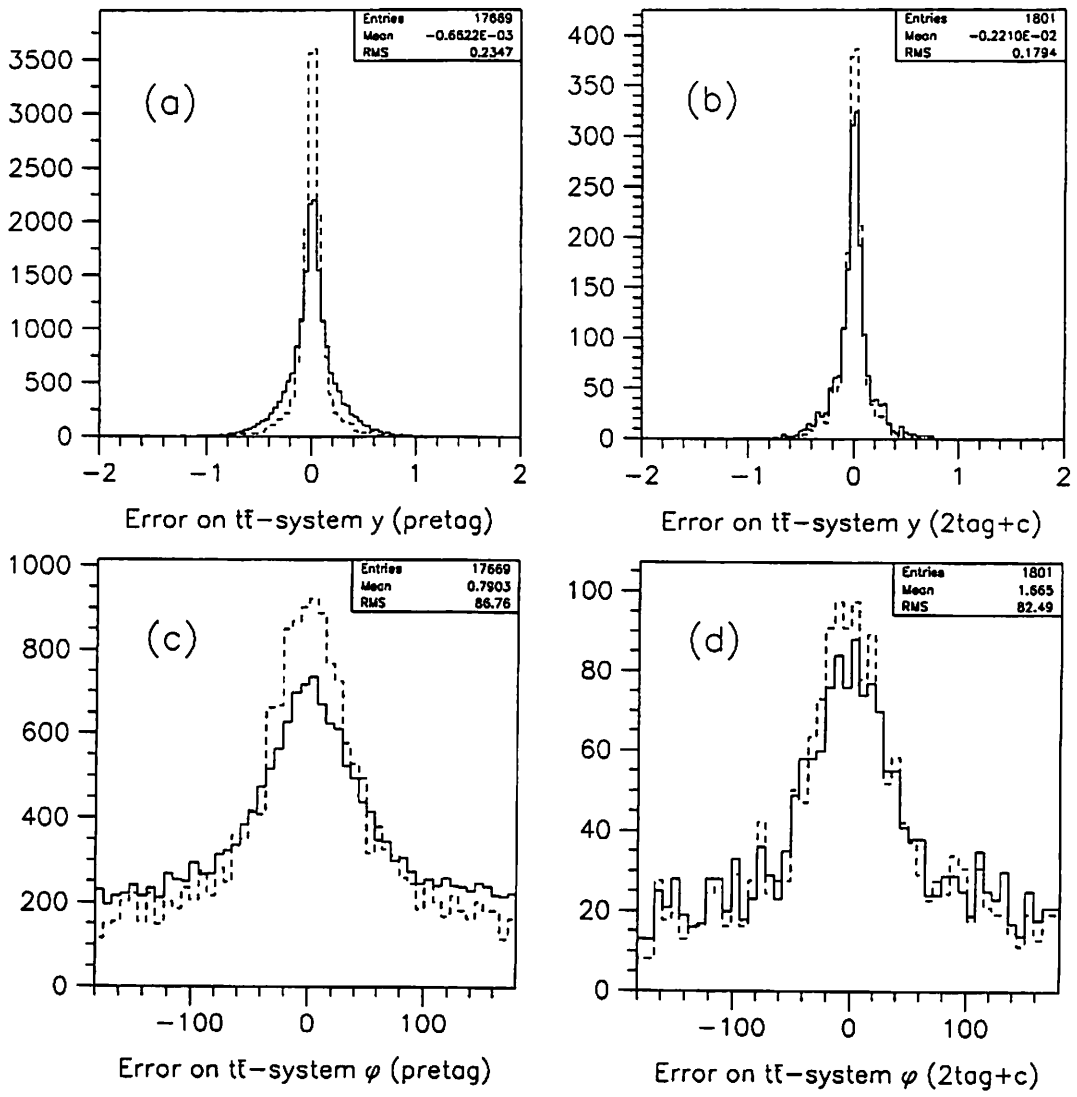

Figure 9.5: Measurement error on the $t\bar{t}$ system rapidity (plots (a) and (b)) and azimuth (plots (c) and (d)). The left-hand side plots are for the pretag sample, whereas the right-hand side plots are for the double-tag sample, with top mass constraint used in the fit. The dashed lines show the corresponding distributions for events in which all parton-jet assignments are correctly made by the fitter. The dashed histograms are normalized to the same area as the solid ones.

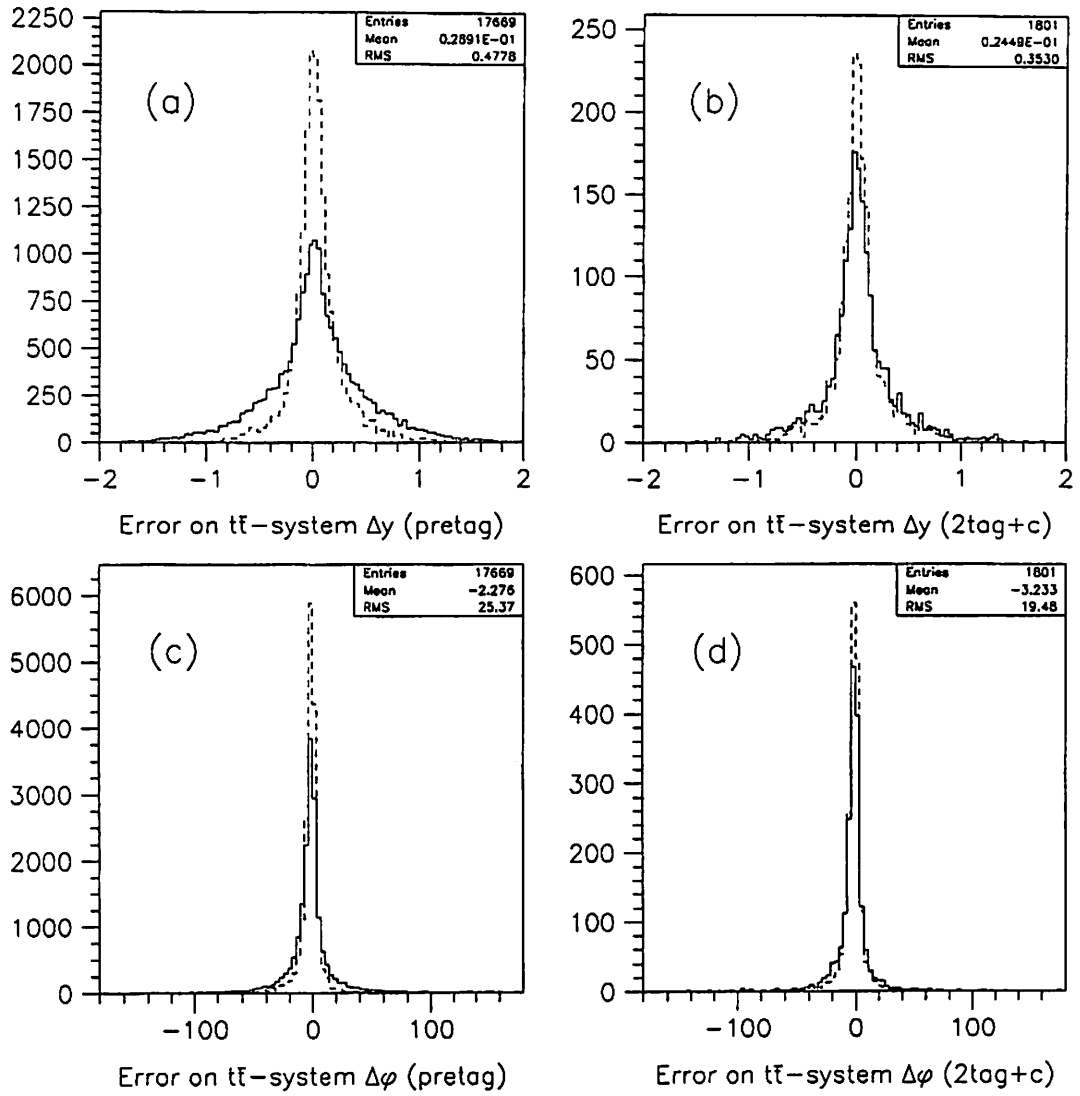

Figure 9.6: Measurement error on the rapidity difference (plots (a) and (b)) and the azimuthal separation (plots (c) and (d)) between the top and antitop. The left-hand side plots are for the pretag sample, whereas the right-hand side plots are for the double-tag sample, with top mass constraint used in the fit. The dashed lines show the corresponding distributions for events in which all parton-jet assignments are correctly made by the fitter. The dashed histograms are normalized to the same area as the solid ones.

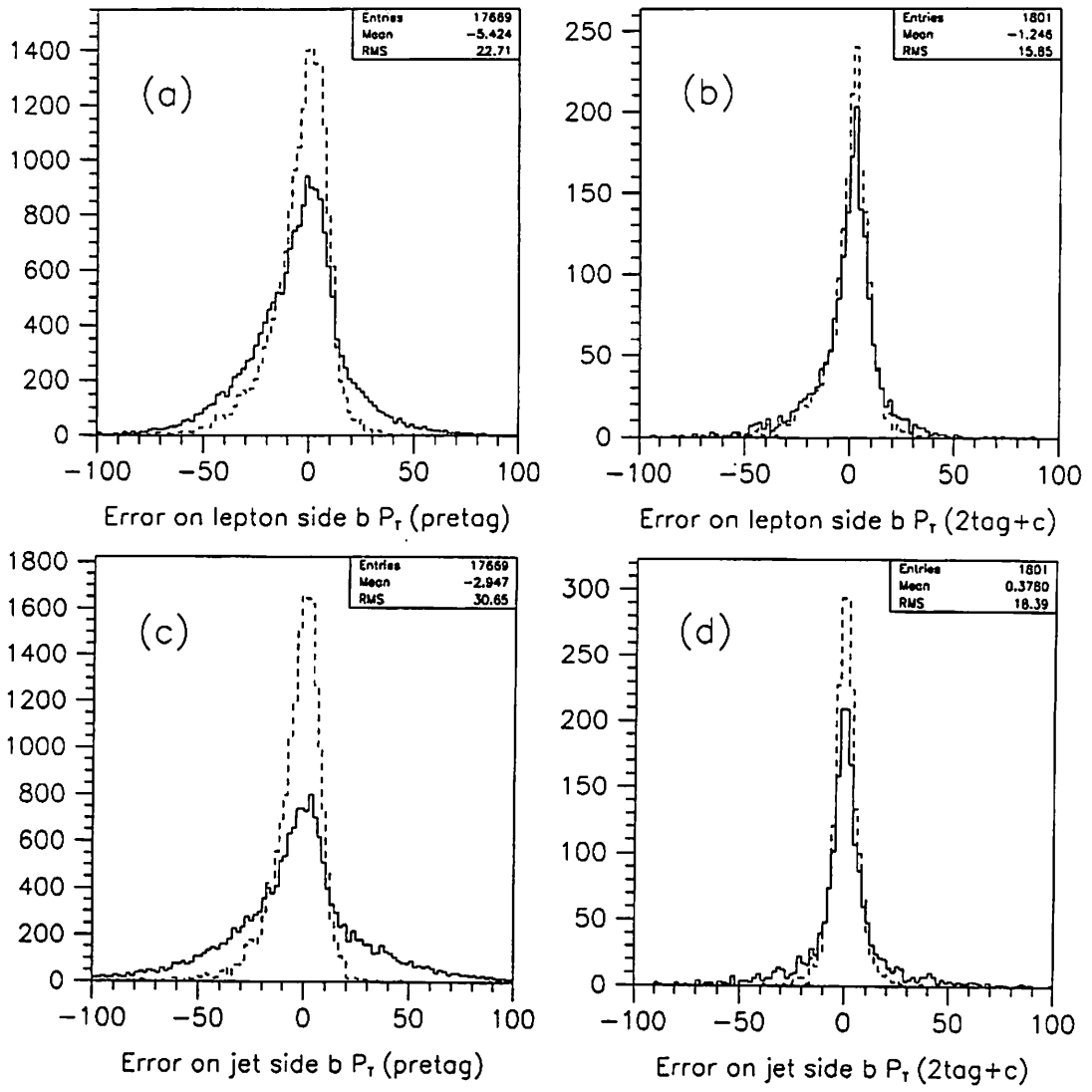

Figure 9.7: Measurement error on the bottom quark transverse momentum for (a) lepton side in the pretag sample, (b) lepton side in the double-tag sample with mass constraint, (c) jet side in the pretag sample, and (d) jet side in the double-tag sample with mass constraint. The dashed lines show the corresponding distributions for events in which the b-jet is correctly identified on the lepton side (plots (a) and (b)), and for events in which all parton-jet assignments are correctly made by the fitter (plots (c) and (d)). In all plots, the dashed histograms are normalized to the same area as the solid ones.

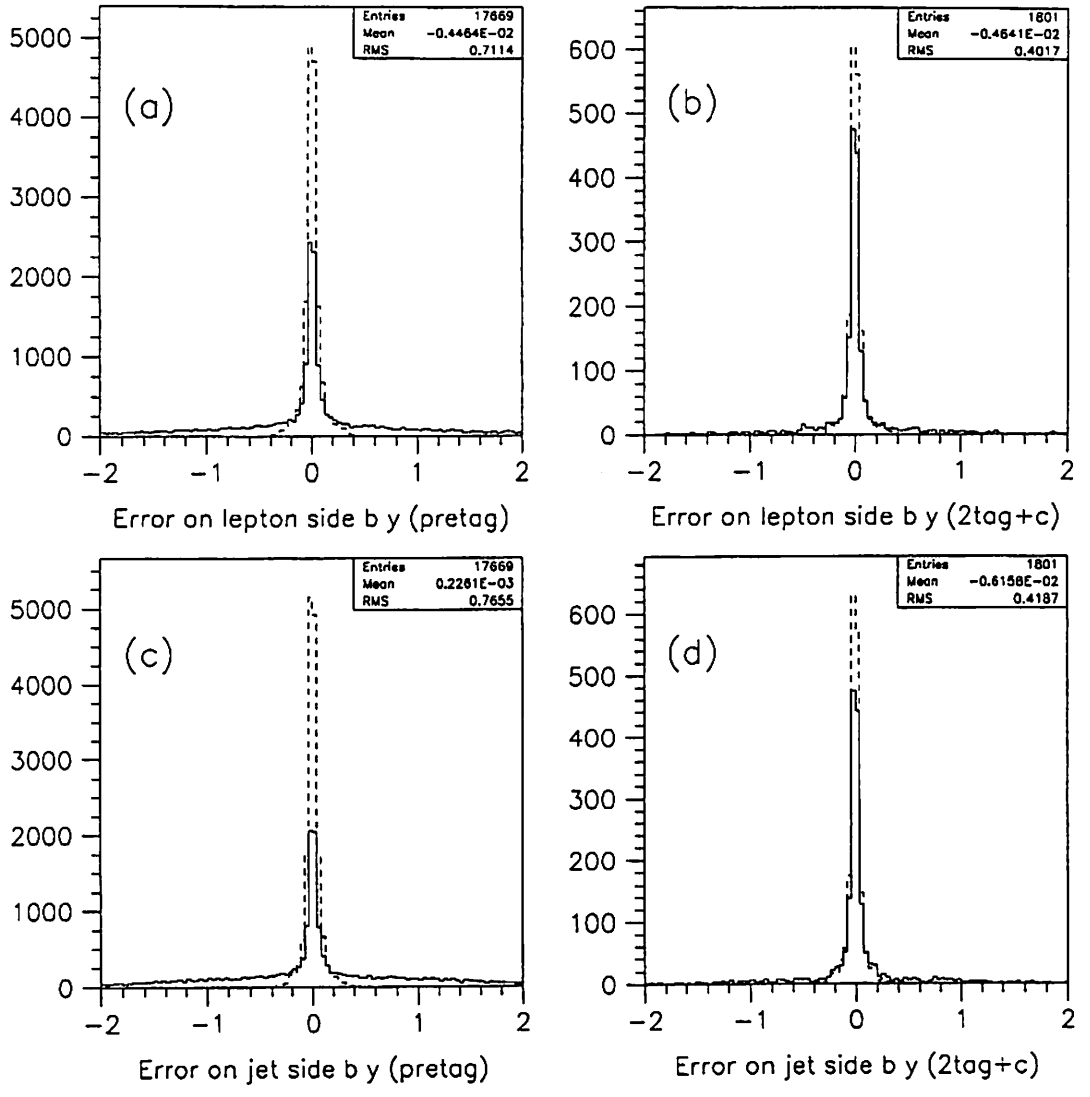

Figure 9.8: Measurement error on the bottom quark rapidity for (a) lepton side in the pretag sample, (b) lepton side in the double-tag sample with mass constraint, (c) jet side in the pretag sample, and (d) jet side in the double-tag sample with mass constraint. The dashed lines show the corresponding distributions for events in which the b-jet is correctly identified on the lepton side (plots (a) and (b)), and for events in which all parton-jet assignments are correctly made by the fitter (plots (c) and (d)). In all plots, the dashed histograms are normalized to the same area as the solid ones.

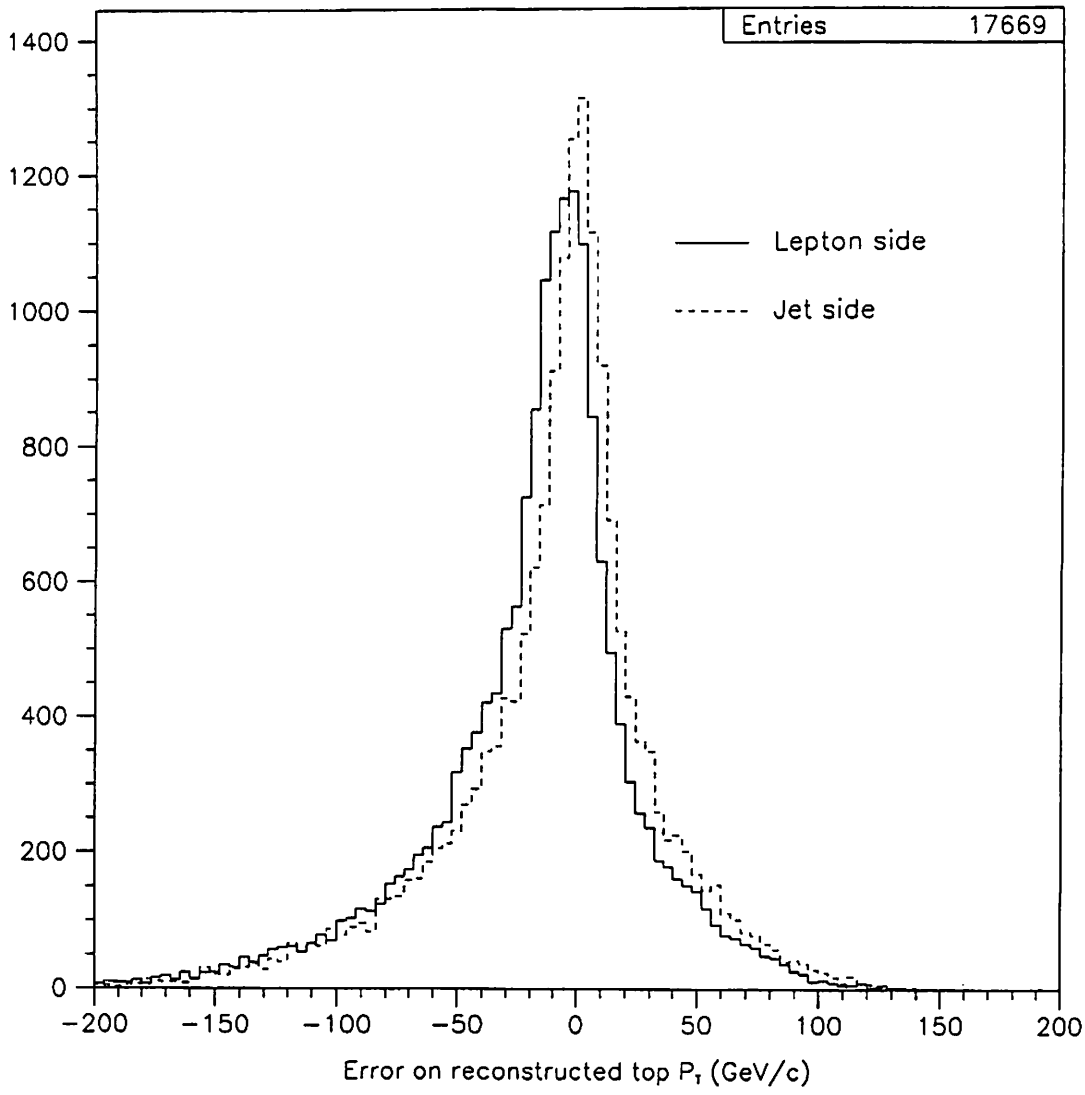

Figure 9.9: Measurement error on the top quark transverse momentum for the pretag sample without top mass constraint. The solid line shows the lepton side distribution, the dashed line the jet side distribution.

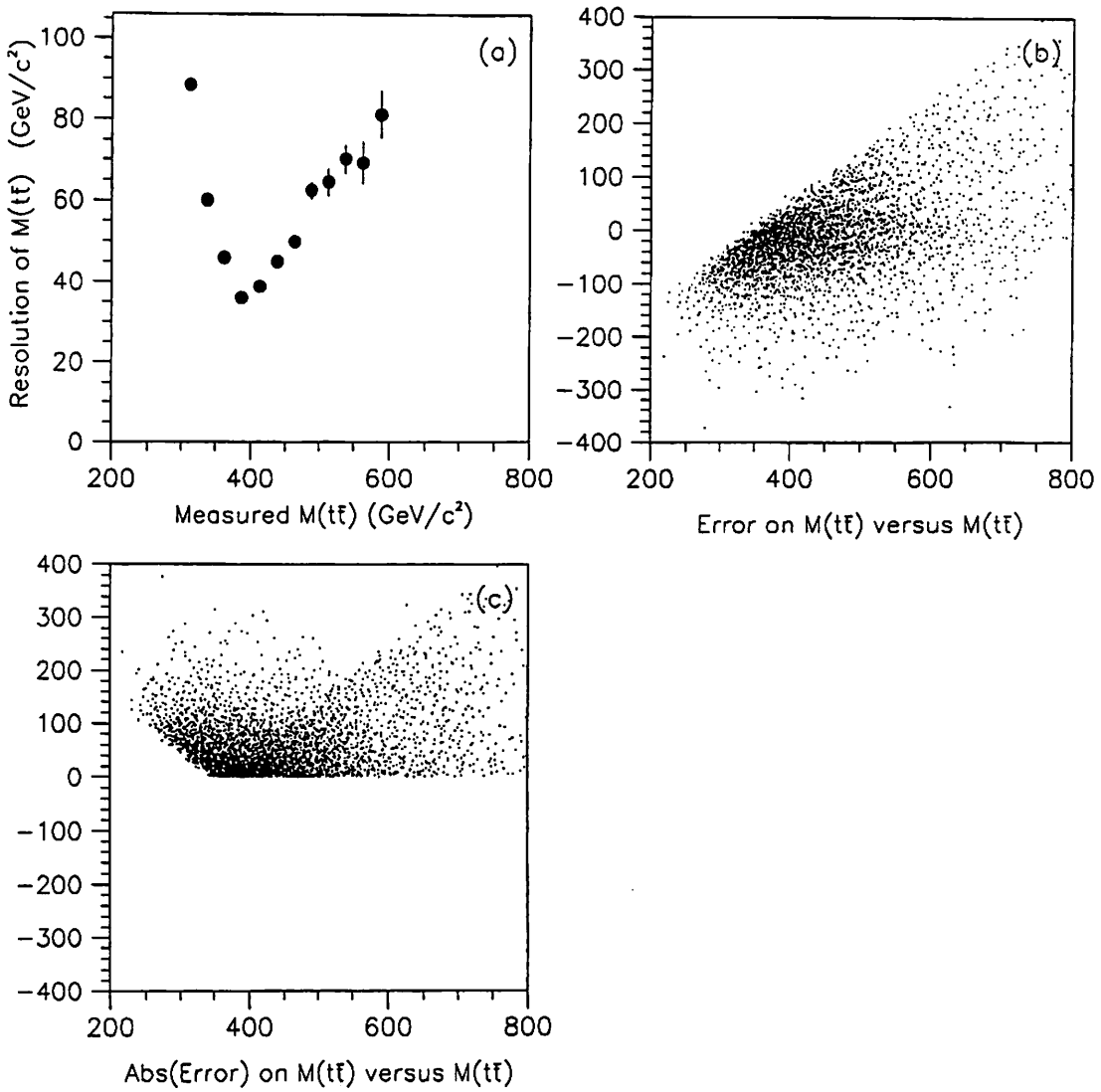

Figure 9.10: Plot (a) shows the measurement resolution of the $t\bar{t}$ invariant mass M as a function of M. Plot (b) is a scatter plot of the true error on M versus M, and plot (c) is a scatter plot of the absolute value of the true error on M versus M. All units are GeV/c^2. All plots were made from the pretag sample without constraining the top mass in the fitter.

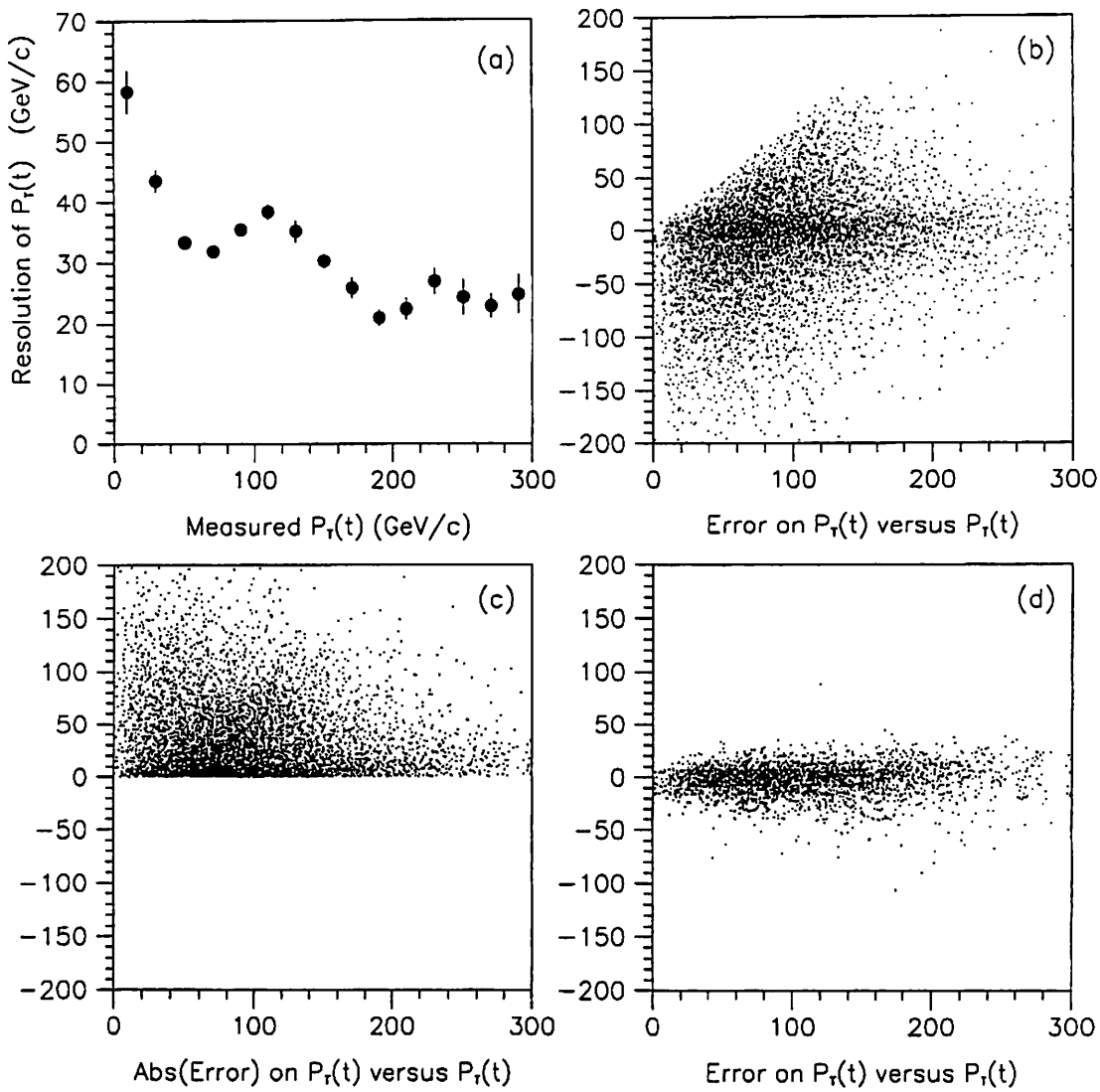

Figure 9.11: Plot (a) shows the measurement resolution of the jet-side top transverse momentum P_T as a function of P_T. Plot (b) is a scatter plot of the true error on P_T versus P_T, and plot (c) is a scatter plot of the absolute value of the true error on P_T versus P_T. Plot (d) is the same as plot (b), but only for events for which the fitter correctly guessed all the parton-jet assignments. All units are GeV/c. All plots were made from the pretag sample without constraining the top mass in the fitter.

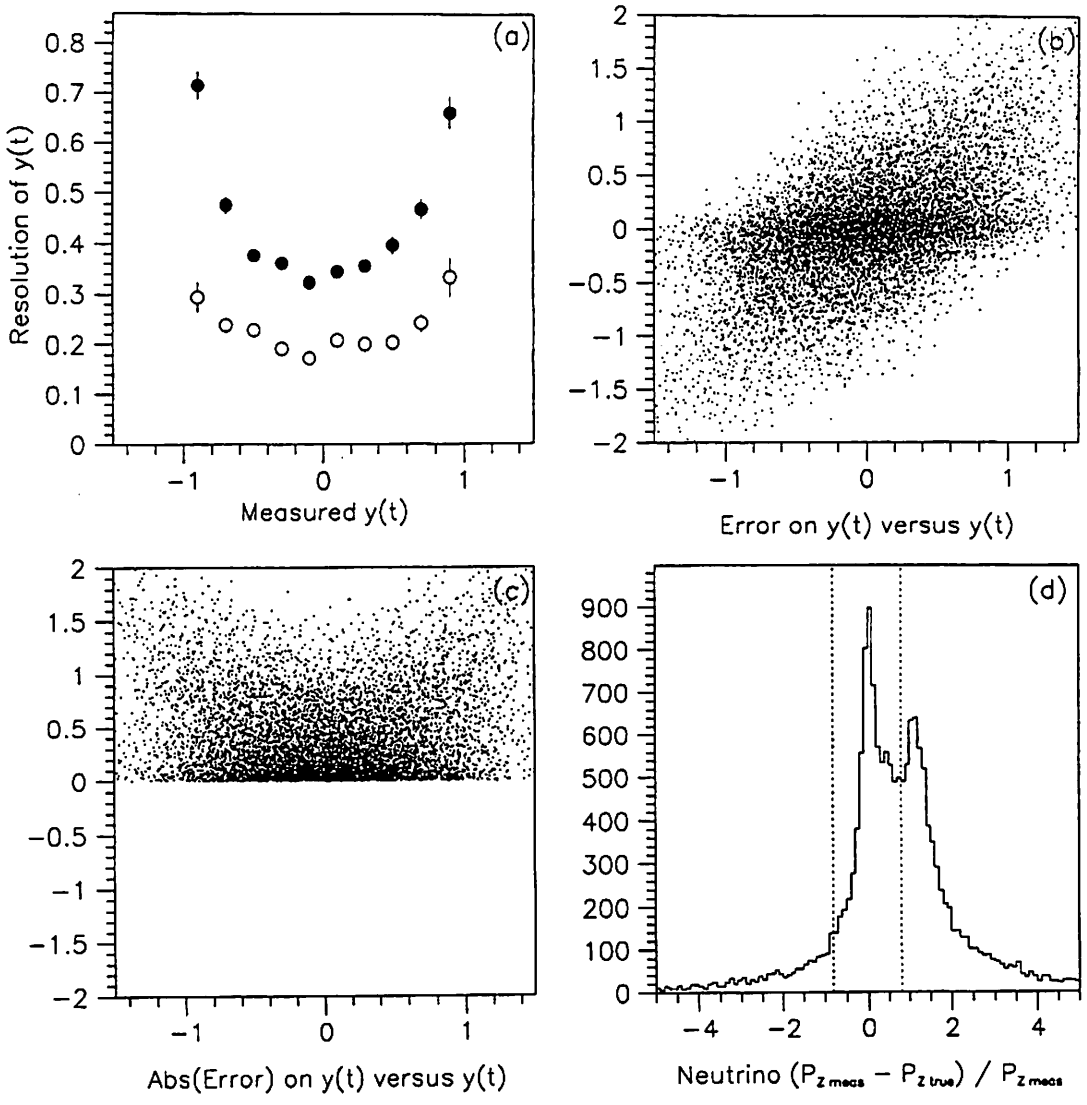

Figure 9.12: Plot (a) shows the measurement resolution of the lepton-side top rapidity y as a function of y for all pretag events (black cicles), and for events for which the reconstructed neutrino momentum passes the cut $|\Delta P_Z/P_Z| \leq 0.8|$ (white circles). Plot (b) is a scatter plot of the true error on y versus y, and plot (c) is a scatter plot of the absolute value of the true error on y versus y. Plot (d) show the relative error on the reconstructed neutrino P_Z. The dotted lines mark the cut used to plot the white circles in plot (a). All plots were made from the pretag sample without constraining the top mass in the fitter.

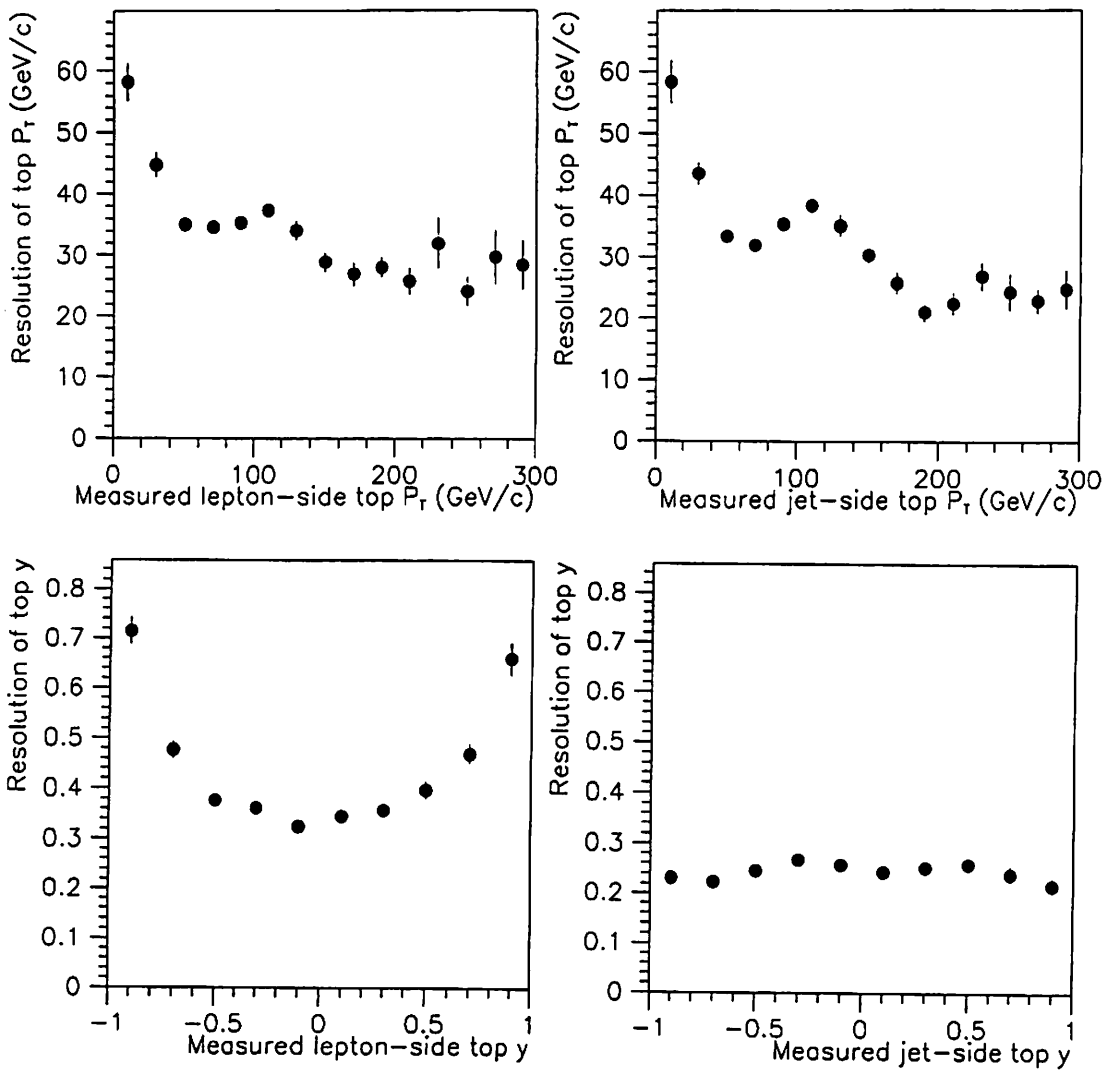

Figure 9.13: Resolutions of the lepton-side top P_T, jet-side top P_T, lepton-side top y and jet-side top y as functions of these variables, for the pretag sample without top mass constraint in the fitter.

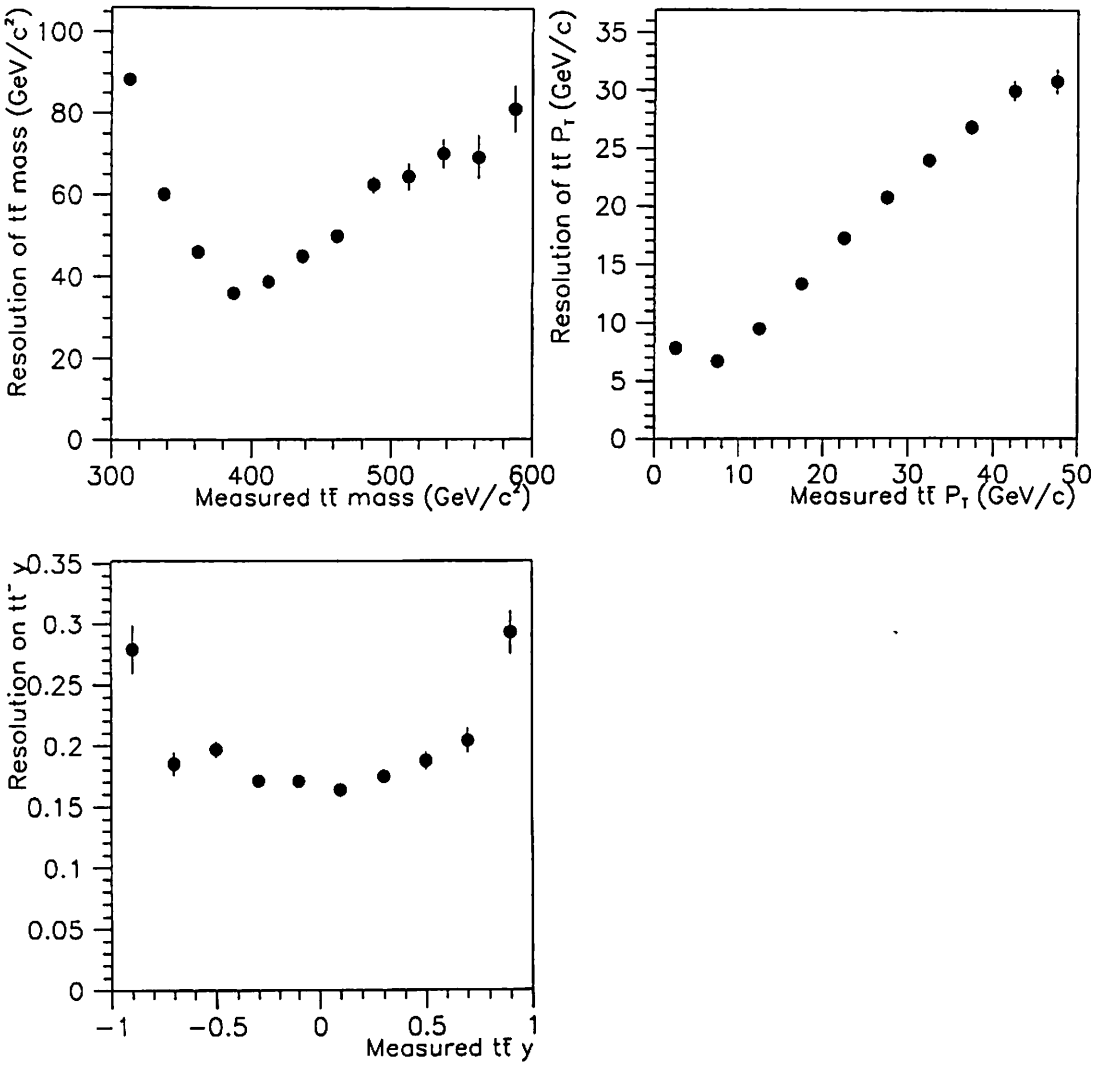

Figure 9.14: Resolutions of the $t\bar{t}$ mass, P_T and y as functions of these variables, for the pretag sample without top mass constraint in the fitter.

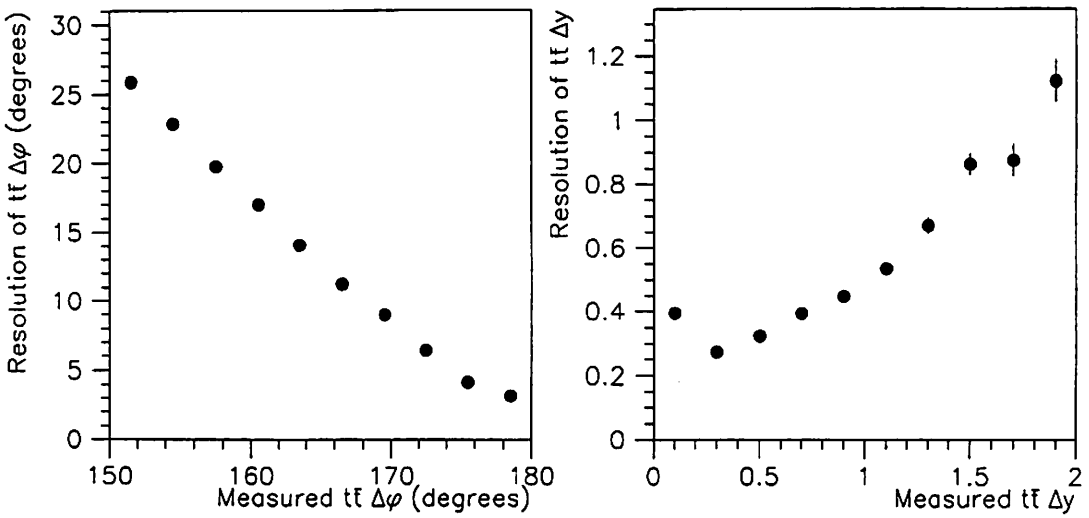

Figure 9.15: Resolutions of the $\Delta\phi$ and Δy separations between the t and $\bar{t}$ quarks, as functions of these variables, for the pretag sample without top mass constraint in the fitter.

9.4 Kinematic distributions without b-tag information

We have 153 events in 110pb^{-1} data when we do not require at least one b-tagged jet. The expected number of background events is provided by Reference[27], estimated to be 98±11 events. We simply superimposed the reconstructed distributions of data and Monte Carlo. As with all plots, black points shows the distribution of CDF data. The dashed histogram shows that of signal plus background Monte Carlo with proper normalization. The dotted histogram shows that of background events only. The mean value and r.m.s. shown in the plots always refer to CDF data.

Figure 9.16 shows the invariant mass distribution of t and $\bar{t}$. Figure 9.17 shows the P_T distribution of the $t\bar{t}$ system. Figure 9.18 shows the P_T distributions for top quarks decaying semileptonically (top plot), and top quarks decaying hadronically (bottom plot). Figure 9.19 is the distribution of $\Delta\phi$ between t and $\bar{t}$. Figure 9.20 presents the distributions in rapidity of semileptonically and hadronically decaying top quarks, of the $t\bar{t}$ system, and also the rapidity difference between t and $\bar{t}$. From looking at the Monte Carlo distributions, it is perhaps worth noting that a cut such as $|y(\text{top})| < 0.8$ would mostly remove background, and very little $t\bar{t}$.

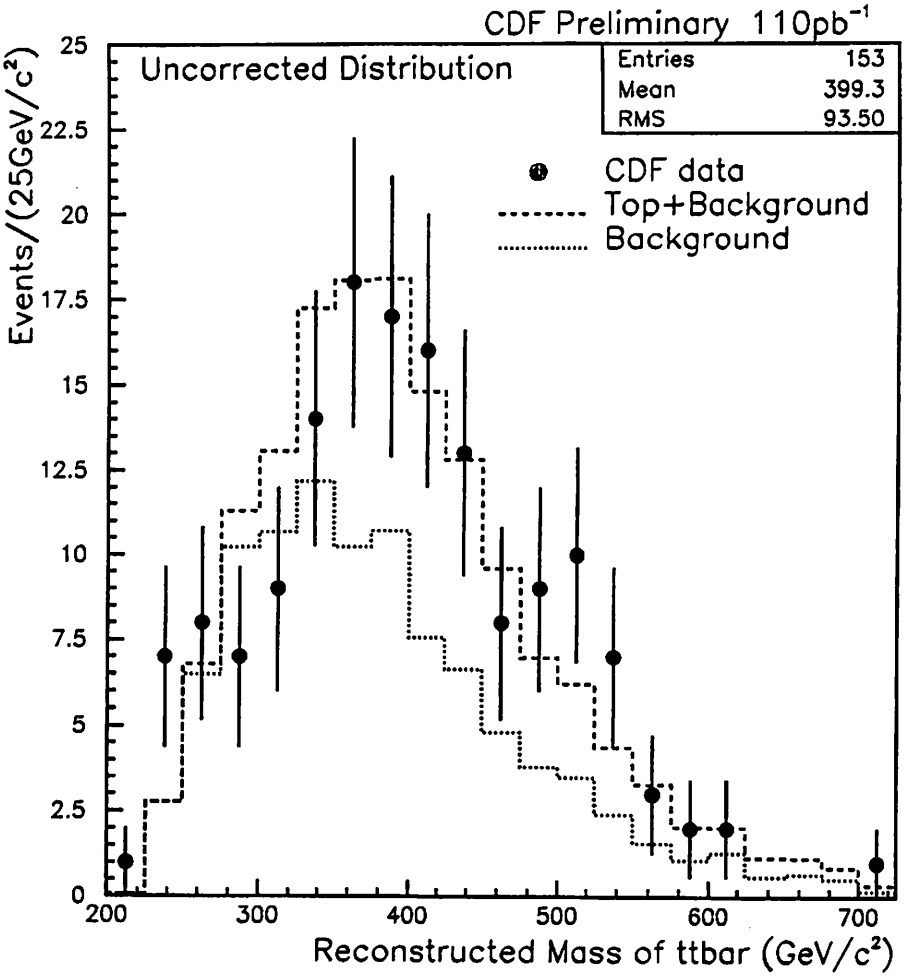

Figure 9.16: The distribution of the invariant mass of t and $\bar{t}$ on pretagged events. Dashed histogram shows the prediction of signal + background Monte Carlo. Dotted histogram shows that of background Monte Carlo.

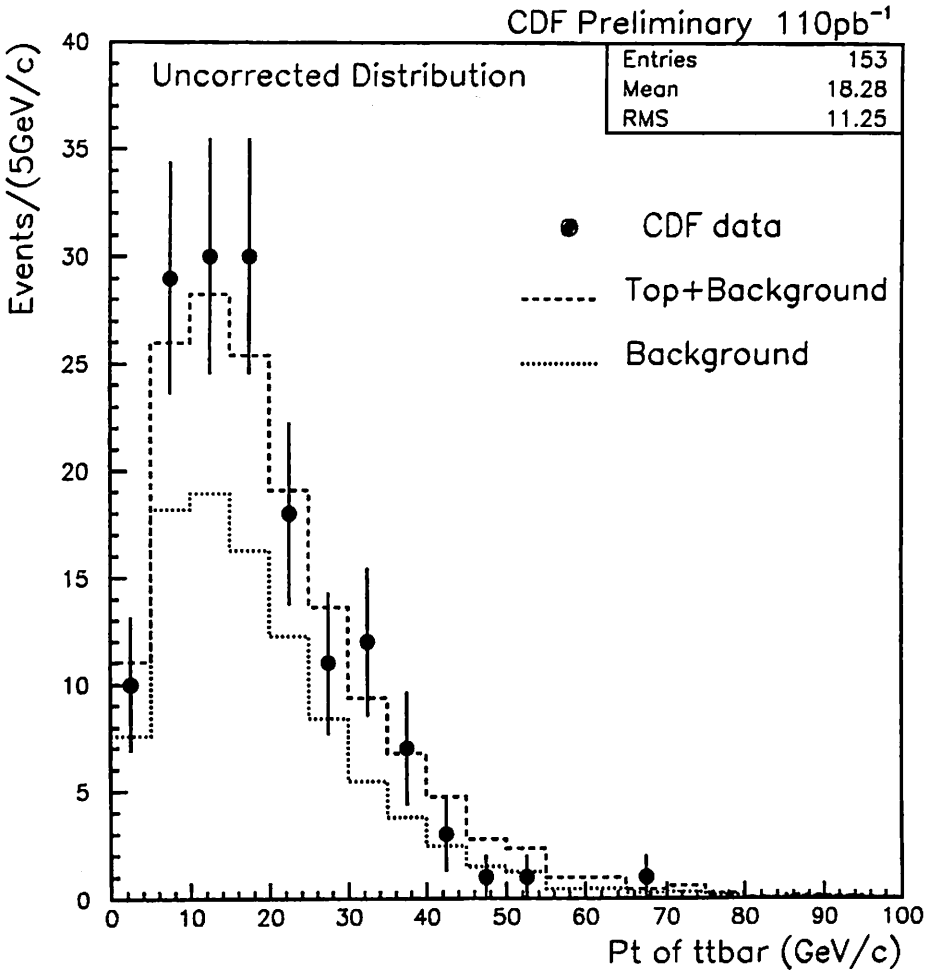

Figure 9.17: The distribution of $P_T(\ t\bar{t}\ )$.

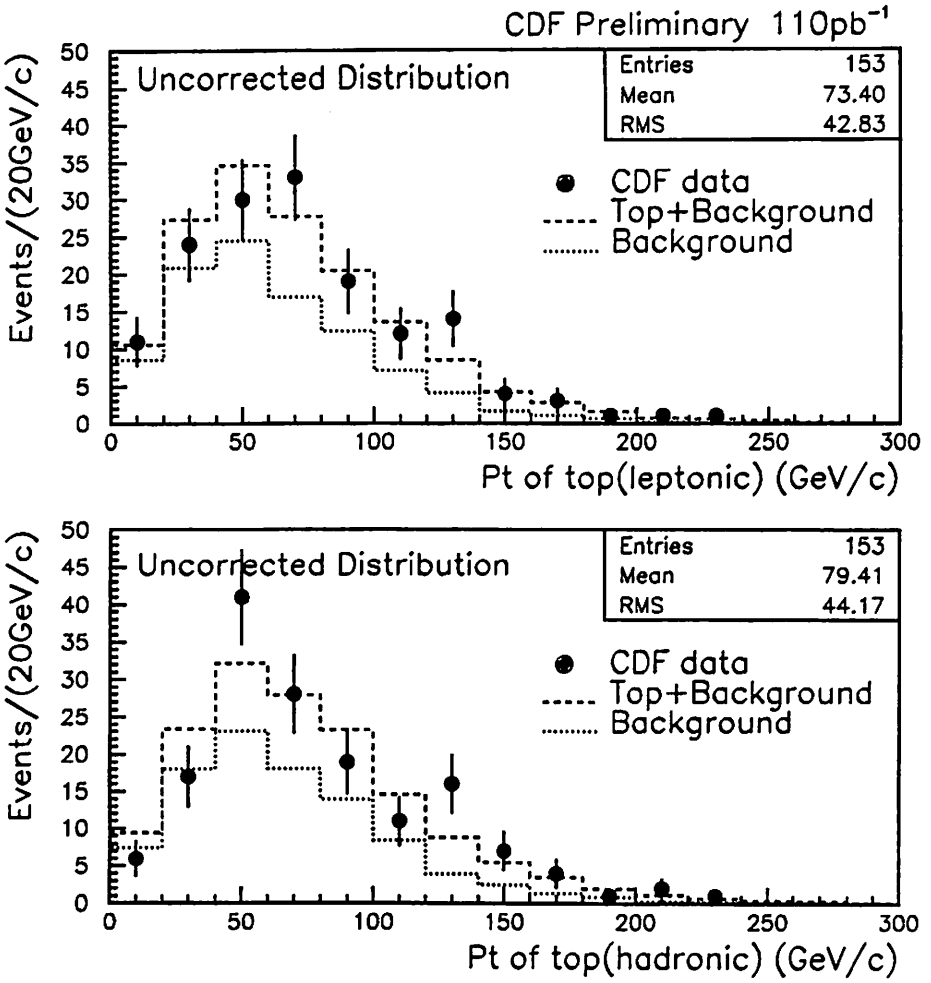

Figure 9.18: The P_T distribution for top quarks decaying semileptonically (top) and hadronically (bottom).

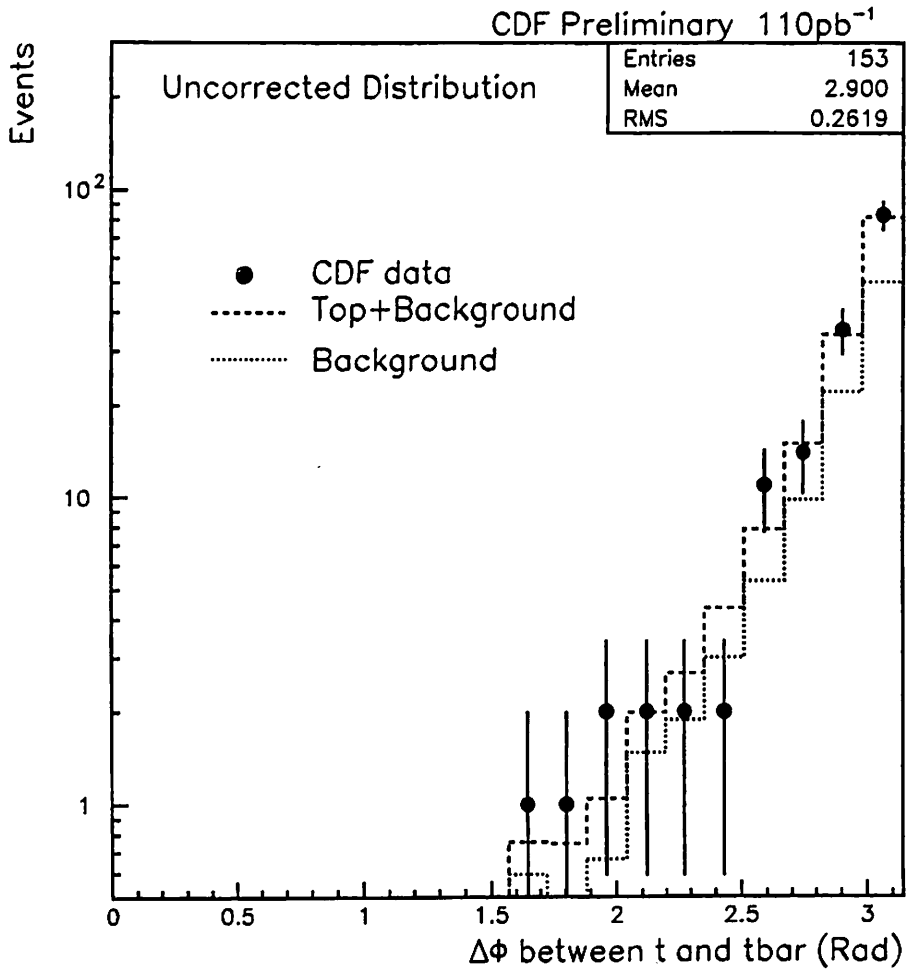

Figure 9.19: The $\Delta\phi$ distribution between t and $\bar{t}$.

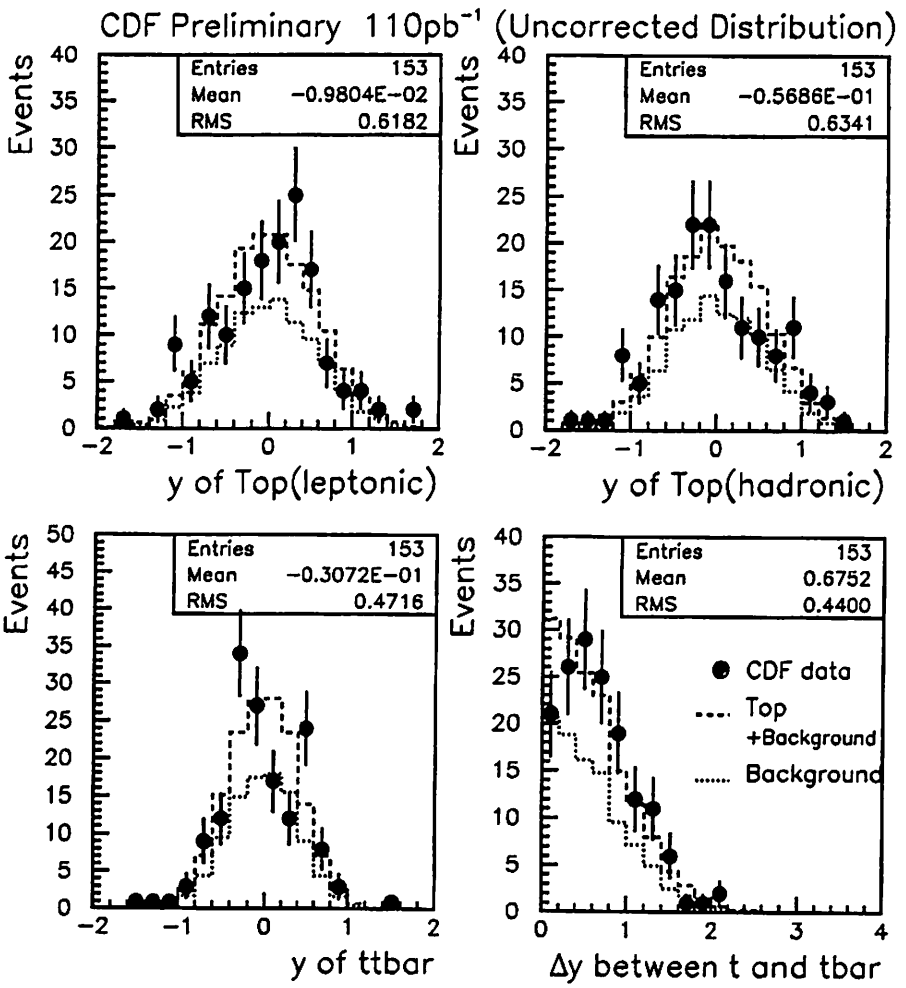

Figure 9.20: The top plots show the rapidity distributions for top quarks decaying semileptonically (left) and hadronically (right). The bottom left plot shows the rapidity distribution of $t\bar{t}$, and the bottom right plot shows the rapidity difference between t and $\bar{t}$.

All distributions show good agreement between the data and the Monte Carlo predictions. This demonstrates that the $t\bar{t}$ candidate events have kinematic properties which are consistent with the Standard Model description of $t\bar{t}$ production and decay.

9.5 Kinematic distributions of b-tagged events

Figures 9.21 to 9.25 show the kinematic distributions for the 34 single b-tagged events. The data distribution of $P_T(t\bar{t})$ seems shifted towards higher values with respect to the Monte Carlo prediction. The CDF data gives a mean of 24.0±2.2 GeV/c, whereas the Monte Carlo calculation predicts a mean of 21.2 GeV/c. This possibly systematic shift is under investigation. Here again, all distributions show good agreement between the data and the Monte Carlo predictions.

9.6 Kinematic distributions of double b-tagged events

Since we only have 9 double b-tagged events, the kinematic distributions shown in Figs. 9.26 to 9.30 have limited significance. $M(t\bar{t})$ mean of the CDF data is 473.6±32.4 GeV/c^2, whereas the Monte Carlo prediction gives $M(t\bar{t})$ mean of 425.9±2.0 GeV/c^2.

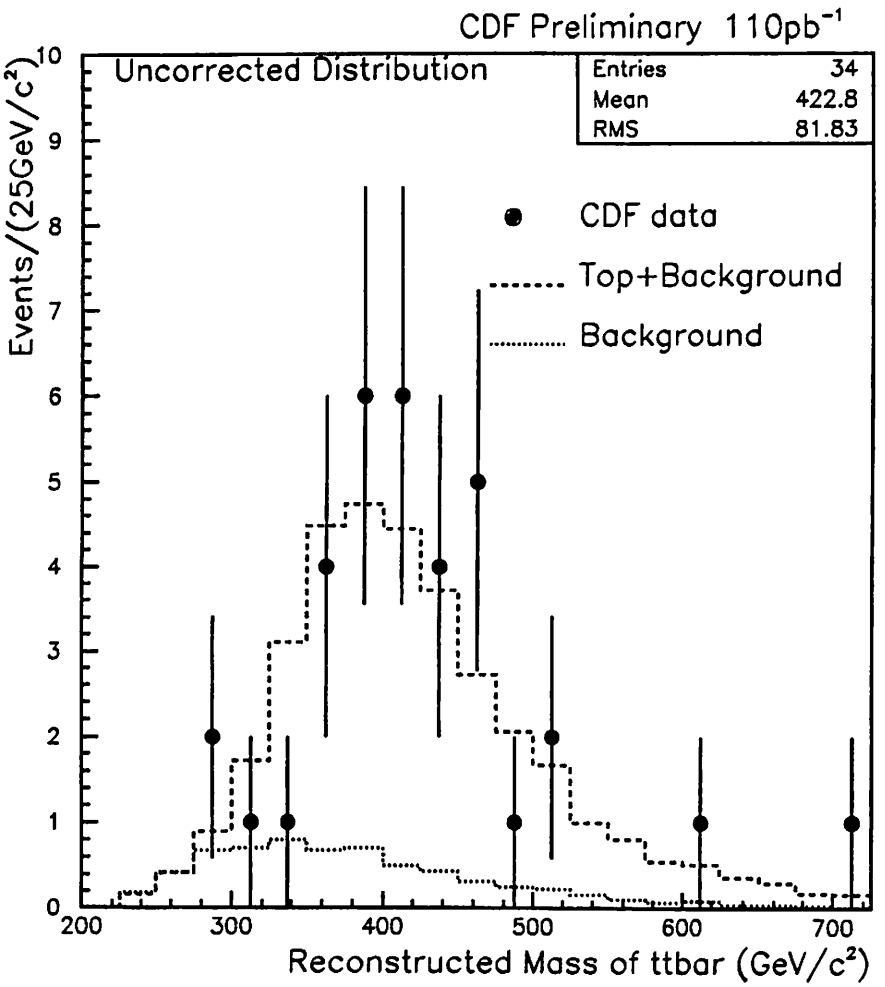

Figure 9.21: The distribution of the invariant mass of t and $\bar{t}$ on b-tag events. The dashed histogram shows the prediction of signal + background Monte Carlo. The dotted histogram shows that of background Monte Carlo.

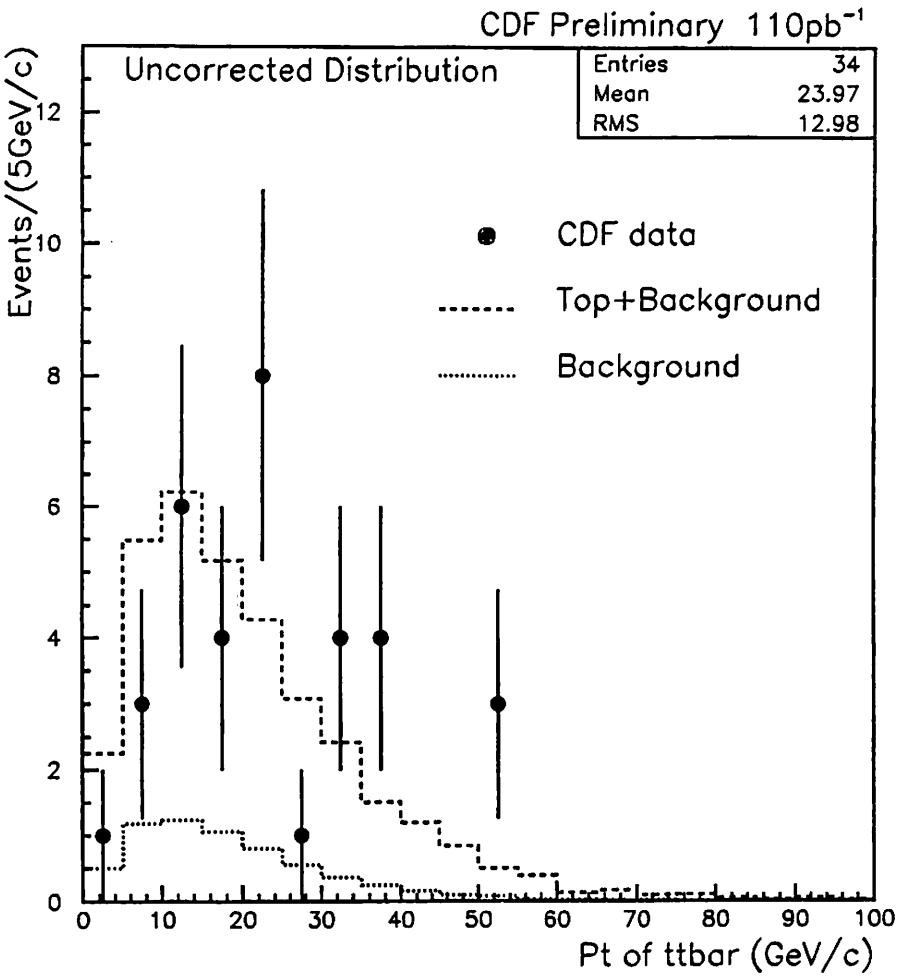

Figure 9.22: The distribution of $P_T(\ t\bar{t}\ )$.

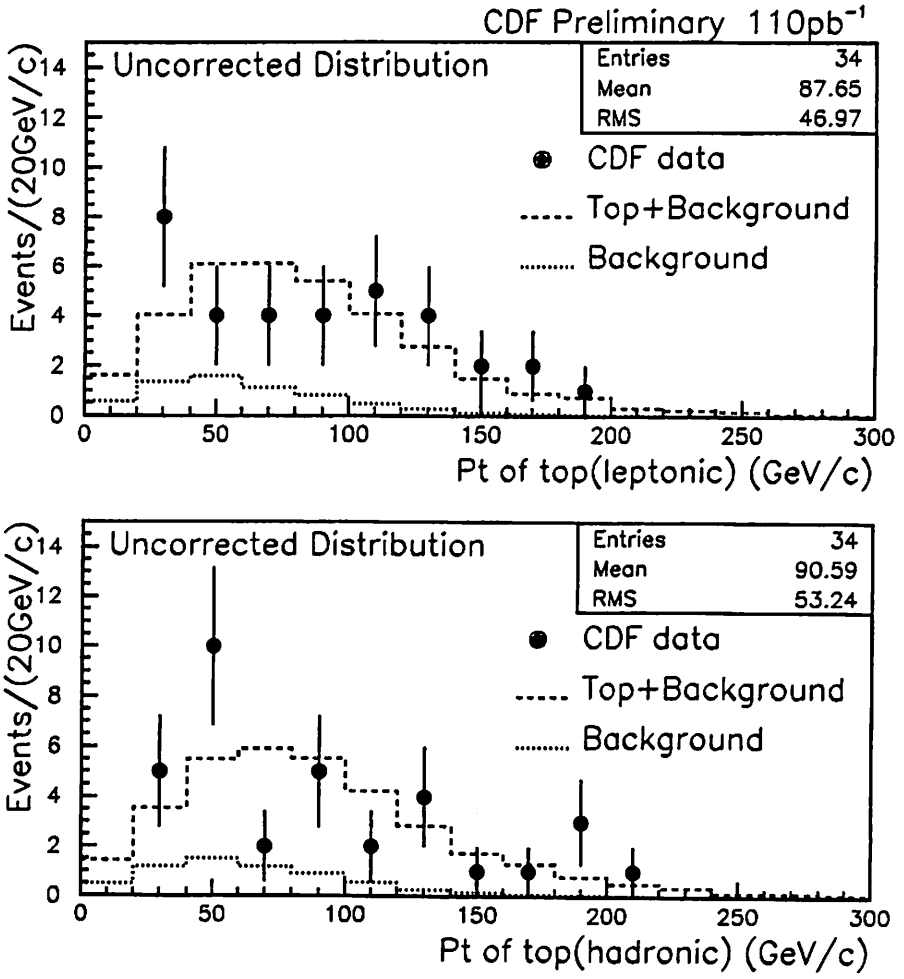

Figure 9.23: The P_T distribution for top quarks decaying leptonically (top) and hadronically (bottom).

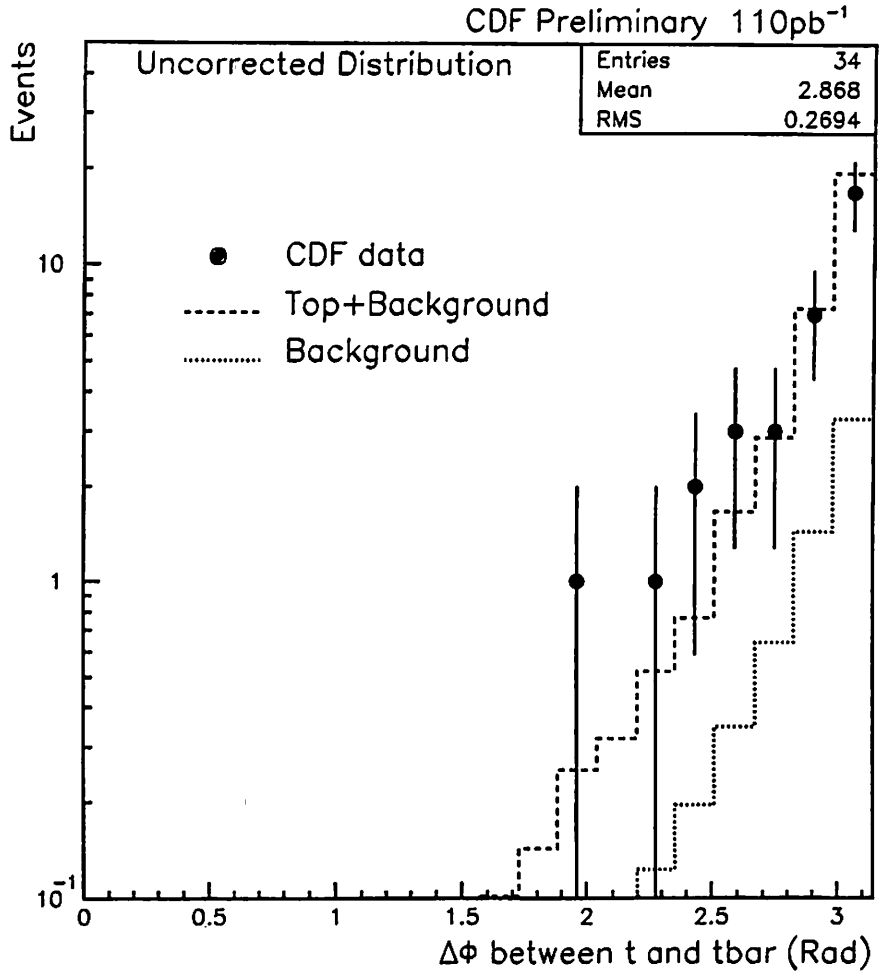

Figure 9.24: The $\Delta\phi$ distribution between t and $\bar{t}$.

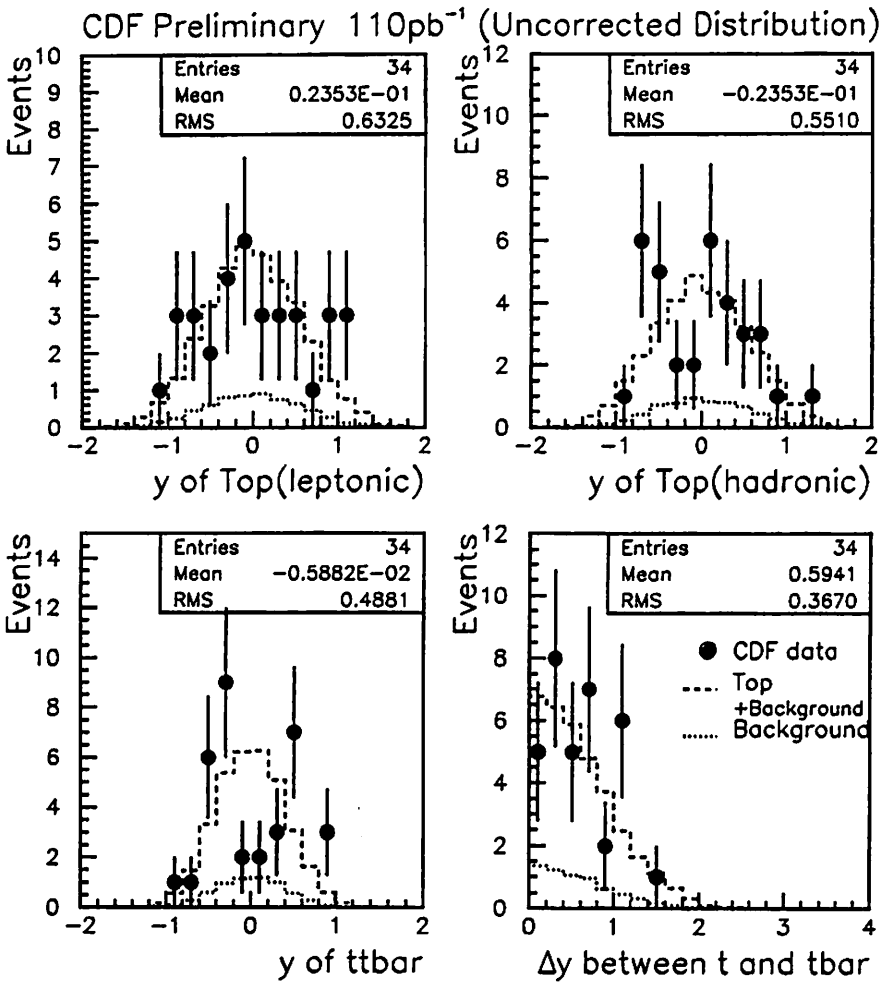

Figure 9.25: The top plots show the rapidity distributions for top quarks decaying leptonically (left) and hadronically (right). The bottom left plot shows the rapidity distribution of $t\bar{t}$, and the bottom right plot shows the rapidity difference between t and $\bar{t}$.

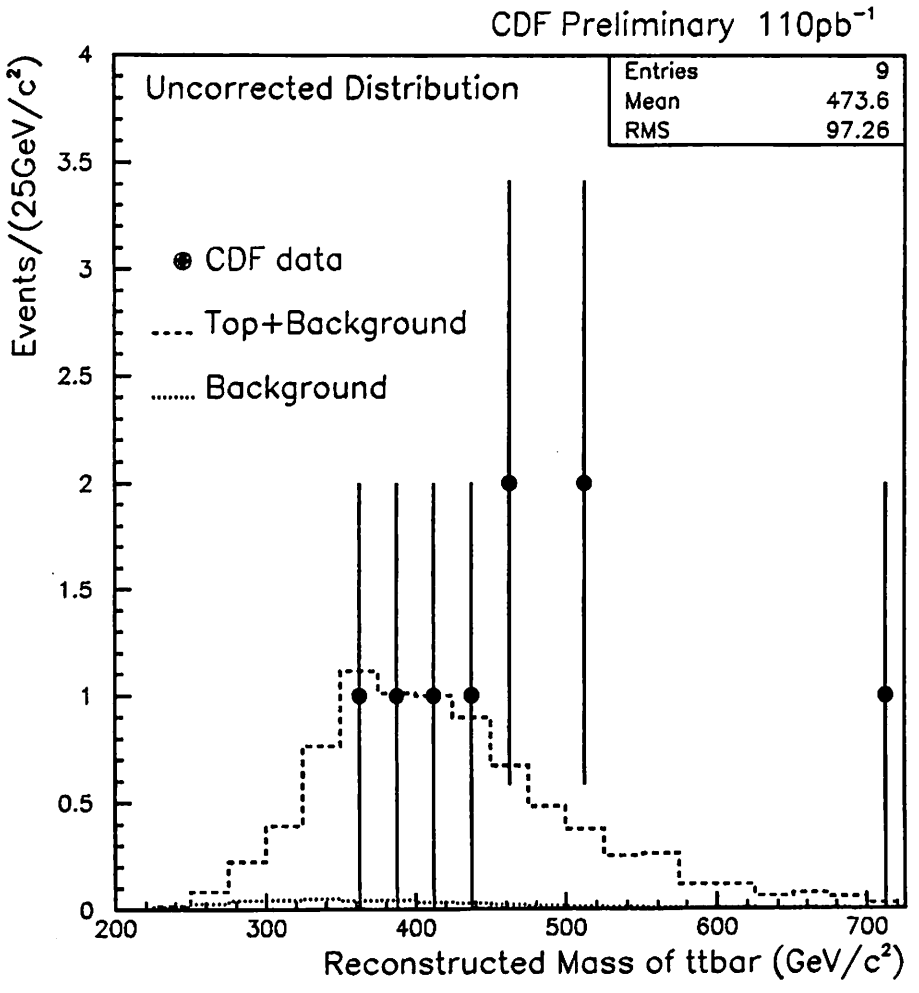

Figure 9.26: The distribution of the invariant mass of t and $\bar{t}$ on double b-tag events. Dashed histogram shows the prediction of signal + background Monte Carlo. Dotted histogram shows that of background Monte Carlo.

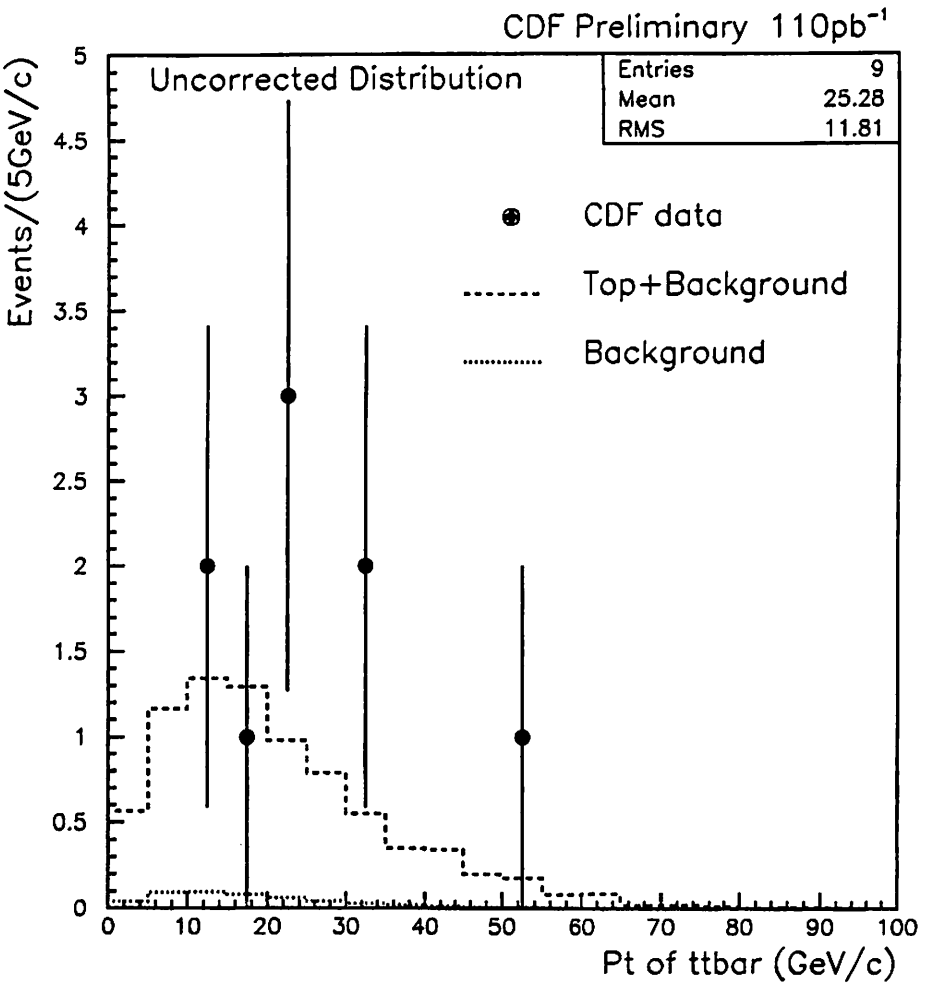

Figure 9.27: The distribution of $P_T(\ t\bar{t}\ )$.

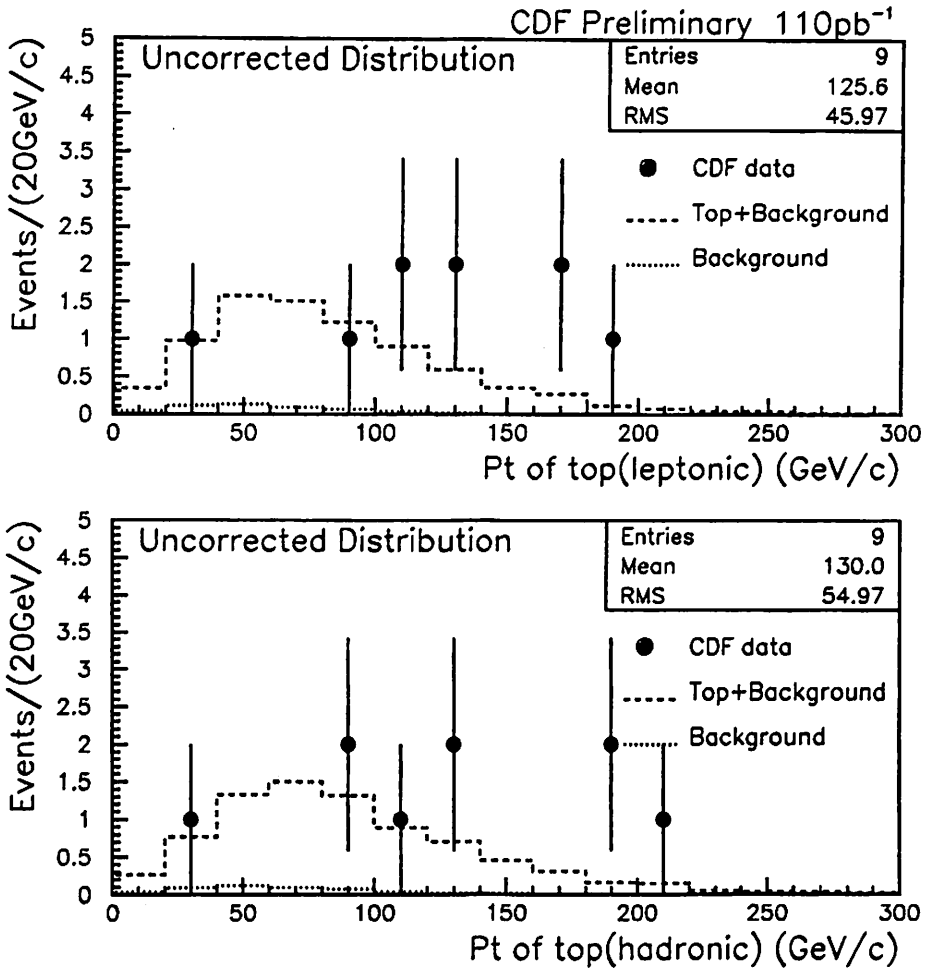

Figure 9.28: The P_T distribution for top quarks decaying leptonically (top) and hadronically (bottom).

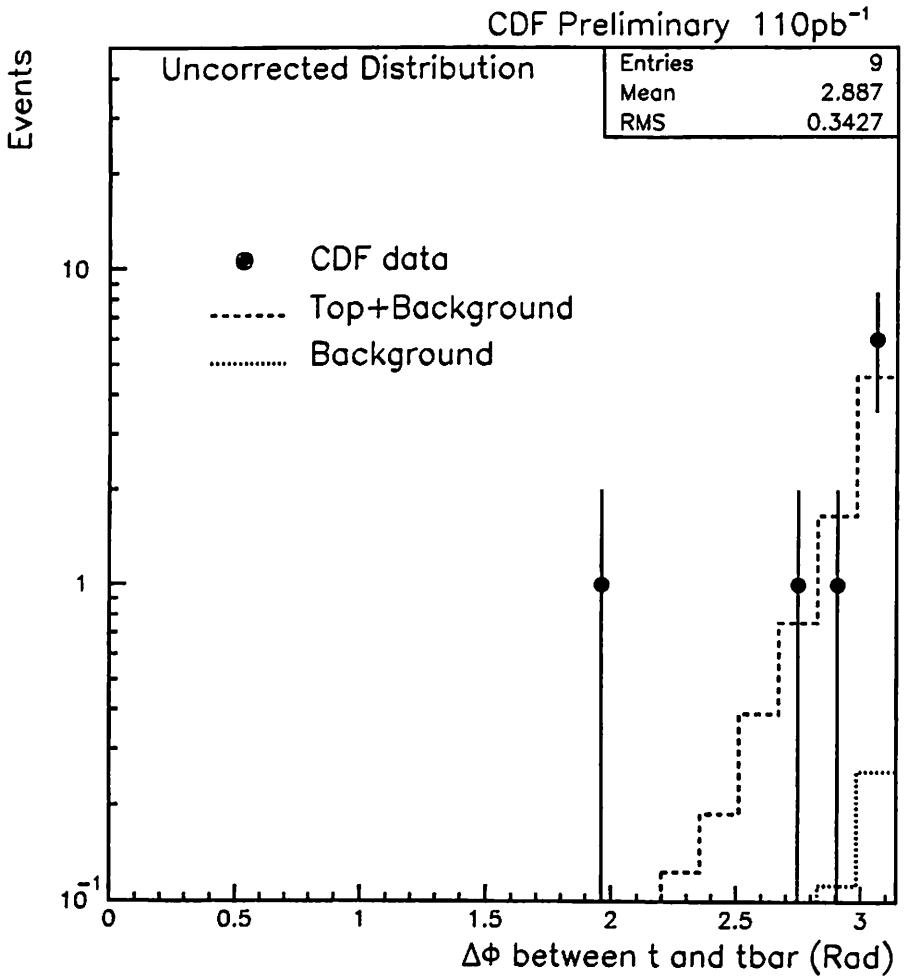

Figure 9.29: The $\Delta\phi$ distribution between t and $\bar{t}$.

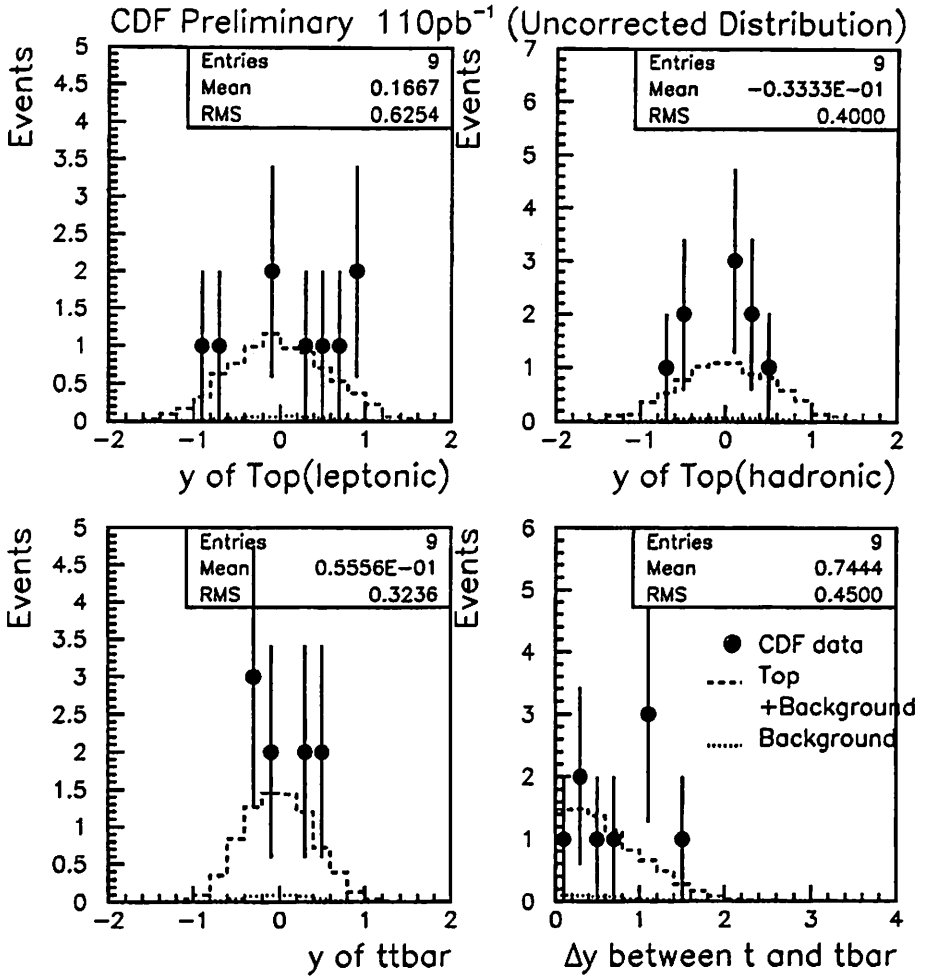

Figure 9.30: The top plots show the rapidity distributions for top quarks decaying semileptonically (left) and hadronically (right). The bottom left plot shows the rapidity distribution of $t\bar{t}$, and the bottom right plot shows the rapidity difference between t and $\bar{t}$.

9.7 Conclusion on kinematic distributions

We checked the kinematic distributions of the $t\bar{t}$ candidate events for 110pb^{-1}. All distributions agree with the Monte Carlo predictions for $t\bar{t}$ plus background. Therefore we do not see any indication for substantial deviation from the Standard Model predictions at this level of statistics. There is one interesting double b-tagged event which has a high $t\bar{t}$ invariant mass.

Chapter 10

Conclusions

We performed the measurement of the top quark mass and the kinematics in top quark production and decay in 1.8 TeV $p\bar{p}$ collisions with the CDF detector using 110pb^{-1} data.

Hadronic W decay process was searched for in $t\bar{t}$ events. The dijet invariant mass distribution in $W+\geq$4jet events showed an excess of (29$\pm$13) $W \rightarrow$jj signal after an optimized H cut. The dijet mass peak has a mean of 77.1$\pm$3.8(stat)$^{+3.0}_{-2.9}$(syst) GeV/c^2 which is consistent with a W mass peak. This indicates there is no significant jet energy scale shift with the CDF detector.

Top quark mass was measured using $W+\geq$4jet events with two b-tagged jets. Requiring the invariant mass of non b-tagged jets within a W mass window, we found 9 $t\bar{t}$ candidates events. Expected number of background events was 0.4$\pm$0.1. Using these candidate events, we measured a top quark mass to be 174.8$\pm$7.6(stat)$\pm$5.6(syst) GeV/c^2 with a likelihood method.

We observed kinematical distributions of $t\bar{t}$ events to investigate the top quark production and decay process. Various kinematic distributions were compared between the CDF data and the Monte Carlo events. All distributions of the CDF data agree with the Monte Carlo predictions. Therefore we do not see any significant deviation from the Standard Model with the present statistics.

Bibliography

[1] A Jawahery, Proc. 24th Int. Conf. on High Energy Physics, Munich, Aug 1988

[2] H.Albrecht *et al.*(ARGUS collaboration), Phy.Lett., 192B (1987) 245

[3] H.Albrecht *et al.*(ARGUS collaboration), Phy.Rev.Lett.,**62** 2233 (1989)

[4] A.Buras and J.Gerard, Phys.Lett. , 203B (1988) 272

[5] M.Akrawy *et al.*, CERN-EP/89-154

[6] G.Abrams *et al.*, Phys. Rev. Lett.,**63** 2447 (1989)

[7] F.Abe *et al.*, Phys. Rev. Lett. **68** 447 (1992); F.Abe *et al.*, Phys. Rev. D **45** 3921 (1992)

[8] S.Abachi *et al.*, Phys. Rev. Lett. **72** 2138 (1994)

[9] LEP Electroweak Woring Group, B.Pietrzyk, Laboraatorie de Physique des Particules Report No. LAPP-EXP-94.-7, 1994 (unpublished)

[10] F.Abe *et al.* Phy.Rev. D **50** 2966 (1994)

[11] F.Abe *et al.* Phy.Rev. Letters **73** 4330 (1995)

[12] S.Abachi *et al.* Phy.Rev. Letters 74 2442 (1995)

[13] E. Laenen, J. Smith, W.L. van Neerven, Phy. Lett. B 321 (1994) 254

[14] F. Bedeschi *et al.* Nucl. Instr. and Meth. A268(1988)

[15] G. Marchesini, B.R. Webber, G. Abbiendi, I.G. Knowles, M.H. Seymour and L. Stanco, Computer Physics Communications **67** (1992) 465.

[16] F. Paige and S. D. Protopopescu, BNL Report No. 38034, 1986(unpublished)

[17] F.A. Berends, W.T. Giele, H. Kuijf and B. Tausk, Nucl. Phys. **B357**, 32(1991); W. Giele, Ph.D. thesis, Leiden.

[18] CDF Collaboration, J. Benlloch, in *The Fermilab Meeting*, Proceedings of the Meeting of the Division of Particles and Fields of the APS, Batavia, Illinois, 1992, edited by C. H. Albright *et al.* (World Scientific, Singapore, 1993), p. 1091

[19] G. Watts, Ph.D. thesis, University of Rochester, 1994.

[20] D.Kestenbaum Ph.D. thesis Harvard University, 1996.

[21] D. Buskulic *et al.* Phy.Rev. Lett. B313 535(1993)

[22] R. Wilkinson, R. Hollebeek CDF internal note 3136 and 3543.

[23] Anwar Ahmad Bhatti CDF internal note 2457

[24] S. Behrends CDF internal note 3550

[25] S.B. Kim, S. Vejcik, CDF internal note 3503

[26] F.Abe *et al.* Phy.Rev. Lett. **75** 3997 (1995)

[27] Brian Harral CDF internal note 3526

[28] F.Abe *et al.* Phy.Rev. D **45** 1448 (1992)

[29] F.Abe *et al.* Phy.Rev. D **47** 4857 (1993)